ABSTRACT

Title of Dissertation: MECHANOCHEMICAL SIMULATIONS OF IN VIVO ACTIN ARCHITECTURES

Qin Ni
Doctor of Philosophy, 2020

Dissertation Directed by: Professor Garegin A. Papoian
Department of Chemistry and Biochemistry

Actin cytoskeleton arranges into distinct architectures to enable cell functions under different mechanochemical environments. Although recent works have revealed the key components and processes involved in actin network dynamics, how actin cytoskeleton responds to mechanical and chemical cues to assemble higher-order *in vivo* structures is still poorly understood. In this thesis, we use an advanced computer simulation platform to explore the mechanochemical dynamics and the physical principles underlying the formation of three ubiquitous actin scaffolds *in vivo*: actin bundles, dendritic lamellipodia, as well as actin rings and shell-like cortices. We first investigate the adaptive remodeling of actomyosin networks induced by a tensile external force. The application of tensile force rapidly alters filaments' orientation, followed by slower myosin motor driven contractility that gradually consolidates the structure into a thick actin bundle. These distinct actin remodeling mechanisms at short *versus* long timescale provide new insights to the formation of stress-fiber like actin architectures. Then, we investigate the dynamics underlying

branched actin filament assembly in networks similar to lamellipodia. By varying actin branching factors and polymerization termination proteins, we reveal how individual filament assembly is related to large scale network turnover, and discuss how it affects lamellipodia driven membrane protrusion and cell migration. Lastly, we explore the question of why actomyosin networks often form ring-like or shell-like structures in cells but condense into clusters in reconstituted networks, where this structural discrepancy is regulated by a balance between myosin driven contraction and actin polymerization speed. Our works provide potential "recipes" for the assembly of cellular actin structures, in the hope of revealing the fundamental biophysical principles underlying active cytoskeleton self-organization.

MECHANOCHEMICAL SIMULATIONS OF IN VIVO ACTIN ARCHITECTURES

by

Qin Ni

Dissertation submitted to the Faculty of the Graduate School of the
University of Maryland, College Park in partial fulfillment
of the requirements for the degree of
Doctor of Philosophy
2020

Advisory Committee:
Professor Jeffery B. Klauda, Chair
Professor Garegin A. Papoian, Co-Chair
Professor Srinivasa Raghavan
Professor Amy Karlsson
Professor Arpita Upadhyaya, Dean's representative

Dedication

To my grandparents,

Ni Zhengling and Su Xiulan,

for their love

Acknowledgments

I would like to thank many people for helping my research and life. This dissertation will not be possible without your help.

First, thank you to my advisor Prof. Garyk Papoian for your support. You have such a broad, multidisciplinary knowledge that always inspires me. These projects in the lab opened a new world to me, and you have taught me how to think critically and independently on scientific problems. I also really appreciate that you have always been respectful of our ideas, which gave me the confidence in developing my original thoughts. Your vision in science is something I will always chase for.

I would like to sincerely thank my fantastic group members in the Papoian lab: Aravind Chandrasekaran, Cal Floyd, Haoran Ni, Mary Pitman, and alumni Hao Wu, James Komianos, and Haiqing Zhao. It is so lucky to have you guys as my lab mates, and thank you for helping me with my research, presentations, writings, and everything. I will miss working with you and all the fun times we had, and I wish you a happy life and lots of success in your future career.

To the faculties and staff at the University of Maryland. Thank you to Prof. Arpita Upadhyaya for helping me throughout my PhD. You are like my second advisor. It is our collaboration that motivates me and gives me the confidence to pursue an experiment based position for my postdoc training. Thank you to my

co-advisor Prof. Jeffery Klauda. Your help always came promptly, and I appreciate your efforts to help me stay connected with the Chemical Engineering department. I also thank many other faculties and administrative staff at the Chemical Engineering department and the Institute for Physical Science and Technologyfor delivering excellent courses and services.

I am grateful to those who have done fantastic works with me. Thank you to Prof. Yi Jiang, Prof. Andreea Trache, Xiuxiu He, and Xiaona Li for bringing up the actin bundle project and all the insightful discussions. Thank you to Kaustubh Wagh and, again, Prof. Arpita Upadhyaya for your excellent experiments and all the hard works on the actin ring project. Thank you to Prof. Veronica Ciocanel for sharing your precious career experiences with me. Thank you to all the other collaborators whom I have met or have not yet met. I wish all of you all the best in your future endeavors.

My undergraduate experience at Rutgers University helps me a lot to overcome the obstacles of living in the United States. I would like to particularly thank Prof. Yee Chiew for introducing the SCUT-Rutgers program to me and guide me to the field of computer simulation. I also thank the faculties at South China University of Technology for encouraging me to pursue a degree aboard.

Of course, this dissertation would not be possible without the love and support from my family and friends. To my parents, Ni Hehong and Liu Xiaohong, my grandparents, and my aunts and uncles, thank you for always having faith in me. To all my friends around the world, thank you for your supports and those happy memories. Thank you all.

Table of Contents

Dedication ii

Acknowledgements iii

Table of Contents v

List of Tables viii

List of Figures ix

List of Abbreviations xi

Chapter 1: Introduction 1
- 1.1 Overview of the actin cytoskeleton . . . 2
- 1.2 Actin structures and their chemical and mechanical dynamics . . . 6
  - 1.2.1 Contractile actin bundles - stress fibers . . . 6
  - 1.2.2 Dendritic actin networks – lamellipodia . . . 9
  - 1.2.3 Outward condensation - actin cortices and rings . . . 10
- 1.3 MEDYAN: a simulation platform for active cytoskeleton . . . 12
- 1.4 Outline of Chapters . . . 17

Chapter 2: Tensile force induced actin bundling 19
- 2.1 Introduction . . . 19
- 2.2 Simulation Methods . . . 23
- 2.3 Results . . . 27
  - 2.3.1 Actin cytoskeleton reorganization in live VSMCs under mechanical stimulation reveals a two-step adaptive response . . . 27
  - 2.3.2 Rapid formation of actin bundles in response to tensile force in MEDYAN simulations . . . 28
  - 2.3.3 Tensile force induces actin alignment in MEDYAN simulations 32
  - 2.3.4 Two-step development of actin bundles depends on both faster mechanical alignment and slower chemical response . . . 32
- 2.4 Discussions . . . 37

Chapter 3: Exploring Actin Filament Assembly in Dendritic Networks 42
- 3.1 Introduction . . . 42

3.2 Methods . . . 47
3.3 Results . . . 48
3.3.1 Actin network turnover is mainly driven by treadmilling of preexisting filaments. . . . 48
3.3.2 Slow CP dissociation promotes actin *de novo* assembly without altering global turnover. . . . 51
3.3.3 Arp2/3 and formin promote turnover via dissimilar treadmilling profiles. . . . 54
3.4 Discussion and Conclusions . . . 55

Chapter 4: The formation of cortex-like and ring-like actomyosin structures **60**
4.1 Introduction . . . 60
4.2 Results . . . 63
4.2.1 Filament treadmilling generates disordered actin networks . . . 63
4.2.2 Actin rings and cortices formation upon enhancing filament treadmilling rates . . . 64
4.2.3 Disrupting treadmilling induces centripetal collapse of actin rings *in vivo* and *in silico* . . . 67
4.3 3. Discussion . . . 70
4.4 Methods . . . 72
4.4.1 Simulation setup . . . 72

Chapter 5: Discussion and Outlook **76**

Appendix A: Supporting Information for Chapter 2 **80**
A.1 Experimental methods . . . 80
A.1.1 Vascular smooth muscle cell cultures and transient transfections 80
A.1.2 Vascular smooth muscle cell imaging . . . 81
A.1.3 AFM mechanical stimulation of VSMCs . . . 82
A.1.4 Three-dimensional image analysis . . . 83
A.2 Simulation parameters . . . 83
A.3 Supplementary figures . . . 85

Appendix B: Supporting Information for Chapter 3 **89**
B.1 Model Details . . . 89
B.1.1 Time integration method and general simulation protocol in MEDYAN . . . 89
B.1.2 Reactions and parameters . . . 91
B.1.3 Mechanical models . . . 95
B.1.4 Dynamic rate models . . . 97
B.1.5 Measurement of turnover halftime, length and treadmilling . . . 97
B.2 Supplementary Figures . . . 101

Appendix C: Supporting Information for Chapter 4 **109**

C.1 Computational Model Details . . . 109
C.1.1 Mechanical models . . . 111
C.1.2 Chemical models . . . 113
C.1.3 Mechanochemical models . . . 117
C.1.4 Simulation protocol . . . 119
C.2 Defining treadmilling rate and treadmilling inhibition simulation setups . . . 120
C.3 Experimental methods . . . 124
C.3.1 Cell culture and transfection . . . 124
C.3.2 Plasmids and reagents . . . 125
C.3.3 Preparation of glass coverslips . . . 125
C.3.4 Microscopy . . . 125
C.3.5 Image analysis . . . 126
C.4 Supplementary Figures . . . 127

Bibliography **132**

List of Tables

A.1 Parameters for the simualtions 85

B.1 Parameters for diffusion and reactions. 93

C.1 Mechanical parameters. 112
C.2 Parameters for diffusion and reactions. 115
C.3 Mechanochemical dynamic rate parameters. 117

List of Figures

1.1 Actin filament polymerization . . . 3
1.2 Structures of actin stress fibers. . . . 8
1.3 Localization and high resolution image of Arp2/3 complex and actin filaments in lamellipodia of Xenopus Keratocyte. . . . 11
1.4 Sketch of actin cortex of an *in vitro* system mimicking cells. . . . 13
1.5 MEDYAN simulation protocol. . . . 16

2.1 Response of VSMC to external pulling force. . . . 29
2.2 Setup of the actin simulation with external force. . . . 31
2.3 Simulated actin network response to external force. . . . 33
2.4 Actin bundle formation under external force. . . . 34
2.5 External force induced anisotropic response. . . . 36
2.6 Isotropic clustering *versus* anisotropic bundling. . . . 38

3.1 Chemical reaction setup and a snapshot in dendritic actin network simulation. . . . 44
3.2 Turnover dynamics in dendritic actin networks . . . 50
3.3 Turnover and treadmilling regulated by capping proteins. . . . 52
3.4 Assembly of pre-existing filament *versus* newly nucleated filaments regulated by capping protein dissociation rate. . . . 53
3.5 Turnover dynamics regulated Arp2/3 nucleation. . . . 56

4.1 Spatial and temporal evolution of actin structures. . . . 65
4.2 Network geometry and energy properties at different treadmilling rates. 68
4.3 Jurkat T cell actin rings deconstruction. . . . 74
4.4 Simulated actin rings deconstruction. . . . 75

A.1 Filament polarity distribution. . . . 85
A.2 Filament radial distribution and snapshots after 5th pulling. . . . 86
A.3 Simulated actin network with a static AFM probe. . . . 87
A.4 Simulated actin network with insufficient and excessive AFM attachment. . . . 88

B.1 Turnover fraction calculation. . . . 99
B.2 An example of turnover fraction as time. . . . 99
B.3 Average filament length. . . . 101

B.4 Turnover halftime and the number of filament when inhibiting nucleation at steady state. . . . 102
B.5 The capping protein "funnel" effect. . . . 102
B.6 Filament capped fraction. . . . 103
B.7 Turnover dynamics with formin nucleation. . . . 103
B.8 Turnover dynamics with Arp2/3 nucleation. . . . 104
B.9 G-actin *versus* F-actin during network evolution. . . . 105
B.10 Turnover halftime as a function of capped fraction, semi-log plot. . . . 106
B.11 Turnover halftime as a function of capping dissociation rate, semi-log plot. . . . 107
B.12 Turnover halftime as a function of Arp2/3 concentration, semi-log plot. 108

C.1 Median of filament radial density distribution for 5 trajectories. . . . 121
C.2 Average filament length as a function of time. . . . 123
C.3 Filament radial density distribution of disordered networks. . . . 127
C.4 Median of filament radial density distribution at different treadmilling rates. . . . 128
C.5 The distribution of filament orientation. . . . 129
C.6 Actin ring in a 10µdiameter disk. . . . 130
C.7 (a-b) Box plots of the number of bound linker (a) and F-actin (b) in the system. Almost all motors are bound upon addition, thus we do not provide a plot for the number of bound motor. . . . 131

List of Abbreviations

in vivo	"within the living", in living organisms
in vitro	"within the glass", in a laboratory environment
in silico	"within silicon", performed on a computer
ATP	Adenosine triphosphate
ADP-Pi	Adenosine diphosphate - phosphate
F-actin	Filamentous actin
ENA/VASP	Enabled/vasodilator-stimulated phosphoprotein
ADF	Actin-depolymerizing factor
NMII	Non-muscle myosin II
GTPases	Guanosine triphosphate hydrolase enzymes
WASP	Wiskott-Aldrich syndrome protein
WAVE	WASP-family verprolin-homologous protein
ROCK	Rho-associated protein kinase
GTP	Guanosine triphosphate
AFINES	Active Filament Network Simulation
MEDYAN	Mechanochemical Dynamics of Actin Networks
NRM	Next reaction method
AFM	Atomic force microscopy
VSMC	Vascular smooth muscle cell
FN	Fibronectin
DMEM	Dulbecco's modified eagle medium
FBS	Fetal bovine serum
FRAP	Fluorescence recovery after photobleaching
CP	Capping protein
LatA	Latrunculin A
EGFP	Enhanced green fluorescent protein
TIRF	Total internal reflection fluorescence microscopy
DMSO	Dimethyl sulfoxide

Chapter 1: Introduction

In eukaryotic cells, actin protein filaments, myosin molecular motors and associated regulatory proteins self-organize into highly ordered actomyosin structures. These actomyosin networks dynamically rearrange themselves to form various *in vivo* architectures with distinct mechanochemical properties that allow cells to migrate, change shape, or transmit force. The remodeling is controlled by the mechanochemical activity of cytoskeletal components and accessory proteins. As a consequence, actomyosin organization undergoes complex mechanochemical feedback interactions, and the fundamental mechanisms underlying the formation of distinct cellular architectures are still poorly understood. This dissertation investigates the dynamic remodeling of actin networks at different mechanical and chemical environments via computer simulations. We explore the fundamental ingredients required for the assembly of different cellular actin structures, and investigate the key mechanochemical cues that determine the remodeling of actin structures.

In this chapter, I will first provide an overview of actin cytoskeleton by introducing its biological functions, chemical dynamics, and mechanical properties. I will then highlight three *in vivo* actin structures that are studied in this thesis, discussing their essential components and self-organization dynamics. The signifi-

cance, the development history, and the current capacity of the simulation platform used throughout this dissertation will be reviewed in the following part. Lastly, I will outline the subsequent chapters in the thesis.

1.1 Overview of the actin cytoskeleton

Actin plays a central role in cellular function by forming semi-flexible filaments. Actin filaments are double-helical polymers with a persistence length of µm and a diameter of 7 nm [2]. By hydrolyzing adenosine triphosphate (ATP), actin filaments undergo rapid assembly in a highly polarized way. ATP and ADP-Pi (adenosine diphosphate - phosphate) bound globular actin monomers (G-actin) preferentially bind to filament barbed (plus) end, leading to fast polymerization (Fig. 1.1A). The release of phosphate converts filamentous actin (F-actin) into the ADP-bound state, which is enriched at the pointed (minus) end of a filament and undergoes rapid dissociation. This process is often called treadmilling, which enables actin filaments to move towards their barbed end direction without external forces [3, 4]. Filament treadmilling is able to generate force acting against the cell membrane, which is critical for cell migration [5].

Actin assembly is also mediated by regulatory proteins. For example, filaments can assemble in a *de novo* way via formin homology proteins, which aggregate actin monomers and nucleate filaments [7]. Formin can also bind to the barbed end of filaments and promote the filament polymerization when working synergistically with profilin [8] (Fig. 1.1B-C). Arp2/3 complex is the other main filament nu-

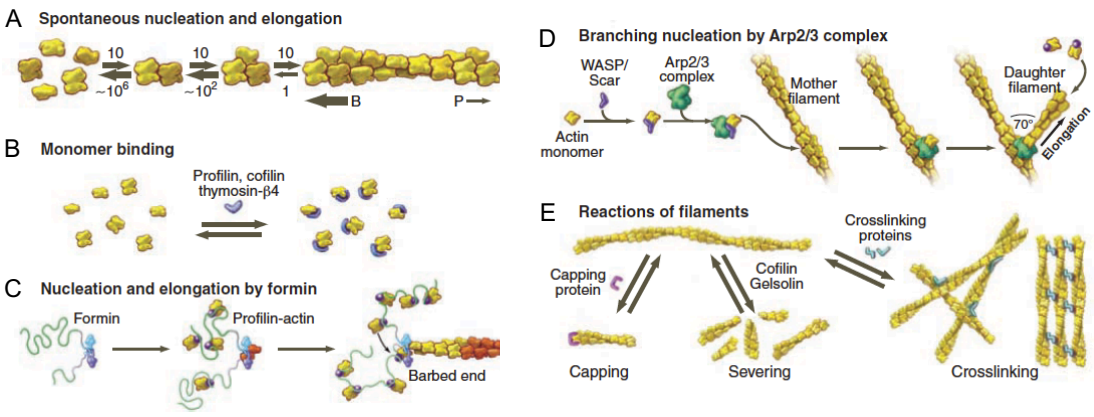

Figure 1.1: Actin filament assembly and other fundamental reactions. (A) Filament nucleation and elongation. Filaments grow faster at the barbed end (B) and slower at the pointed end (P). (B) Actin monomer binding proteins. (C) Formin-profilin induced filament nucleation and elongation. (D) Arp2/3 complex induced filament branching. (E) Filament capping, severing, and crosslinking reactions. Image is adapted from [6] with permission from Elsevier under STM permissions guidelines.

cleator, which has a very different nucleating mechanism. Arp2/3 complex would bind to preexisting mother filaments and nucleate daughter filaments with an angle of 70°, forming a "dendrite" [9, 10] (Fig. 1.1D). Capping protein is another main regulator that binds to the barbed end of actin filaments and terminated the filament polymerization, mediating filament length and density of branchers [11] (Fig. 1.1E). ENA/VASP (enabled/vasodilator-stimulated phosphoprotein) proteins also bind to filament barbed ends, however, they promote filament polymerization [12]. Unlike formin, they cannot nucleate filaments [13]. On the other hand, actin-depolymerizing factor (ADF)/cofilin can sever a filament into two pieces [14] (Fig. 1.1E). Interestingly, recent research suggests that the segment that contains the original pointed end will rapidly depolymerize due to the enrichment of ADP-actin, significantly enhancing the disassembly of actin networks [15].

Actin networks require motor proteins and crosslinking proteins to fulfill most

of their functions. In most animal cells, non-muscle myosin II (NMII) is the major force generator. NMII molecules assemble into mini-filaments that are hundreds of nanometers long, binding across actin filaments [16, 17]. The binding of NMIIs displays an interesting catch-bond mechanochemical property, where the binding becomes stronger as the external load acting on NMII increases. By hydrolyzing ATP, NMII mini-filaments are able to walk along filaments, converting the chemical energy into mutual shearing forces. Similar to filament treadmilling, motor-driven shearing is also polarized, where NMIIs walks towards filament barbed ends. The force generated by NMII leads to large-scale centripetal movement of actin filaments towards a geometric center, which is often described as contractility. NMII driven contractility is indispensable for condensing and organizing actin networks into higher order structures [18–22]. The contractility can be amplified by passive crosslinkers [20,23–25], though recent researches suggest that crosslinkers can generate contractility in the absence of motor [26,27]. There are several crosslinker types with various length and stiffness. For example, α-actinin is a 30-40 nm crosslinker that is widely found in motile cell interior and contractile bundles, while fascin is a much smaller crosslinker (~8 nm) that helps to form unipolar actin bundle in protruding filopodia [28]. In this thesis, we will mostly focus on forces generated by NMII and α-actinin.

The chemical activities of these cytoskeletal proteins are regulated via signaling pathways, which sense mechanical or chemical cues inside and outside cells. By inhibiting or over-expressing the activity of a particular protein and monitoring changes in cytoskeleton dynamics and structures, researchers have discovered

several important signaling pathways that connect stimuli from environments to cytoskeletal activities. Rho is a large family of small GTPases (guanosine triphosphate hydrolase enzymes) widely found in eukaryotic cells that plays essential signaling roles in actin dynamics. Rho GTPases trigger filament nucleation from Arp2/3 complex indirectly by activating Wiskott-Aldrich syndrome protein (WASP) and WAVE (WASP-family verprolin-homologous protein) family proteins [29, 30]. Actin polymerization at formin bound barbed ends can also be stimulated by Rho [7]. Moreover, Rho is also known for mediating the binding of myosin light chain through ROCK (rho-associated protein kinase) proteins [31]. Despite the complexity of signaling, their ultimate downstream effects may be simplified into a few basic elements. To explore fundamental principles underlying actomyosin dynamics and *in vivo* structure formation, we will focus on and directly manipulate these downstream effects in our computer model in this thesis.

Mechanically, actomyosin networks show interesting viscoelastic properties. At a short timescale, they behave like elastic crosslinked and branched polymer networks. The elasticity of actin network is controlled by factors such as filament length and the number and types of crosslinkers [32–34]. However, at a longer timescale, actin networks can rapidly remodel their structure to better sustain the mechanical environment, displaying fluid-like dynamics. Typical timescales for this type of viscous response range from around 10 s to minutes depending on the turnover timescale of cytoskeletal components [35–37], though certain types of crosslinkers turn over at sub-second timescale [38]. The fluid-like behavior is believed to regulate important biological functions such as promoting cell division [39] and drive cells to

migrate under water flux [40].

1.2 Actin structures and their chemical and mechanical dynamics

By consuming chemical energy stored in ATP and guanosine triphosphate (GTP), actin networks are able to produce, transfer, and sustain cellular forces by scaffolding from semi-flexible protein filaments into skeleton-like higher order networks. Actin structures in cells are also highly dynamic, allowing them to rapidly remodel themselves to adapt to different chemical and mechanical environments [28, 41]. As a consequence, actin cytoskeleton is indispensable for important cellular activities such as cell morphology controls [42], cell migration [43, 44], and cell division [45]. This highly dynamic feature also has significant impacts on the activity of non-cytoskeletal biomolecules, such as inducing surface protein clustering during immune activation [46, 47].

In this chapter, I will introduce the compositions, roles in cellular activities, and mechanochemical dynamics of three actin structure categories that are ubiquitous in cells: actin bundles, dendritic actin networks, as well as actin rings and cortices. In Chapter 2-4, I will present research projects focusing on these structures.

1.2.1 Contractile actin bundles - stress fibers

The actin bundle is a widely found actin scaffold *in vivo* that is responsible for force production and transduction. At the leading edge, actin filaments are bundled by fascin into unipolar bundles, filopodia, that protrude the cell membrane

to direct migration via rapid filament polymerization [48–50]. On the other hand, stress fibers are arranged as a bi-polar actomyosin bundle crosslinked by α-actinin, serving as the major contractile unit in most animal cells. A contractile stress fiber normally consists of two or more small crosslinked, unipolar actin bundles, and these filopodia-like small actin bundles are connected with reverse polarity [51]. Unlike filopodia, stress fibers are able to generate contractile force, potentially owing to this graded polarity pattern. Since myosin motors walk towards a particular direction, small actin bundles with distinct polarity can slide together under the shearing force generated by myosin, inducing contractility. In addition, stress fibers are often anchored to focal adhesion, enabling cell level force transduction and triggering mechanosensing [52, 53]. They also mediate cell migration due to the connection between focal adhesions and substrates or extracellular matrices [44, 54].

There are several types of stress fibers with distinct structures and localization. Dorsal stress fibers are unipolar bundles, which are normally generated by actin filament polymerization from focal adhesion [55]. Since filaments in dorsal stress fibers have their barbed ends attached to the focal adhesion site, their growth is restricted as they need to push against the focal adhesion complex. They also typically do not contain myosin II motors. As a consequence, dorsal stress fibers are normally short (around a few microns) and non-contractile [56]. Dendritic actin networks in the cell body may collapse into transverse arcs, which display a periodic α-actinin-myosin pattern. As introduced above, this graded polarity can generate contractile force, however, it is still unclear whether transverse arcs can transduce cellular forces due to the lack of connection with focal adhesion [28, 51]. The ven-

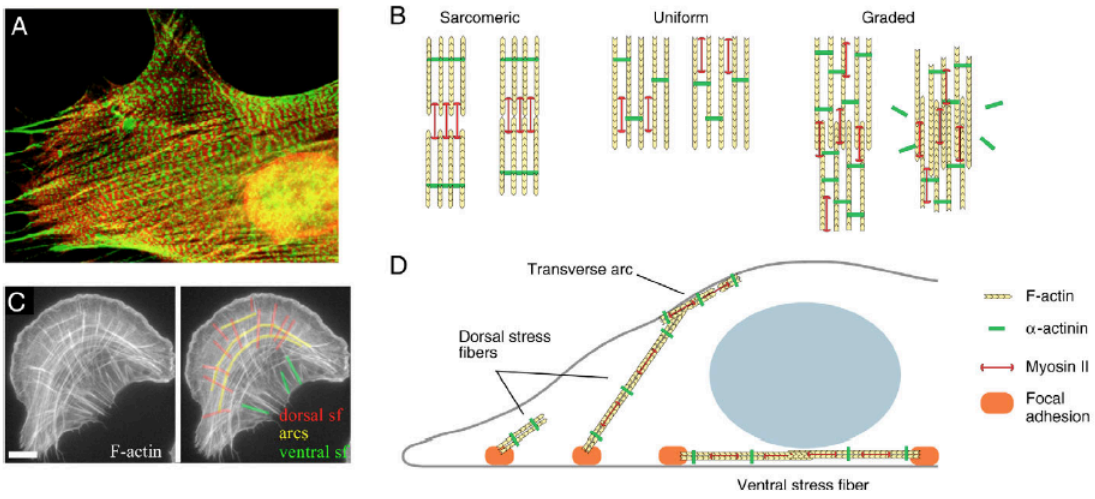

Figure 1.2: Structures of actin stress fibers.(A) The periodic polarity of stress fibers in gerbil fibroma cells. Non-muscle myosin is stained as red and α-actinin is stained as green. (B) Schematic representations of stress fiber structures consist of polarized actin filaments, non-muscle myosin motors and α-actinin crosslinkers. (C) Three categories of stress fibers in U2OS osteosarcoma cells with F-actin stained. (D) Model of stress fiber localizations in cells and ventral stress fiber formation. In this model, two dorsal stress fibers and connected by a transverse arc to form a ventral stress fiber. Image from Figure 1 in [44] with permission from Journal of Cell Science, The Company of Biologists Limited, Copyright (2007).

tral stress fiber is a "complete" stress fiber and the main force generator in many interphase cells as it connects to two focal adhesions that allow cellular force transduction. The ventral stress fiber is potentially created by connecting a transverse arc and two dorsal stress fibers [55], nevertheless, the molecular level mechanism is still poorly understood. Experiments have shown that stress fibers can be created and strengthened upon external mechanical stimuli [57], suggesting the formation of actin bundle can be trigger by extracellular mechanical cues. In Chapter 2, we will explore the actin microstructure reorganization and the stress fiber like bundle formation under tensile external force.

1.2.2 Dendritic actin networks – lamellipodia

The motility of cells relies heavily on a quasi-2D dendritic actin scaffold called the lamellipodium. Located at the leading edge of migrating cells, lamellipodia harness WASP/WAVE family proteins to activate Arp2/3 complex [28, 58, 59] (Fig. 1.3a-c). These activated Arp2/3 proteins nucleate many short branchers [9, 10] (Fig. 1.3d), generating protrusive forces that drive the cell to move by polymerization against the plasma membrane [5, 60]. The force generation from lamellipodia is very unique, since it neither relies on myosin motors nor does it requires filament bundling. Various experiments show that a stall force on the order of a few nN per 1 μm^2 contact area is required to stop lamellipodia driven motion [28, 61–63]. Moreover, lamellipodia can be strengthened by external load force. An *in vitro* experiment discovered that branched actin networks tend to grow faster after applying an external load force and then removing it [64]. This load dependent growth velocity is associated with the remodeling of dendritic actin networks, but a comprehensive understanding of how dendritic actin network remodeling is still lacking.

Capping proteins are a widely presented remodeling regulator in lamellipodia, playing an essential role in lamellipodia functionality. Interestingly, the presence of capping proteins does not hinder filament protrusion in the lamellipodium. On the contrary, capping proteins may be able to promote cell migration. Theoretical researches suggest that capping proteins, firstly, reduce the overall filament length, making protruding membrane more favorable than buckling filaments [60, 65], and secondly, promote the uncapped filament polymerization by conserving G-actin.

This effect can be very significant in lamellipodia, since capping proteins are more active when they are close to the plasma membrane due to signaling [66]. Since Arp2/3 branching competes with filament polymerization for G-actin monomers, capping filament barbed ends can also promote the branched filament density [35, 36, 67]. The synergistic effects between capping proteins and Arp2/3 complex may explain why lamellipodia are usually more dynamic than other actin structures. For example, the turnover halftime is ~ 10 s at the front of lamellipodia [43], much shorter than ~ 1 min turnover halftime of actin cortex [39, 42]. In Chapter 3, we will investigate how Arp2/3 complex and capping proteins regulate actin network turnover in detail using computer simulation.

1.2.3 Outward condensation - actin cortices and rings

In cells, actomyosin networks often form 3D shell-like or 2D ring-like structures. The most well known example of these structures is the actin cortex, which is a thin actomyosin mesh under the plasma membrane (Fig. 1.4). The actin cortex is highly contractile owing to the presence of myosin II motors and α-actinin crosslinkers [42]. Through tethering with the plasma membrane, cortical actin networks are able to generate contractile forces on cells that preserve cell shape and volume against osmotic pressure [68]. On the other hand, there are many ring-like actin structures, such as the contractile ring created during cytokinesis [69], belt-like actin networks formed in cell-cell junctions [70], and periodic ring pattern generated in axon [71, 72]. In this thesis, we focus on the actin ring formed when expressing

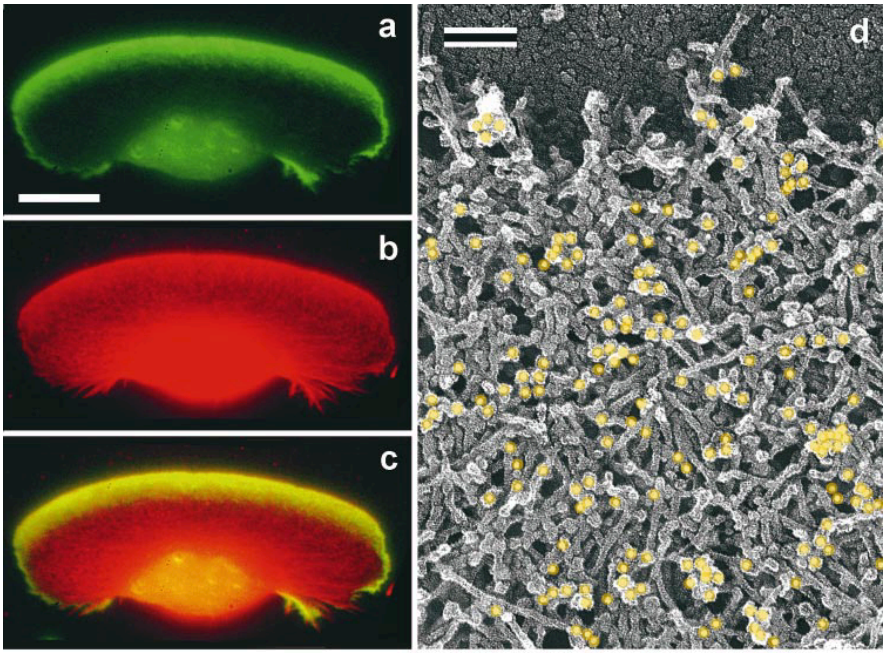

.

Figure 1.3: Localization and high resolution image of Arp2/3 complex and actin filaments in lamellipodia of Xenopus Keratocyte. (a-c) Arp2/3 is stained with p21 antibody in green and actin is stained with TRITC-phalloidin in red. (d) Immune electron microscopy of lamellipodia. 10-nm gold-conjugated secondary antibody (gold dots) reveals Arp2/3 locations. Scale bar: (a) 10 µm, (d) 0.1 µm. Image is adapted from Figure 3 in [10], with permission from Journal of Cell Biology, Rockefeller University Press, Copyright (1999)

immune cells on stimulatory substrates [73]. The formation of actin ring is an important process of immune cell activation, such as allowing the clustering of T cell receptors [74]. The actin ring has similar component as actin cortex, but can be as thick as several microns [47]. It is also more dynamic, undergoing a large scale of retrograde flow [46].

Interestingly, networks reconstituted from purified actin, myosin II motors and crosslinkers display distinct actin patterns compare to the shell-like and ring-like networks in cells. *In vitro*, the addition of myosin II and crosslinkers tends to induce large scale, inward clustering of actin networks. For example, Ref 21 shows

that the photo-activation of myosin motor in a thin actin layer induces condensation of actin filaments toward the network center. This condensation is often described as contractility, which is believed to be mainly generated by mutual shearing from myosin motors and is assisted by crosslinkers [41]. Increasing myosin or crosslinker concentration tends to enhance the global network contraction process [20, 24, 25].

The observation of centripetal collapsing *in vitro* is rarely observed in cells, and this "inward" condensation process seems to be contradictory to the formation of actin cortices and rings, which can be view as "outward" condensation. Why actomyosin networks form distinct patterns at steady state, and how actin rings and cortices can maintain their geometry against motor-driven contractility are still unknown. In Chapter 4, we will investigate the potential driving force that leads to this phase transition and explore the mechanism underlying actin ring or cortex formation.

1.3 MEDYAN: a simulation platform for active cytoskeleton

This chapter is partly adapted from: Qin Ni, Kaustubh Wagh, Arpita Upadhyaya and Garegin A Papoian. "Filament treadmilling induces phase transition in actomyosin networks" In preparation. (2020)

Computer simulation is a powerful tool to explore the complex dynamics of the cytoskeleton, and several models have been developed in the recent two decades. Cytosim is one of the most well-known cytoskeleton simulation tools, which has

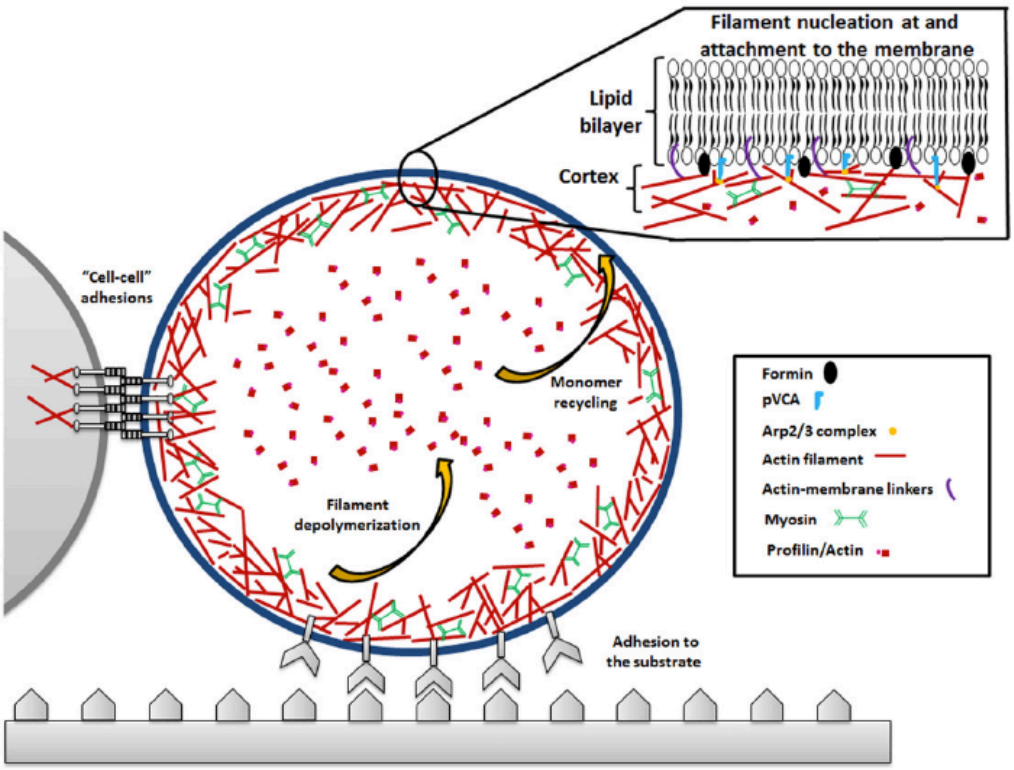

Figure 1.4: Sketch of actin cortex of an *in vitro* system mimicking cells. A thin cortical actin mesh is confined by the lipid bilayer membrane. Actin filaments undergo polymerization, depolymerization, and nucleation. The actin cortex is attached to the membrane by transient Arp2/3 complex and tethering proteins such as ezrin. The contractile cortex is subject to non-muscle myosin II activities. Image from Figure 4 in [75], with permission from Biochimica et Biophysica Acta (BBA) - Molecular Cell Research, Elsevier, Copyright (2015).

been used for numerous systems consisting of actin, microtubule, and associated proteins [76,77]. Recently, the model developed by Kim et al. [78] and an open-source 2D simulation software (called AFINES - Active Filament Network Simulation) developed by Freedman et al. [79] focus on elaborating the mechanical interaction of actin cytoskeleton. These models have been used to investigate the contractility and viscoelasticity of actomyosin networks [25, 80, 81]. On the other hand, researchers also employ mathematical modeling and fluid mechanics to explore the actin network dynamics [26, 68, 82].

Despite these efforts, most previous modeling works focus on mostly the mechanical interactions of the cytoskeleton and have no consideration or very coarse-grained treatments of chemical reactions. In active cytoskeletal networks, energy consuming chemical reactions and polymer mechanics are deeply coupled. Therefore, a desirable platform that can capture the active dynamics needs to consider the mechanochemical interplay between cytoskeletal elements. To achieve this goal, Popov et al. [20] developed the simulation platform MEDYAN (*Mechanochemical Dynamics of Active Networks*) based on several prior works from Papoian Lab at University of Maryland on modeling filopodia [48, 49, 83] and lamellipodia [60, 84]. MEDYAN integrates stochastic reaction-diffusion treatment of biochemical reactions and molecular transport, cytoskeletal polymer physics, with mechanochemical feedbacks at a single molecule resolution. With high computational efficiency and scalability, MEDYAN simulations of complex active networks can achieve the length scale of cells and timescales of thousands of seconds. A recent update also enables MEDYAN to track free energy dissipation from mechanical minimization and chemical events in actomyosin networks [85].

In MEDYAN, the simulation space is divided into a solution phase and a polymer phase. All diffusing molecules, such as G-actin and unbound molecules including myosin motor, crosslinker, formin, and capping proteins, are dissolved in the solution phase. To reduce the computational cost in modeling diffusion of particles without losing too much spatial information, the solution phase is discretized into many linear compartments. The dimension of the compartment is carefully chosen based on the Kuramoto length of actin, which is the mean-free path that

molecules are expected to diffuse before undergoing their next reaction [60]. Diffusing molecules are assumed to be well-mixed within each compartment without specific locations, and the transport of molecules between compartments is modeled as a diffusion reaction within the solution phase. On the other hand, polymeric filaments and bound molecules are modeled in the polymer phase that lies over the solution phase. This phase accounts for the mechanical modeling of boundary repulsion, steric interactions, bending and stretching of filaments, as well as the stretching of crosslinkers and motors. When polymerization, nucleation, motor, or crosslinker binding reactions happen, diffusing molecules will be transferred from the solution phase into the polymer phase. The depolymerization, filament destruction, and unbinding reactions will release molecules from the polymer phase to the solution phase. MEDYAN employs the Next Reaction Method [86] for the chemical evolution, which discretizes chemical master equation into stochastic events based on Gillespie based algorithm [87,88]. MEDYAN also takes care of mechanochemical feedbacks of cytoskeletal elements. Filaments, motors, and crosslinkers will update associate reaction rates based on their catch-bond or slip-bond features and mechanical environments. Filament polymerization against the boundary will be restricted by the boundary repulsive force, following the Brownian Ratchet model [89].

The relaxation time for local deformations of actin networks [90] is much shorter than the timescale of typical chemical events such as motor stepping [91] or filament polymerization [4], thereby creating a significant separation of timescales. Hence, the mechanical equilibrium process can be viewed as a pseudo-adiabatic process that can be separated from chemical reactions. Based on this hypothesis, the

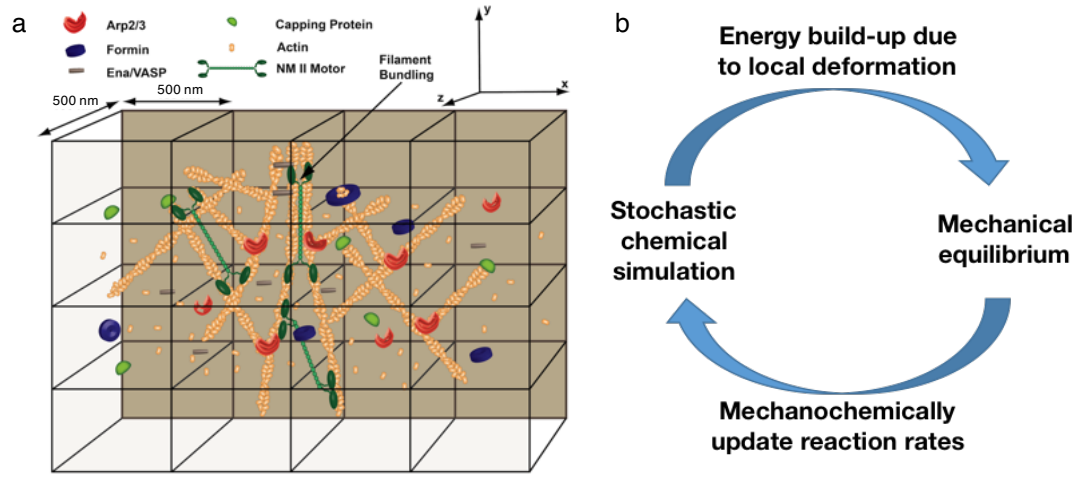

Figure 1.5: (a) The network space is divided into cubic compartments based on Kuramoto length, which is 500 nm for typical cytoskeletal proteins. Chemical reactions occur based on the local concentration of diffusive species in each compartment. Mechanical components of MEDYAN overlay the compartment. (b) MEDYAN simulation protocol goes as follows: (1) chemical reactions occur that evolve the time of the system stochastically; (2) pausing chemical reactions when the time step reaches a preset time value, and the system mechanically minimizes the total energy; (3) reaction rates are updated based on the mechanical conditions after minimization; (4) going back to step 1 based on the updated reaction rates. Image is adapted from Figure 1 and Figure 4 in [20], with permission under the terms of the Creative Commons Attribution License.

simulation can be carried out in the following protocol (also shown in Fig. 1.5b).

1. The system stochastically evolves the diffusion and chemical reactions using the Next Reaction Method.

2. Pausing chemical reactions after reaching a preset times step. The system computes the new mechanical energy based on the network deformation and then minimizes it.

3. Updating reaction rates based on the mechanical conditions after minimization following the mechanochemical models.

4. Going back to step 1 with the updated reaction rates.

A more detailed introduction of MEDYAN models can be found in [20]. The code and a usage guide can be freely accessed from http://medyan.org.

1.4 Outline of Chapters

This dissertation uses computer simulations to explore potential mechanisms underlying the assembly of *in vivo* actin architectures and investigate mechanochemical properties of these systems. The chapters are ordered based on the three main actin structures studied in this dissertation - actin bundles, dendritic actin networks, and actin rings and cortices as introduced earlier. Each chapter contains an introduction, results, and a discussion section. The main tool used in this dissertation is MEDYAN, which has been introduced in Chapter 1.3. Specific simulation setups and modifications to the model will be introduced in each chapter.

In Chapter 2, we investigate actin bundle formation under external force by using MEDYAN to mimic an Atomic Force Microscopy (AFM) pulling experiment, in collaboration with researchers from Georgia State University and Taxes A&M University. Our simulations and experimental results on smooth vascular muscle cells showed that exerting tensile external forces on a small portion of filaments is able to shape actin network into bundles. The bundle formation follows a two-step manner: tensile external forces first rapidly induce actin filament alignment along the force direction to form a bundle structure, and then myosin-driven contraction taken place at a longer timescale follows this anisotropic pattern that further consolidates the network into actin bundles.

In Chapter 3, we focus on the turnover dynamics of dendritic networks under the regulation of capping proteins and nucleators. In this work, we revealed how Arp2/3 and capping proteins regulate the treadmilling rate of individual filaments and the turnover of entire actin networks. Moreover, we distinguished the conceptual idea of filament polarized (de)polymerization, the treadmilling, from actin network turnover timescale measured from Fluorescence Recovery After Photobleaching experiment.

In the last project presented in Chapter 4, we look for the fundamental principle underlying the formation of distinct actomyosin patterns: actin cortices and rings in cells *versus* large clusters in reconstituted networks. We discovered that the filament treadmilling rate is a key tuning parameter that regulates phase transition of actomyosin network structures. With low treadmilling rates, actin networks form large, highly condensed clusters. On the other hand, networks from ring-like structures in quasi-2D cylinderical systems and cortex-like structures in 3D spherical systems as treadmilling rate increasing to *in vivo* level. This observation is supported by experiments on live Jurkat T cells by Dr. Arpita Upadhyaya's lab at the University of Maryland. In the end, we show that the formation of actin rings and cortices is potentially driven by condensation towards a higher shell volume region.

Chapter 2: Tensile force induced actin bundling

This chapter is adapted from: Xiaona Li [*], Qin Ni [*], Xiuxiu He, Jun Kong, Soon-Mi Lim, Garegin A Papoian, Jerome P Trzeciakowski, Andreea Trache, and Yi Jiang. "Tensile force-induced cytoskeletal remodeling: Mechanics before chemistry". ***PLoS Computation Biology*** *16(6): e1007693. (2020) [*]Co-first authors* [92]

Author contributions: X.L., Q.N., X.H., and Y.J. performed computer simulations and analysis (Section 2.2.2 to 2.2.4, and Figure 2.3 to 2.6). Q.N. and G.A.P. designed the computational tool (Section 2.4.5 and Figure 2.2). S.-M.L., J.P.T. and A.T. performed AFM experiments and data curation (Section 2.2.1 and 2.4.1 to 2.4.3, and Figure 2.1), and J.K. analyzed the experimental alignment data (Section 2.4.4, and Figure 2.1). X.L., Q.N., X.H., G.A.P., A.T. and Y.J. wrote the manuscript.

2.1 Introduction

Cells adapt to local mechanical stresses by converting mechanical stimuli into chemical activities that alter the cellular structure-function relationship and lead to specific responses [93–95]. Cellular response to mechanical stimulation is a balance between contractile elements of the cytoskeleton, cell-matrix adhesions, and extracellular matrix [96]. Although cellular mechano-transduction has been an active

field of research for a number of years, the process by which transduction of external mechanical signals across the cellular cytoplasm induce cytoskeletal remodeling is not well understood. The most important question in the field of mechanobiology is "how do cells sense and integrate mechanical forces at the molecular level to produce coordinated responses necessary to make decisions that change their homeostatic state?"

Vascular smooth muscle cells (VSMCs) provide an excellent model system to study the mechanotransduction process. The mechanism by which VSMCs sense and adapt to external mechanical forces that result in cytoskeletal remodeling (6-8) is critical for understanding arterial disease pathology. In vivo, they sense and respond to mechanical forces generated by pulsatile blood pressure changes through alteration of signal transduction pathways to induce remodeling of their cytoskeleton and adhesions [97]. Thus, VSMCs residing in the vessel wall are mainly subjected to circumferential stretch and axial stress [57,98,99]. Circumferential stretch generated by the pulsatile blood flow exerts dynamical mechanical stimulation on the vessel wall in a direction perpendicular to the direction of blood flow. This is a well-recognized mechanical stressor and its biomechanical effects were well studied [98, 99]. Axial stress in the vessel wall arises from longitudinal tethering of the arteries to surrounding connective tissue [100]. Even though axial stress (i.e., tensile force) has been known as an important mechanical stressor of the vessel wall for a long time [101, 102] and a fundamental contributor to vessel wall homeostasis [100], less attention was given to study its biomechanical effects at the cellular level.

In anchorage-dependent cells, external mechanical forces are imposed on a

pre-existing balanced force equilibrium generated by cytoskeletal tension [103–105]. Thus, forces acting on a cell will induce cytoskeleton deformation throughout the cell, such that the actin cytoskeleton remodels to better sustain the external load. Actin cytoskeleton consists of semi-flexible actin filaments, myosin motors, and crosslinking proteins. It has been proposed that de novo actin polymerization is critical for actin fiber formation in migrating cells [55], while the aggregation of existing actin filament fragments is most likely for stationary cells in a static environment [51]. Mechanical stimulation of stationary VSMCs in tissue represents an intermediate state, in which cells must dynamically adapt to their native, the mechanically active environment. It is not known which mechanism is favored in this normal functional homeostatic state. Moreover, research has shown that cells adapt to external force by activating mechanically-sensitive signaling pathways that involve conformational changes of proteins at cell-matrix adhesions (e.g., integrins, vinculin, talin, etc), and promote actin filament polymerization [106].

Previous works [107] by Trache and Lim on VSMCs suggested that cellular adaptation to the applied tensile force is a characteristic of the integrated cell system as a whole. To address how application of external tensile force induces actin cytoskeleton remodeling, we combined imaging techniques with simultaneous mechanical stimulation of single cells using fibronectin-functionalized atomic force microscope (AFM) probes [108]. Thus, we found that mechanical stimulation not only increases alignment of actin filaments, but also induces actin bundling measured by increased fluorescence intensity of F-actin [57].

Here, we build upon these experimental results and investigate the biome-

chanical effects of axial stress at cellular level using computational modeling, by asking how tensile force induces actin cytoskeleton adaptive remodeling? During the adaptation process, the actin cytoskeleton remodels to better sustain the external load [28, 42, 109]. Thus, actomyosin networks crosslinked by α-actinin and other crosslinking proteins are able to adapt to external forces via fast mechanical response, in which stress relaxation occurs on the timescale of seconds [18, 110–112]. However, cytoskeletal reactions, such as actin (de)polymerization or myosin II activation that continuously converts chemical energy into mechanical force, remodel the actin networks on a slower pace, on a time scale of minutes [36, 82, 113]. As a result of myosin dominant mechanochemical dynamics, actin networks tend to contract [85, 114]. Prior computational models have investigated remodeling of the actin cytoskeleton due to slower chemical reactions [48, 49, 80, 115, 116], however, how external mechanical stimuli induce the active formation of actin bundles is still poorly understood.

To better understand the detailed spatiotemporal dynamics of cytoskeletal reorganization due to external mechanical loading, we simulated the mechanical and chemical dynamics of the actin cytoskeleton using the MEDYAN (MEchanochemical DYnamics of Active Network) software [20]. In our simulations, we model the active cytoskeletal networks using polymer mechanics of semi-flexible filaments, crosslinking proteins, and motor proteins. A stochastic reaction-diffusion scheme was used to simulate chemical reactions, including myosin activation, crosslinking protein binding, and actin filament assembly. Additionally, we had applied external tensile forces to the actin network to mimic the AFM mechanical stimulation in the experiments.

In these systems, a few filaments were initially anchored to a simulated AFM probe, in addition to a free filament pool. The external force was applied by moving the simulated AFM probe, and the amplitude of z-axis displacement directly determined the magnitude of the force. In highly crosslinked actomyosin networks, the external force exerted on a small fraction of filaments would transmit to the entire system that changes their homeostatic state in microseconds [117]; this will be considered as the fast mechanical response. After each tensile force was applied, the system was allowed to evolve for minutes, such that we were able to study how the actin network adapts under a slower chemical response.

Both experiments and simulations suggest that the external tensile force applied on actin networks quickly induces alignment of actin filaments along the direction of force, and this directional alignment is independent of longer timescale chemical response. In addition, the formation of actin bundles as a result of external tensile force relies on both the faster mechanical response and the slower chemical response. We hypothesized that cellular cytoskeletal adaptation to external tensile forces and formation of actin bundles follows a "mechanics before chemistry" process.

2.2 Simulation Methods

A computational model for mechanochemical dynamics of active networks (MEDYAN) [20] was used to simulate the actin cytoskeletal network with an external tensile (i.e., z-axis) force. In this model, actin filaments are treated as "cylinders"

connected into chains. The cylinder itself is unbendable, and the radial deformation of filaments is realized by bending between two neighboring connected cylinders. Each cylinder consists of up to 40 actin monomers, where a full cylinder is 108 nm long and has 4 possible binding sites for myosin motors and crosslinkers. Myosin motors are modeled as harmonic springs that can walk towards filament plus end with equilibrium length from 175 nm to 225 nm based on the non-muscle myosin II (NMII) [16]. Crosslinking proteins are also modeled as harmonic springs with an equilibrium length for α-actinin (30-40 nm) [118]. The main chemical events we considered in this work include filament polymerization and depolymerization, binding and unbinding of myosin and crosslinker, and myosin activation. These reactions are mechanochemically sensitive and are modeled by an efficient Next Reaction Method based on the Gillespie algorithm [86, 88]. Simulation parameters and other model details can be found in Table A.1 and a previous publication [20].

We initialized a $3\times3\times1.25$ μm^3 simulation volume with a 250 nm radius semi-spherical AFM probe that attached to the upper boundary. At time 0 sec, 300 seed filaments, each with 40 monomers, were randomly created in the network, defined as the free filament pool. These filaments free from simulated AFM probe attachment are allowed to polymerize and depolymerize on either the plus end or the minus end. To appropriately transmit the external force generated by probe displacement to the actin network, additional 30 seed filaments were initialized with their minus-end attached to the simulated AFM probe via stiff harmonic springs (Fig. 2.2a). These filaments are allowed to polymerize and depolymerize at the plus end. Myosin II concentration is 2 μM (equivalent to 0.1 μM NMII mini-filament)

and α-actinin concentration is 2 μM, based on their concentrations reported in Dictyostelium discoideum [45, 119, 120]. We use a concentration of 20 μM for actin, which is consistent with the physiological concentration of 24 μM actin [121, 122]. The concentrations of actin, motors, and crosslinkers in the computational model are also used in prior computational modeling works [20, 116]. Based on an earlier work using MEDYAN, these concentrations are adequate for filament bundle to maintain their structure [116]. At the start of simulations, free G-actin was added to the network to ensure the total actin concentration is 20 μM. Since the concentration is much larger than the critical concentration [123], seed filaments would grow rapidly and reach an average F-actin length of $\sim 8\mu$m in a few seconds of simulation. Myosin motors and α-actinin crosslinkers were added after 5 seconds of simulation. The addition of myosin and α-actinin linkers connect the free filament pool to the filaments attached to the probe.

The external tensile force from the AFM probe was implemented as follows. The network was allowed to evolve for 150 s before the AFM probe vertical displacement (i.e., tensile force on z-axis). Each probe displacement created a 250 nm or 500 nm step displacement of the AFM probe, applying tensile force to the AFM probe-attached filaments via stiff harmonic springs. To ensure the energy was properly minimized, each displacement step was broken up into 100 sub-steps (2.5 nm or 5 nm displacement per 0.01 s). Networks were mechanically equilibrated after each sub-step, and displacement would create additional simulation space by raising the upper boundary. Since all AFM probe displacements were finished in 1s and each mechanical minimization was instant in the simulation, we were able to treat

the network change before and after displacement as a fast, mechanical response that is independent of chemistry. Networks were allowed to evolve for another 150 s before the next probe pulling step (Fig. 2.2b). During the 150 s period, cytoskeletal network remodeling was Chemically dominated by filament treadmilling, myosin activation, and α-actinin linker binding and unbinding. Since the time interval between two displacement steps is much longer than the pulling time (1 s), we define the network evolution during each 150 s as the long timescale Chemical response. We applied the AFM-probe pulling 5 times, for a total of 900 seconds, during each simulation. Table A.1 lists all the modeling parameters.

The present work tested four different tensile force conditions. For convenience, we labeled them as Case i-iv in decreasing order of displacement sizes (Fig. 2.2b). In Case i, a constant 500 nm step size was applied. This step size exerted an instantaneous force on the AFM-probe attached filaments. In Case ii, we used mixed step sizes: in the first three pulling events, each step generates 250 nm displacement, and in the last two pulling events, each step generates 500 nm displacement. In Case iii, we reduced the displacement size to constant 250 nm, implying a weaker external force. In the last case, we did not apply any external force to the network, hence, all 330 filaments were in the free filament pool. However, the upper boundary in Case iv would still move up in the same way as for Cases i to avoid any problems due to the boundary effects.

2.3 Results

2.3.1 Actin cytoskeleton reorganization in live VSMCs under mechanical stimulation reveals a two-step adaptive response

Andreea Trache and Soon-Min Lim at Texas A&M University performed the experiments on VSMCs. Live VSMCs expressing mRFP1-actin-7 were subjected to the mechanical loading delivered by the AFM probe (Fig. 2.1a). The mechanical loading was a vertical force (along the z-axis) force that applied to a small area (circular diameter is approximately 5 µm) at the apical cell surface through a fibronectin (FN) functionalized probe. This force induced cytoskeletal remodeling by pulling on cortical actin through a FN-integrin-actin linkage [57, 107]. Cell responses to the probe displacement and the florescent intensity of actin bundles over time were recorded using spinning-disk confocal microscopy. Detailed experimental methods can be found in the Appendix A. The reconstructed 3D-images of the actin cytoskeleton were used to segment actin bundles in 3D (Fig. 2.1b & 2.1c). We used these 3D bundles to calculate an average fiber alignment index in the direction of the pulling force. The alignment index is defined as the average of $\cos(\theta)$, where θ is the acute angle between each filament segment and the direction of the force (Z-axis) (Equation 1 in Appendix A1.4). With a value between 0 and 1, the alignment index equals to 1 for perfect alignment with the Z-axis, and 0 for alignment perpendicular to the Z-axis. The alignment index increases right after the application of an external force, but levels off (Fig. 2.1e) upon larger pulling forces. Note that the

small alignment index value is due to the cell aspect since the VSMCs lay flat on the substrate, and the majority of the filaments were perpendicular to the Z-axis. In addition, the normalized actin fluorescence intensity of the cell increased steadily as the AFM displacement continued (Fig. 2.1f). A second pulling was carried out at 3000 s (Fig. 2.1d), however, it did not trigger further increment in alignment index and intensity (Fig. 2.1e-f), which potentially indicates the pulling reaches the maximum effect after the first pulling event. These experimental results show a force-induced actin cytoskeleton remodeling via the directional alignment and actin fiber bundling.

2.3.2 Rapid formation of actin bundles in response to tensile force in MEDYAN simulations

To understand the molecular mechanisms of the actin cytoskeleton reorganization under tensile force application using the AFM probes, we designed computational simulations of actin networks with external tensile force using MEDYAN software. We generated 300 free filaments in a $3\times3\times1.25\ \mu m^3$ simulation box, initially as a random network, and another 30 filaments attached to an AFM probe located at the center of the upper boundary of the simulation box. The number of AFM attached filaments was chosen based on the reported number of filaments in actin bundles [51]. The simulation box contained 20 μM of actin, 2 μM of non-muscle myosin II (NMII), and 2 μM of α-actinin crosslinkers. The simulated AFM probe was displaced by a distance d, every 150 seconds. Each pull (Z-axis tensile

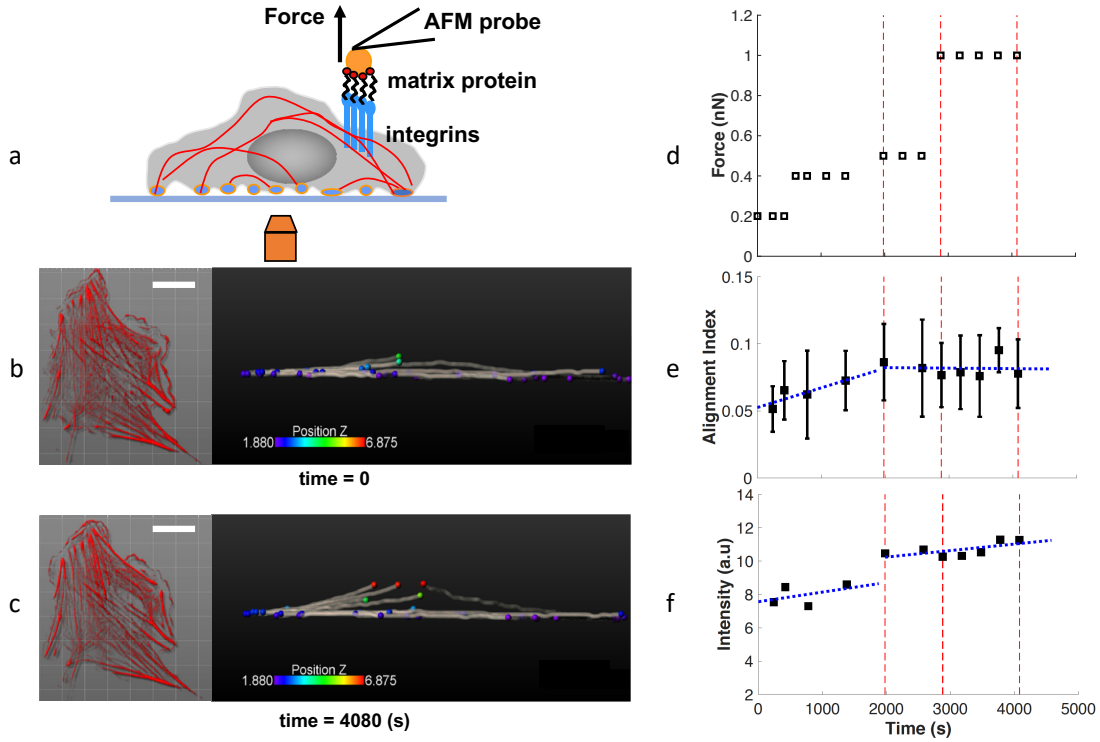

Figure 2.1: Response of VSMC to external pulling force. (a) Schematic of a VSMC mechanically stimulated with a FN functionalized AFM probe and simultaneously imaged by spinning-disk confocal microscopy. (b) Fluorescence images of VSMC expressing mRFP1-actin-7 (left) and the 3D reconstructed image of the representative segmentation of actin filament bundles (right) for before the AFM probe displacement at time 0 min (b), and after the AFM probe displacement at time 68 min (c). Scale bar: 20 μm. (d) The scheduled pulling force in three phases: small, intermediate and large forces. (e) The alignment index for the actin filament bundles increased rapidly as small force was applied, but slowed down as the force increased. (f) The normalized intensity for mRFP1-actin-7 increased steadily through all force ranges. Blue lines: piece-wise linear fit for forces below 0.5 nN and $\geq$ 0.5 nN.

force application) created a 250 nm or 500 nm step displacement of the simulated-AFM probe, generating tensile force on the filaments attached to the probe via stiff harmonic springs (Fig. 2.2a). The amplitude of step displacement size d is linearly proportional to the pulling force of the AFM probe. Chemical interactions, including filaments treadmilling, myosin activation, and α-actinin crosslinking, took place throughout the simulations. We varied the pulling patterns (Fig. 2.2b) to simulate the different pulling forces in the experiment (Fig. 2.1d).

Interestingly, pulling on only a small fraction of AFM-attached filaments is sufficient to alter the actin filament structure of the entire network. After 900s and five AFM probe pulling steps, each with d=500 nm (case i), the actin networks reorganized into a bundle (Fig. 2.3a), which is approximately 2 μm long and around 500 nm thick. These actin bundles have mixed filament polarity, i.e., plus ends or minus ends of filaments are randomly distributed (Fig. A.1). In contrast, actin networks free of external force geometrically collapsed into a globular cluster-like structure (Fig. 2.3b), as a result of contractility driven by myosin motors and crosslinkers. Reducing the step size d in Cases ii and iii creates an intermediate geometry between the bundle and cluster (Fig. A.2). If the step size is further reduced to 0, but the 30 filaments are maintained attached to the simulated AFM probe, the geometry would be similar to the cluster (Fig. A.3). Moreover, if we release the filaments from the simulated AFM probe after bundle formation, then actin bundles would also tend to collapse into globular clusters (Video 1).

The actin bundle formation was also regulated by the number of actin filaments attached to the AFM-probe. When too few filaments were attached to the AFM

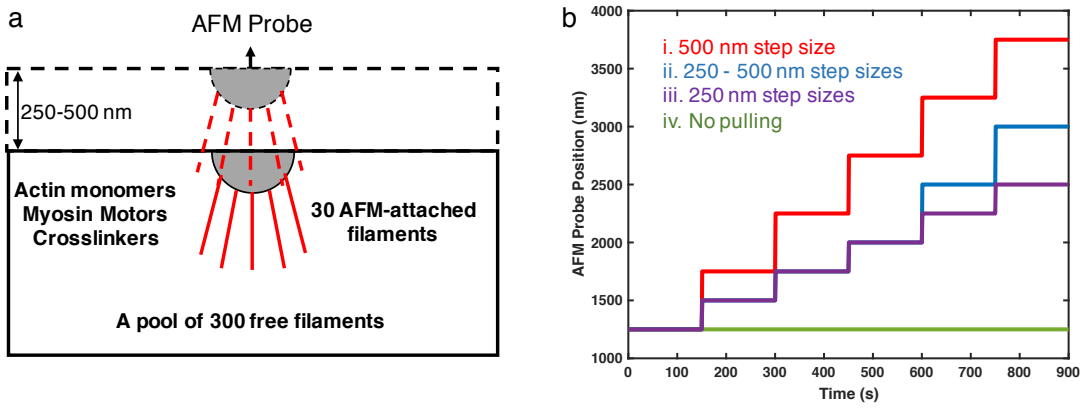

Figure 2.2: (a)A sketch of the simulation setup. The simulation box is 3 μm in x and y directions, and the initial height (z-direction) is 1.25 μm. The simulation box contains 300 free actin filaments, as well as diffusible G-actin, myosin, and α-actinin linkers. A semi-spherical AFM probe is located at the upper boundary, and 30 filaments are attached to the probe via stiff harmonic springs. At the beginning of simulations, all filaments are 0.108 μm long (containing 40 actin subunits). The input G-actin concentration is much higher than the equilibrium concentration, making actin filaments rapidly elongate. An average length of 0.8 μm is achieved and maintained after around 40s of simulation. (b) Simulated AFM-probe position, equivalent to the height of upper boundary, as a function of time for Cases i-iii. The control case (Case iv) is without AFM probe and without filament attachment, with only the upper boundary moving in the same way as in Case i to avoid potential boundary effects.

probe, the pulling force was insufficient to generate a bundle (Fig. A.4a). In some of the simulations, after pulling, the actin filaments that were attached to the AFM-probe would disconnect completely from the free actin filament pool. For the myosin motor and α-actinin concentrations used in our simulations, we found that about 20 actin filaments need to be attached to the probe for actin bundle formation. On the other hand, increasing the number of AFM-probe attached filaments lowered the density of the free filaments. As a consequence, most free filaments could only collapse into small globular clusters locally and were unable to join the actin bundle formed by the filaments attached to the AFM-probe (Fig. A.4b).

2.3.3 Tensile force induces actin alignment in MEDYAN simulations

To investigate actin filament alignment during actin bundle formation, we calculated the alignment index $\cos(\theta)$ as described in the experimental section. The alignment index increases immediately after each of the AFM-probe pulling events in all three pulling patterns tested (Fig. 2.3c, Case i-iii). In the simulation, mechanical equilibration is instant, therefore these rapid jumps suggest very strong mechanical responses. Moreover, the directional filament alignment is regulated by the magnitude of the external tensile force, since reducing the pulling step size amplitude (compared to Cases ii and iii) results in a weaker alignment response. On the other hand, the directional alignment barely changes during the 150 s window between two pulling events (noted as the long timescale response). Since the long timescale response is regulated by slower chemical evolution events, we hypothesize that the directional alignment of actin filaments in response to tensile force is primarily due to fast mechanical adaptation.

2.3.4 Two-step development of actin bundles depends on both faster mechanical alignment and slower chemical response

To further analyze the formation and evolution of actin bundles, we next defined a cylinder-shaped boundary under the AFM probe (500 nm in diameter). More than 80% of the total F-actin accumulated within this boundary towards the end of simulations under the Case i pulling condition, suggesting that monitoring F-actin's

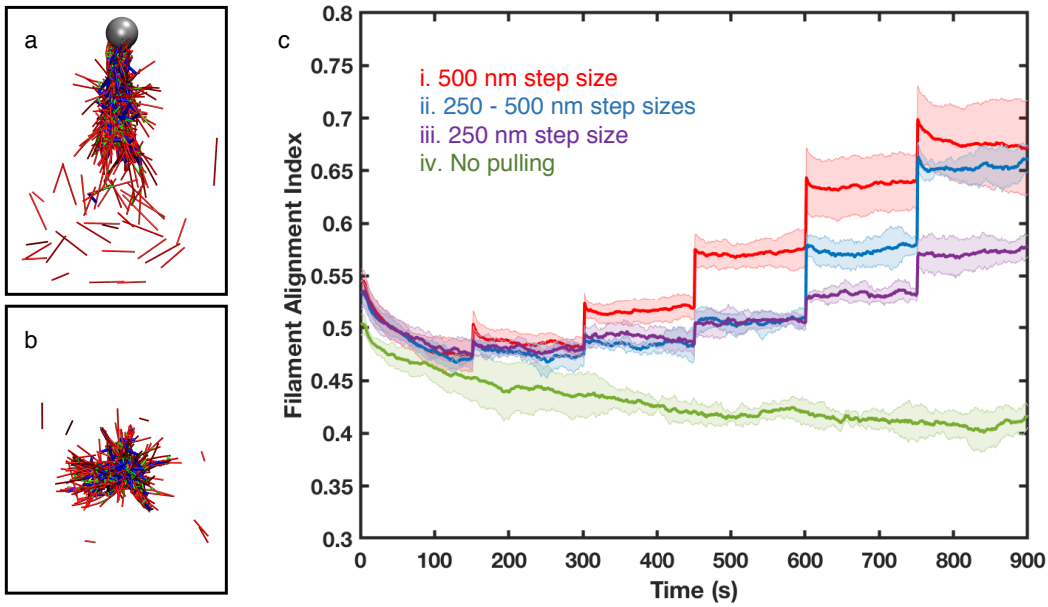

Figure 2.3: (a-b) Representative snapshots of (a) bundle-like actin networks under Case i pulling condition at time t = 900 s, and (b) cluster-like actin networks without external force at time t = 900 s. Actin filaments, myosin motors, and crosslinkers are shown in red, blue, and green cylinders, respectively. The gray sphere in (a) represents the AFM probe. (c) Filament alignment index along the Z-axis for 500 nm step size (red, Case i), mixed step sizes (250 nm for the first three pulling events and 500 nm for the last two, blue), 250 nm step size (purple, Case ii) and no AFM-probe pulling (green, Case iii). α-actinin linker:actin is 0.1 and myosin:actin is 0.005 in all simulations. Error bars represent the standard deviation from the mean in 5-10 simulation replicates.

accumulation in the bundle region provides a simple but robust way to quantify the bundle development process. We observed instant F-actin accumulation after each pulling event (Fig. 2.4a), while reducing step size hindered the accumulation (Fig. A.2a). Similar to the directional alignment, these results suggest that actin bundle development relies on the fast, mechanical response.

Surprisingly, the accumulation of actin filaments into the bundle kept increasing steadily between pulling events, suggesting that slower chemical dynamics contribute to bundle development as a result to the adaptation to force. To capture the

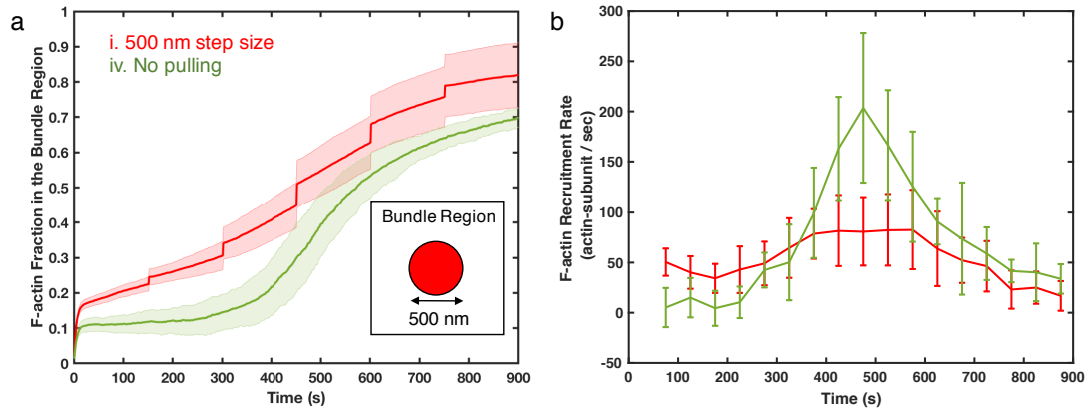

Figure 2.4: (a) The F-actin fraction in the bundle region as a function of time for actin networks under 500 nm displacement steps (red, Case i) and actin networks free of external force (green, Case iv). The bundle region is defined as the volume under the simulated AFM probe, which is a cylindrical region of 500 nm in diameter and the height of the simulation box. The box size varies over time based on the position of the AFM probe. Insert shows a 2D illustration of the bundle region. (b) The rate of F-actin accumulation in the bundle region from simulations with the AFM probe pulling force (red, Case i) and without AFM probe pulling- force (green, control Case iv). The recruitment rates are calculated by linear-fitting of the data points every 50 seconds. Shaded colors and error bars are the standard deviations of 10 replica simulations for Case i and 5 replicas for Case iv, respectively.

long timescale of F-actin recruitment, we calculated the F-actin recruitment rate in the defined bundle region (Fig. 2.4b). The control case without external pulling (Case iv, green line) also shows sharply F-actin recruitment as a result of myosin and α-actinin induced contractility and bundling. Similarly, the recruitment rate of F-actin during the intervals between pulling (Case i, red line) is always positive, showing net recruitment of F-actin. The rate of F-actin recruitment for bundling is lower than that for the actin clustering into globular foci in the control case.

To further explore the significance of chemical evolution of bundle development, we tested three different conditions with "insufficient" chemical evolution. First, we reduced the myosin concentration from 2 μM to 0.4 μM. Without sufficient

myosin, the network was unable to generate enough contractility of the actomyosin network, leading to high actin filament dispersion (Video 2). Second, by reducing α-actinin crosslinker concentration from 2 μM to 0.4 μM, the F-actin network could not form properly (Video 3). Although myosin motors still generated contractility, the actin fiber network is fragmented as disconnected actin foci. Lastly, we shorten the time between each pulling from 150 seconds to 10 seconds. Only a small fraction of actin filaments bundled together and followed the upward movement of the simulated AFM probe, disconnecting from the rest of the filaments (Video 4).

F-actin distribution further showed that the tensile force application using AFM-probe immediately stretches the actin fiber network along the direction of force (Fig. 2.5a-c), leading to a wider F-actin distribution in the Z-direction. As a result, the standard deviations (σ) of these distributions increased right after pulling (Fig. 2.5e). When we measure the radius of gyration (Rg) to quantify the cluster size of actin networks, we also find instantaneous jumps similar to those in the filament alignment and recruitment results (Fig. 2.5f). These instant stretches eventually shape actin networks into thinner actin bundles. Furthermore, these actin bundles maintain their geometric structures at a longer timescale. The F-actin distribution of actin bundle networks shifts slightly towards the force direction after 150 seconds of chemical evolution (Fig. 2.5a), but the shape and the standard deviation from the mean, σ, remain almost the same (Fig. 2.5d-e). In addition, the contraction rate, measured as the rate of Rg change ($\dot{R}_g = \frac{\Delta R_g}{\Delta t}$), is much slower than that for the actin globular clusters in the control case without force application (Fig. 2.5g). These observations are consistent with the slower F-actin accumulation rate in the

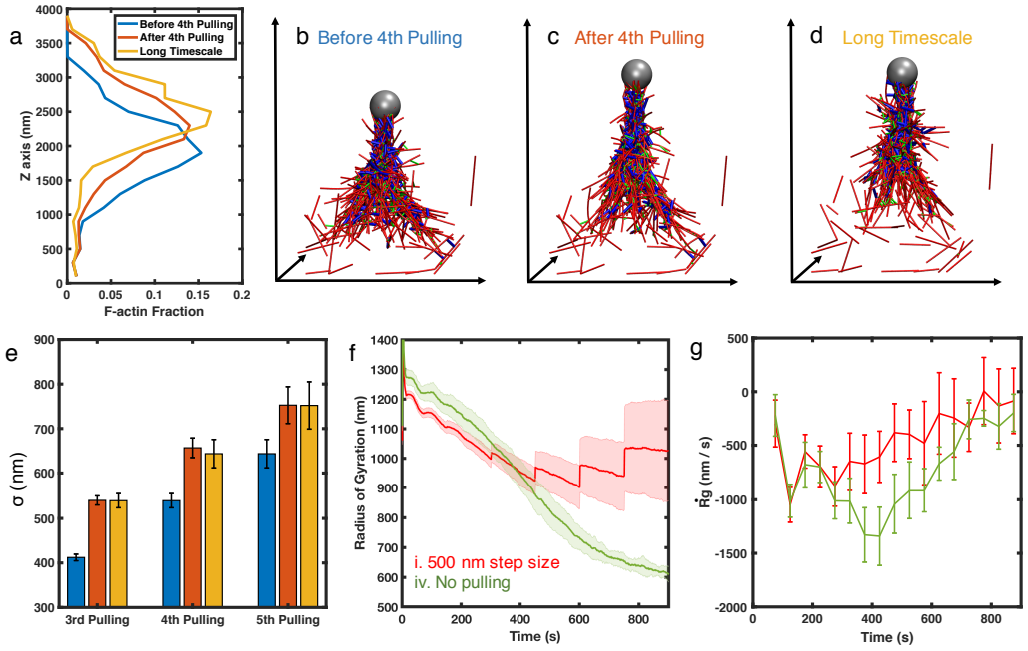

Figure 2.5: (a) F-actin distribution along the force direction (Z-axis) of the most representative trajectory before the 4th pulling at t = 600 s (blue), after the 4th pulling at t = 601 s (orange), and after the long-timescale chemical evolution at t = 750 s (yellow). (b-d) Corresponding simulation snapshots before pulling, after pulling, and after chemical evolution, respectively. (e) Standard deviations (σ) of the F-actin distribution along the force direction before pulling (blue), after pulling (orange), and after 150 s of chemical evolution (yellow) at the third, fourth, and fifth pulling events. σ are averaged over 10 duplicated trajectories, and error bars represent the standard errors. (f) The radius of gyration, Rg and (g) the rate of Rg change, $\dot{R}_g$, of actin networks in Case i with 500 nm pulling (red) and in Case iv without pulling (green). Shaded colors and error bars are the standard deviations of 10 duplicated trajectories for Case i and 5 duplicated trajectories for Case iv.

bundle region, as shown in Fig. 2.4b, suggesting that the actin bundle structure is more stable than the actin cluster. These results are also in agreement with the fact that the actin bundle can preserve its shape and would not contract into clusters under myosin driven contractility at longer timescale.

2.4 Discussions

Mechanotransduction is the process by which cells convert mechanical stimuli into biochemical activity. A key aspect of the mechanotransduction is that cells remodel their cytoskeleton in response to mechanical stimuli. To study external force-induced adaption of the actin cytoskeleton, AFM was used to apply external, tensile forces on single cells adherent on a substrate. Cell responses measured through probe displacement over time are directly dependent on the intrinsic contractility that modulates the function of the actomyosin apparatus. The observed rapid rise in actin fiber alignment upon tensile force stimulation contrasts with the continuous growth of actin fluorescence intensity, leading to our hypothesis of "mechanics before chemistry": fast mechanical stimulation-induced actin bundle alignment, followed by a slower chemical driven process to stabilize the actin bundle structure.

To explore this hypothesis, we developed a new feature in the MEDYAN software that mimics the conditions of our AFM mechanical stimulation experiments. Our simulation results reveal that tensile force triggers a rapid mechanical adaptation of actin networks that induces actin filament to align along the direction of force application, and promotes actin bundle formation. We also found that slower chemical evolution is essential to the formation of actin bundle, which requires the integration of actin networks through α-actinin crosslinking followed by myosin activation and eventual further actin recruitment to the bundle. Moreover, we found that actin bundles generated in our simulations are stable since they contract much

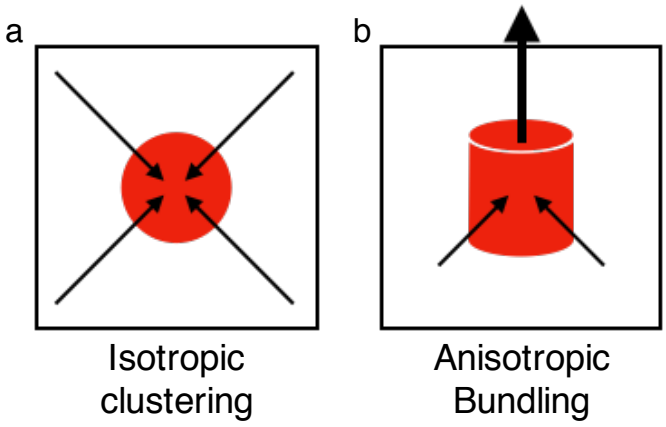

Figure 2.6: Motor-driven chemical evolutions generate contractility that induces the geometric collapse of the actin network. In random networks without external forces, the geometric collapse would be isotropic, causing filaments to cluster into globular foci (a). However, the external tensile force inducing filament directional alignment that favors anisotropic chemical evolutions, results in filament bundling (b).

slower than networks free of external force.

Thus, our simulations agree with the experiments, supporting a "mechanics before chemistry" hypothesis as an alternative two-step explanation regarding how active cytoskeletal networks adapt to external mechanical stimuli in real-time. In the control case of actin networks without external forces, actomyosin network contraction does not have a bias towards a specific direction, leading to an isotopic collapse into globular actin clusters (Fig. 2.6a). The external tensile force first stretches the actin cytoskeletal network, forcing filaments to align, as a rapid mechanical response, which initializes anisotropic actin bundle-like structures. Longer time scale chemical processes further stabilize the actin bundle structures that can preserve the anisotropy (Fig. 2.6b). As a result, the contractility generated by subsequent chemical evolution follows the anisotropic distribution, which strengthens actin bundles by recruiting more actin filaments while maintaining the bundle

shape.

Actin cytoskeleton plays a crucial role in maintaining cellular shape and supporting force transmission to and from extracellular substrates. Numerous studies have demonstrated the direct coupling between mechanical forces and chemical signaling. Mechanical stretch alters conformation of integrins such that their cytoplasmic β-tails provide binding sites for focal adhesion proteins [124] and further induce assembly of an adhesion complex at the site of force application [125, 126]. This process is followed by actin stress fiber remodeling, which is necessary to redistribute physical forces needed for cell contraction and to enable cell adaptation to the extracellular microenvironment [127, 128]. Moreover, sensing of substrate stiffness via integrins further triggers the adaptation of cellular cytoskeleton in less than 100 ms [129], proposing a 'mechanics first' mechanism of cellular response that supports our hypothesis. Thus, when the cell experiences an external force, the cytoskeletal adaptation will first elicit the actin fiber rearrangements (mechanical) before spending ATP to initiate the chemical reactions (chemical).

This work also suggests that motor-driven contractility potentially plays an indispensable role in the stress fiber formation. To form a stress-fiber-like actin bundle, the number of myosin and other accessory proteins such as crosslinkers should generate sufficient contractility that can contract the network over at a similar speed as external force induced deformation. Comparing to stress fibers that consist of 10-30 filaments [51], actin bundles in this work are thicker. In the simualtion, the upper section of the bundle has around 30 actin filament, which are the AFM attached filaments, and the bottom section has more filaments that does not tightly

bundle together. The thickness of the bundle may be regulated by the step size of AFM pulling event, where a larger step size may decrease the bundle thickness, and an filament adhesion site at the lower part of the network may help to bundle the network. The thinner upper region *versus* thicker lower region topology may be linked to the shear thinning of the gel-like actin network. In addition, there may be a maximum tensile force that an bundle can endure. The binding between AFM probe and actin cytoskeleton is realized through non-covalent bond among matrix proteins, integrins and cytoskeletal proteins, and a large enough force should be able to induce the disconnection between cytoskeleton and AFM probe. In the priming stage of experiment (before 2000 s), a small pulling force of 0.4 pN did not trigger significant alignment or intensity change, indicating there may be also a minimal force threshold to trigger the cytoskeleton remodeling. What are these maximum and minimum force thresholds for actin bundle remodeling and how they are regulated should be investigated in the future.

It should be noted that the alignment in the experiment was measured based on actin bundle, but the alignment in the simulation counts the orientations of all filaments. It is infeasible to measure the alignment of actin filaments in the experiment due to resolution limit, and it is also impractical to simulate a system contains multiple bundles due to the high computational cost. Therefore, we did not attempt to directly compare experimental results with simulation. Instead, the experiment is more of an inspiration for the simulation design.

In summary, we integrated in vitro cellular biophysical experiments with in silico modeling to investigate the effects of external load on the actin cytoskeleton

network. The experimental data and our modeling results suggest that under tensile force actin filaments align first, and then contractility induced by chemical evolution takes place to further restructure the cytoskeleton. The mechanical stimulation of stationary cells (in vitro or in tissue) represents an intermediary state of dynamic adaptation to stress of stationary cells placed in a mechanically active environment (i.e., vessel wall). Thus, our results suggest that in this intermediate cellular state, short timescale mechanical structural adaptation operates before chemical evolution necessary to further remodel the actin network. This study lays the groundwork for further studies related to predicting cellular adaptation to mechanical stimulation, which will be important for understanding diseases that involve changes of cellular stiffness, e.g., in cancer, hypertension and aging.

Chapter 3: Exploring Actin Filament Assembly in Dendritic Networks

*This chapter is adapted from Qin Ni and Garegin A Papoian. "Turnover versus treadmilling in actin network assembly and remodeling". **Cytoskeleton**. ; 76: 562– 570. (2019)* [36]

3.1 Introduction

Cells move and adapt their shape to the environment by relying on rapid turnover of their actin cytoskeletal network. These remodeling processes are intricately regulated by numerous actin-binding proteins, such that distinct cytoskeletal microarchitectures and functional behaviors emerge depending on the cell type or the environmental conditions [28, 130, 131]. For example, motile cells on a flat substrate project pseudo-two-dimensional protrusions, called lamellipodia, based on a rapidly remodeling, dendritic actin mesh [43, 60]. Many cells contain another important actin structure under the plasma membrane that establishes cell's morphology, called the cortex, which turns over at significantly longer timescales [42, 132]. On the other hand, the turnover of *in vitro* actin networks is usually much slower than in living cells, which, in turn, leads to yet another set of distinct geometric and

mechanical patterns [15, 21, 24].

The turnover dynamics of actin networks are driven by many processes, including growth and depolymerization of actin filaments, branching and growth of daughter filaments, and *de novo* nucleation of new filaments from the cytosol. Kinetics of an individual actin filament are highly polarized, the barbed end favoring monomeric actin (G-actin) association, while the pointed end undergoing preferential dissociation, producing net filament treadmilling towards the barbed end direction [3]. Treadmilling causes filaments to act like motors by converting chemical energy into mechanical force that is responsible for important cellular activities such as protruding the plasma membrane [5, 133]. Often treadmilling is viewed as being nearly synonymous to turnover, however, the latter being defined phenomenologically via Fluorescence Recovery After Photobleaching (FRAP) experiments [37, 39, 43, 134]. In this work, we carefully distinguish between these two phenomena, finding instances where they are clearly distinct.

The same processes that govern turnover dynamics of actin networks also regulate their mechanical behaviors. For example, force generation in highly dendritic networks is quite different from networks lacking nucleators, which are comprised of long unbranched filaments. In the cases of the former networks, such as found in lamellipodia, Arp2/3 is activated at the leading edge, driving branching of numerous short filaments that generate strong protrusion forces [28, 60, 84]. Furthermore, to maximize force generation, elongation of filaments has to be curtailed [35]. Therefore, how turnover is regulated in dendritic *versus* unbranched networks has important implications on the fundamental mechanisms of force generation in these

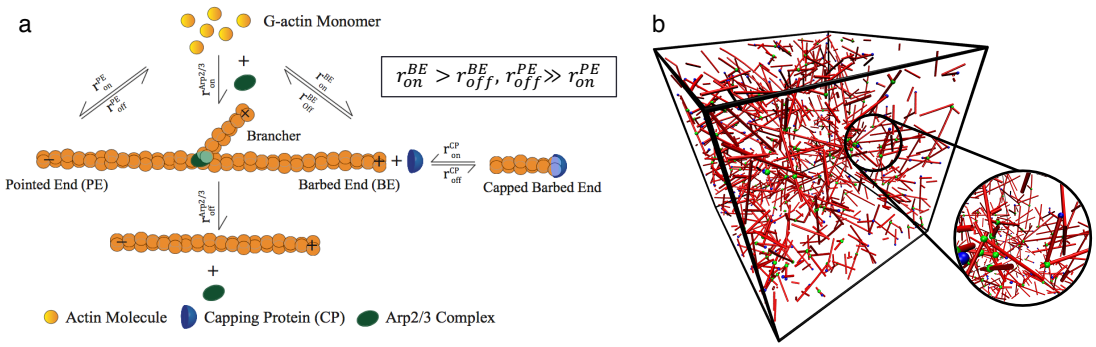

Figure 3.1: (a) A schematic diagram illustrates the list of reactions governing dendritic actin network growth studied in this work. Actin assembly and disassembly occur at the both ends of a filament: at the barbed end actin polymerization is faster than depolymerization, leading to filament elongation; however, the polymerization at the pointed end is insignificant, resulting in filament shortening. Arp2/3 complex binds to a preexisting mother filament and nucleates a daughter filament with capped pointed end. Arp2/3 complex can dissociate from the pointed end of a brancher and release a free pointed end. Capping protein (CP) binds to free barbed end and terminates both polymerization and depolymerization. (b) A snapshot is shown from a MEDYAN simulation of an $2\mu m \times 2\mu m \times 2\mu m$ dendritic actin network comprised of C_{actin} = $15\mu M$, $C_{Arp2/3}$ = $50nM$ and C_{CP} = $50nM$. Actin filaments are drawn as red cylinders; bound Arp2/3 molecules are drawn as green spheres; and bound CPs are drawn as blue spheres.

systems.

Treadmilling of an individual actin filament is intricately regulated by various proteins. For example, it can be disrupted by capping protein (CP), which attaches to the filament barbed end and terminates barbed elongation [28, 35]. On the other hand, direct nucleation from cytosolic G-actin is extremely slow, therefore requiring assistance of nucleators, such as Arp2/3 or formin. Arp2/3 complex branches daughter filaments from preexisting mother filaments, helping to generate a dendritic network [30], while formin can directly nucleate linear filaments by aggregating G-actin monomers [7, 135]. In prior experimental works, actin turnover dynamics investigated using FRAP relied on simple mathematical models to in-

terpret their measurements [15, 37, 43, 136]. However, the relative contributions of treadmilling *versus* *de novo* nucleation to overall turnover has remained unclear due to the resolution limit of FRAP and the lack of stochastic elaboration of the previous models.

In recent years, several computational models have been developed to simulate complex cytoskeletal networks. In some works, turnover has been used as a tunable parameter to investigate properties of cytoskeletal systems including structural transformation of actin bundles [116], viscosity of crosslinked actin networks [23], tension generation and network morphology of actomyosin networks [137], and geometric contraction of actomyosin networks [77]. In particular, a recent work has shown that enhanced treadmilling fluidizes jammed actomyosin networks and there is an optimum threadmilling rate exists for maximal contractility [20]. However, the turnover dynamics itself has not been carefully investigated, while the turnover process has been commonly modeled in a highly simplistic manner.

Therefore, to gain deeper understanding into how older filament treadmilling and *de novo* filament formation modulate actin network turnover, we carried out mechanochemical simulations of actin network formation and growth, including the reactions between actin, Arp2/3 complex, formin and CP (Fig. 3.1). Our 3D structural model is based on microscopic physical chemistry of actin networks, relying on the MEDYAN force field and simulation package (Mechanochemical Dynamics of Active Networks), which combines a stochastic reaction-diffusion engine with polymer physics treatment of active matter [20]. We carried out MEDYAN simulations of various systems having a linear dimensions of 2 microns for 2,000 seconds each,

hence, reaching experimentally meaningful length- and timescales.

In this chapter, we focus on uncovering the relative contributions of treadmilling and other processes to actin network turnover. Our simulations suggest that it is convenient to categorize actin dynamics into two subgroups based on whether a particular actin filament existed or not at the beginning of turnover timescale measurement time window (which is further elaborated below). We denoted the former as "preexisting" filaments, which tend to be long and unfavorable for force generation, while filaments that come into existence after the observation start time are denoted as *de novo* filaments. Importantly, this framework mimics the conceptual idea of FRAP experiments that quantify turnover in actin networks. Our study addresses the following two questions about the regulation of actin turnover: (1) in what relative proportions do preexisting filaments' treadmilling and assembly of *de novo* filaments contribute to the global turnover? (2) How does CP affect turnover dynamics by regulating treadmilling and nucleation processes? Our MEDYAN simulation results show that preexisting filament treadmilling is the main contributor to the turnover under most circumstances. However, we found that reducing CP dissociation strongly enhances the *de novo* assembly contribution, in particular, because of increased cytosolic G-actin concentration. Furthermore, CP also promotes both uncapped filament elongation and nucleation, nevertheless, without affecting the overall turnover timescale. Although it is generally believed that rapid turnover is accompanied by rapid treadmilling, we found that fast turnover can also occur under slow treadmilling conditions when Arp2/3 concentration and filament capping are specifically fine-tuned.

3.2 Methods

All simulations performed in this work were carried out in MEDYAN [20]. The chemical reactions considered in our studies include filament polymerization and depolymerization at both barbed ends and pointed ends, CP binding and unbinding to filament barbed ends, Arp2/3 branching, and formin based linear nucleation. Each polymerization or binding reaction of CP consumes a diffusing molecule from a compartment and adds it to a barbed end or a pointed end that is located in the same compartment, and vice versa for depolymerization and unbinding reactions. The Arp2/3 binds to a mother filament and branches a one monomer long daughter filament with pointed end capped. The disassociation of Arp2/3 will release that molecule to the solution phase, creating a free pointed end. We also consider the destruction of a filament, which only happens if the filament shortens to become a dimer. The reaction models and parameters are greatly elaborated in Appendix B.1.1 - B1.4.

In this work, we initialized all networks starting with 100 seed filaments, each with two monomers, and varying $C_{G-actin}$, $C_{Arp2/3}$, C_{formin}, and C_{CP} in a non-periodic cubic box having a linear dimension of $2\mu m$. Dendritic and disordered networks were generated within a few seconds as the initial $C_{G-actin}$ was much greater than the critical concentration (Fig. B.9) [123, 138]. All networks were allowed to evolve for 2000 seconds. Statistical analysis of filament lengths indicated that all systems reached a steady state after several hundred seconds (Fig. B.3). The simulation data were sampled each second after a steady state was reached. The

presented results were each averaged over 5 independent trajectories. Further details on the measurements of turnover halftime and treadmilling rate can be found in Appendix B.1.5.

3.3 Results

3.3.1 Actin network turnover is mainly driven by treadmilling of pre-existing filaments.

We initialized Arp2/3 containing networks by adding Arp2/3, CPs and 100 seed filaments to a diffusing G-actin cytosolic pool, with the latter concentrations ranging from $3 - 25\mu M$. The initial concentration of G-actin is much higher than the critical concentration [123], thus filaments start rapidly polymerizing, converting almost all monomeric G-actin into polymeric F-actin upon reaching the steady state (Fig. B.9). To quantify turnover, we monitored the actin dynamics over the whole system and calculated turnover halftime ($t_{1/2}$, the time required for 50% of filaments to undergo turnover) after reaching the steady state via a process similar to the FRAP method. Further details about the simulation protocol and the parameters are provided in the Methods section and the Appendix B. The typical range of values for $t_{1/2} \sim 100s$ observed in our simulations (Fig. 3.2a) are similar to the timescales observed in some *in vitro* systems [15, 24].

We found that the actin filaments treadmill towards their barbed ends (Fig. 3.2b) while maintaining a stable average length (Fig. B.3). Compared to networks with a constant number of filaments, networks that allow nucleation and destruction

of filaments are more dynamic, with a broader filament length distribution. At earlier stages of network evolution, numerous new filaments are created by Arp2/3 nucleation in proportion to actin concentration, C_{actin}. Subsequently, after evolving for hundreds of seconds, the total number of filaments becomes nearly constant due to balancing of filament nucleation and destruction activities (Fig. 3.2c-d), which brings the network to a dynamic equilibrium.

It is difficult to directly disentangle the effects of filament treadmilling and nucleation since they are correlated: growth of *de novo* filament requires treadmilling. Instead, we calculated the fractional contributions to turnover of two subpopulations, namely, preexisting filaments and *de novo* filaments, where *de novo* filaments are defined as the filaments nucleated during each $t_{1/2}$ measurement. These results show that overall remodeling of the actin network is mostly driven by preexisting filament treadmilling regardless of actin concentration (Fig. 3.2e) and is nearly independent of the nucleator concentration (which is additionally discussed in section 2.3). To further examine the effect of nucleator, we passivated the Arp2/3 binding reaction after reaching a steady state, finding that inhibiting nucleation had minimal effect on turnover during the first $t_{1/2}$ measurement (Fig. B.4a). However, these older networks that lack nucleation were gradually arrested at longer time scales. Short filaments were rapidly destructed, leading to significant overall reduction in the total number of filaments (Fig. B.4b). At the very end, the remaining filaments were trapped at the simulation box boundaries, with the network becoming nearly static.

In summary, we conclude that although remodeling of homogeneous actin

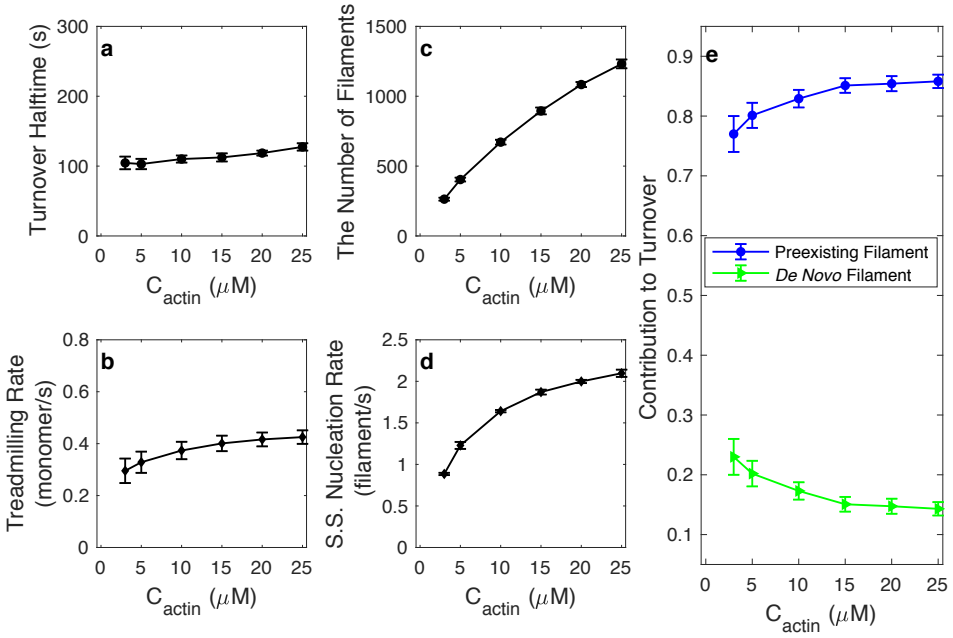

Figure 3.2: All plots are shown as a function of C_{actin}. (a) A plot of turnover halftimes ($t_{1/2}$) indicates that all systems have a similar $t_{1/2} \sim 100s$. (b) Treadmilling rate is defined as the speed of barbed end elongation, which matches the speed of pointed ends shortening at a steady state (SS). (c-d) Plots of the total number of filaments (c) and nucleation rate (d) at an SS are shown. The SS nucleation rate is balanced with the SS filament destruction rate. (e) The fractions of turnover contributed by treadmilling of preexisting filaments (blue squares) and *de novo* assembly of Arp2/3 nucleated filaments (green triangles) are plotted. All data were acquired at a steady state ($t > 800s$), where Arp2/3 and CP concentrations were fixed at $50nM$ for all conditions. Error bars represent the standard deviation from the mean in 5 simulation replicates.

networks is primarily governed by treadmilling of preexisting filaments rather than nucleation and growth of *de novo* filaments, however, the latter are essential for maintaining network dynamics at a steady state.

3.3.2 Slow CP dissociation promotes actin *de novo* assembly without altering global turnover.

CP binds to a filament's free barbed end, directly inhibiting polymerization. Interestingly, our results indicate that the turnover and treadmilling timescales of an actin network are very insensitive to CP's concentration until almost all barbed ends are capped (Fig. 3.3 and Fig. B.10). In the latter case, the uncapped barbed end elongation is significantly promoted as filament capping enhances the cytosolic G-actin pool, an effect denoted as "funneling" in prior works (Fig. B.5a-b) [123,139]. G-actin funneling also promotes nucleation during both an initial evolution stage and at a steady state (Fig. B.5c-d), which was also discussed earlier [3,35,60]. However, our simulations indicate that the resulting faster elongation and nucleation processes are insufficient to compensate for the extensive loss of free barbed ends after around 90% capping, giving rise to nearly static networks.

In the above presented simulations, the CP dissociation rate ($r_{CP,off}$) was chosen to be $0.04s^{-1}$, based on prior modeling works [49, 60], which is significantly slower compared with the estimates obtained from some *in vivo* studies [43, 140]. On the other hand, even slower CP dissociation rates on the order of $0.0004s^{-1}$ have also been reported primarily for *in vitro* systems [35, 141, 142], creating an overall dynamic range covering 3 orders of magnitude. Thus, we next explored to what degree CP dissociation rate affects actin network remodeling, varying $r_{CP,off}$ from $0.0004s^{-1}$ to $0.4s^{-1}$.

The corresponding results indicate that the turnover timescale is nearly inde-

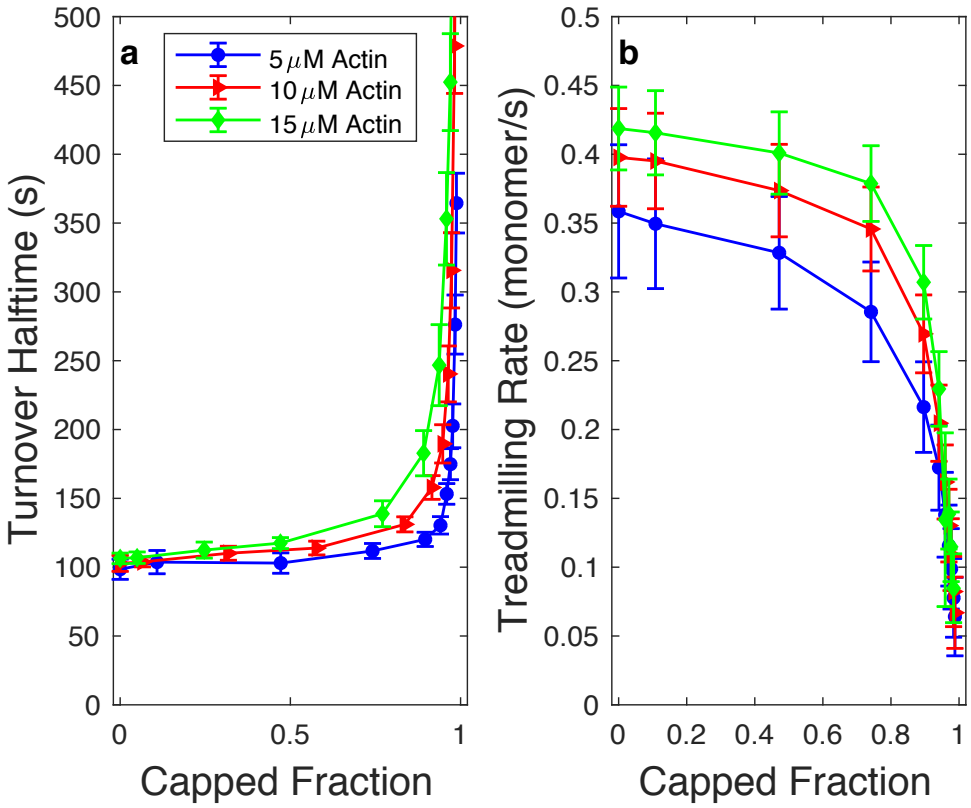

Figure 3.3: (a) Plots of the turnover halftimes and (b) treadmilling rates are shown as a function of the capped fraction of barbed ends. Significant slowdown of both turnover and treadmilling only occur at a very high capping fraction (more than 90%). The capped fraction as a function of C_{CP} is shown in Fig. B.6 Arp2/3 concentration is fixed at $50nM$ under all conditions. Error bars represent the standard deviation from the mean in 5 simulation replicates.

pendent of capping dissociation rate (Fig. 3.4a and Fig. B.11). However, *de novo* filament assembly is greatly enhanced when capped filament fraction increases due to low CP dissociation rates ($r_{CP,off}$ = $0.004s^{-1}$ and $0.0004s^{-1}$, as shown in Fig. 3.4b). In these systems, CPs tend to stay at capped filament ends at a timescale similar to or longer than the turnover timescale. Since treadmilling of preexisting filaments is highly inhibited when CP dissociation rates are low, this, in turn, promotes enhanced assembly of *de novo* filaments. Somewhat surprisingly, this promotion is

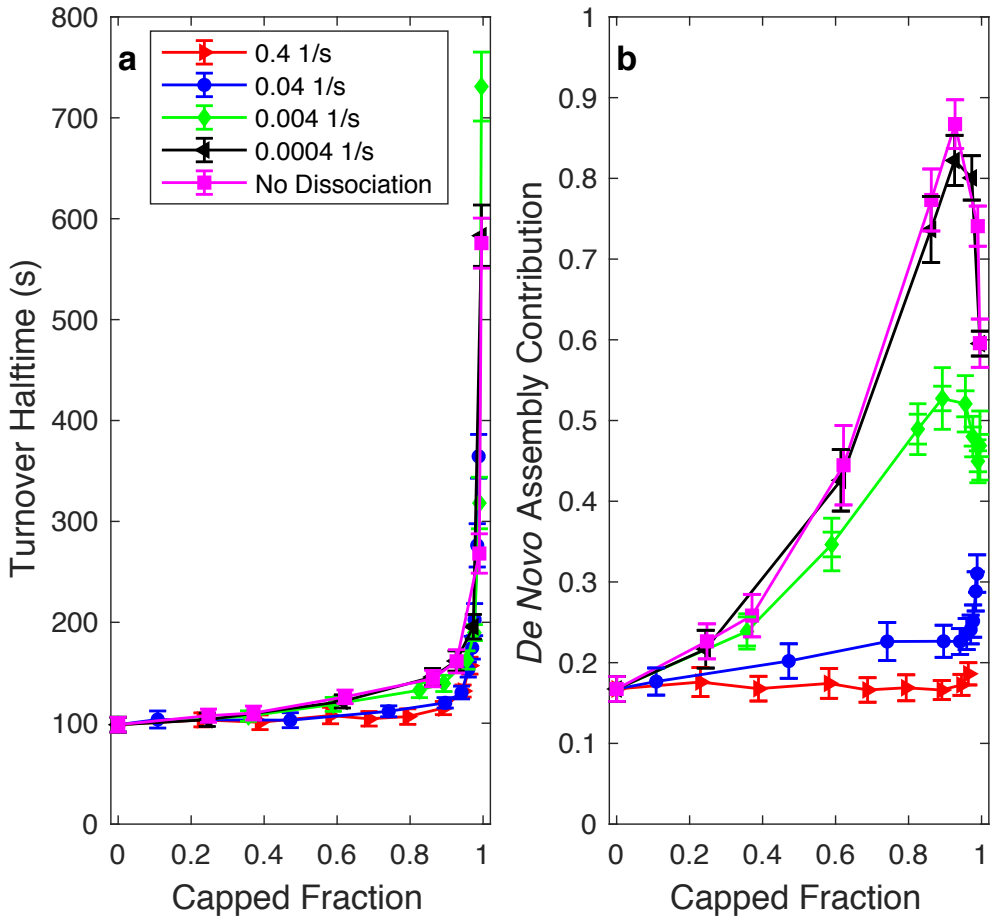

Figure 3.4: Plots of (a) $t_{1/2}$ and (b) the *de novo* filament assembly contribution to the turnover are shown as a function of the capped fraction of barbed ends. Varying the CP dissociation rate does not appreciably affect the turnover profile in (a). As seen in (b), preexisting filament treadmilling is the main contributor to turnover at high CP dissociation rates ($r_{CP,off}$ = $0.04s^{-1}$ and $0.4s^{-1}$), but reducing the CP dissociation rate promotes *de novo* filament assembly ($r_{CP,off}$ = $0.004s^{-1}$, $0.0004s^{-1}$ and no dissociation). Under the "no dissociation" condition, the CP would not dissociate from barbed ends unless a filament had been destroyed by pointed end depolymerization. The CP association rate was kept at $3.98(\mu M \cdot s)^{-1}$, with C_{actin} = $5\mu M$ and $C_{Arp2/3}v$ = $v50nM$. Error bars represent the standard deviation from the mean in 5 simulation replicates.

sharply peaked at ~ 90% fraction of capped filaments.

3.3.3 Arp2/3 and formin promote turnover via dissimilar treadmilling profiles.

Arp2/3 complex branches dendritic filaments with capped pointed ends, while formin nucleates linear filaments and attaches to filaments' barbed ends. Regardless of the distinct nucleation mechanism, both nucleators regulate the total number of filaments in a somewhat similar way, as can be seen in Fig. 3.5b and Fig. B.7d. At low nucleator concentrations ($< 0.05\mu M$), treadmilling is slow (Fig. 3.5a and Fig. B.7b) because more filaments are capped by CPs (Fig. B.8d and Fig. B.7e). In this case, turnover is rather sensitive to the nucleator concentration (Fig. 3.5d, left and Fig. B.7a).

Turnover becomes faster and less sensitive to nucleators as their concentrations further increase (Fig. 3.5d, right and Fig. B.12), however, distinct treadmilling profiles emerge for Arp2/3 *versus* formin. In Arp2/3 based networks, treadmilling rate is a biphasic function with a sharp maximum at $C_{Arp2/3} \sim 0.03\mu M$ (Fig. 3.5a). As a result, turnover halftime at high $C_{Arp2/3}$ is does not decrease below $t_{1/2} \sim 60s$. Unlike Arp2/3, treadmilling does not slow down at high concentrations of formin, such that very fast turnover rates can be achieved ($t_{1/2} \sim 10s$, Fig. B.7a).

The contrasting treadmilling profiles of Arp2/3 and formin at high concentrations can be attributed to three different causes. Firstly, barbed end elongation is strictly balanced with pointed end shortening at a steady state. Similar to CP, Arp2/3 caps the pointed end, also hindering the overall treadmilling process. Secondly, binding affinity between the Arp2/3 complex and the mother filament is

strong [130]. Hence, we assume that filament depolymerization cannot pass through the branch point. Thirdly, nucleation and treadmilling compete with each other for G-actin. Therefore, the more nucleators a system contains, the less G-actin is available for polymerization. Consequently, treadmilling is inhibited in highly dendritic networks. In contrast, although the reduction of G-actin as C_{formin} concentration increases also occurs in linear formin networks, this still leads to relatively rapid treadmilling rates, which albeit level off (see Fig. B.7c).

Surprisingly, Arp2/3 concentration has minimal impact on the contribution of *de novo* filaments to actin turnover (Fig. B.8a). We suggest the following explanation for this apparent lack of sensitivity. Preexisting filaments and *de novo* filaments polymerize at similar speeds, thus their relative contributions to the turnover are mainly dependent on the ratio of filament numbers in the two subpopulations. Since adding more Arp2/3 simultaneously increases the number of preexisting filaments and *de novo* filaments to the same extent, their fractional contributions would not change as a function of $C_{Arp2/3}$. Another reason for the weak dependence of *de novo* filaments' contribution to treadmilling is based on *de novo* filaments being usually shorter than preexisting filaments, making them more prone to complete disassembly.

3.4 Discussion and Conclusions

In this work, we studied turnover dynamics of actin networks using a microscopic, structure based mechanochemical 3D model, called MEDYAN, which simul-

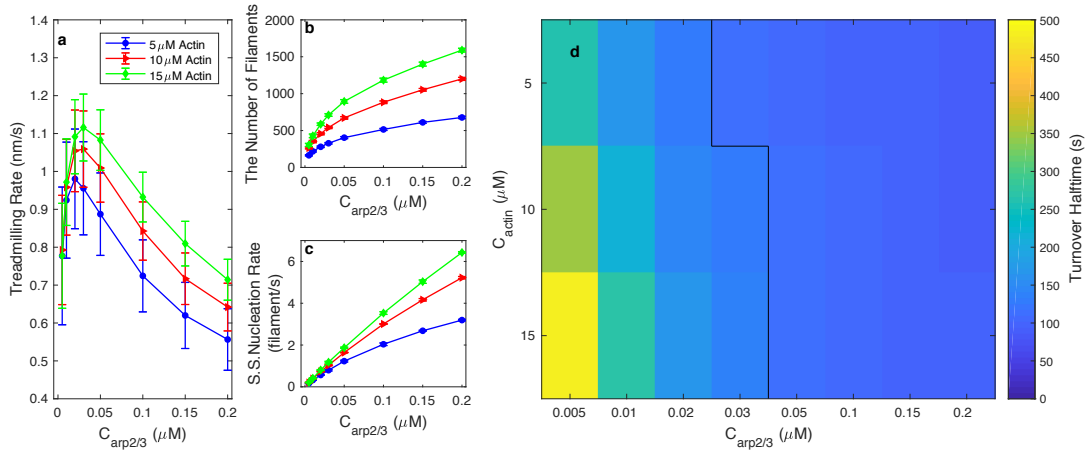

Figure 3.5: Various physical and geometrical observables are plotted as a function of the Arp2/3 concentration, $C_{Arp2/3}$: a) the filament treadmilling rate, (b) the total number of filaments, (c) the steady state filament nucleation rate and (d) the color map of $t_{1/2}$. (a) The treadmilling speed profiles reach a maximum at $C_{Arp2/3}$ = $20nM$ for C_{actin} = $5\mu M$ and $C_{Arp2/3}$ = $30nM$ for C_{actin} = $10\mu M$ and $15\mu M$. (b-c) Increase of the total number of filaments and of the SS nucleation rate confirm that $C_{Arp2/3}$ directly promotes filament nucleation. (d) The turnover halftime decreases with increasing the Arp2/3 concentration. Left of the solid line: the turnover timescale is sensitively promoted by $C_{Arp2/3}$; right of the solid line: the turnover timescale is insensitive to $C_{Arp2/3}$. The CP concentration was fixed at $50nM$ under all conditions. Error bars represent the standard deviation from the mean in 5 simulation replicates.

taneously treats stochastic chemistry, molecular diffusion and filament mechanics. Our results suggest that a useful general framework for gaining deeper insights into the organization of turnover processes is to analyze two distinct filamentous actin subpopulations. More specifically, we quantified contributions of preexisting filament treadmilling and *de novo* filament assembly to turnover. We define turnover as global remodeling process of the actin network, which can be probed via experimental approaches, such as FRAP. We found that actin remodeling is mainly determined by preexisting filament treadmilling. However, at low CP dissociation rates, the contribution of *de novo* filament nucleation and assembly becomes significant. Since longer filaments in less branched networks are unfavorable for force

generation [35, 84, 143], slow CP dissociation conditions are expected to produce a more mechanically active actin network.

Although it may be implicitly assumed that individual filament treadmilling is equivalent to network turnover, we found clear instances where this is not so. For example, our simulations have revealed that in highly dendritic networks rapid turnover is accompanied by slow filament treadmilling. In this case, reduction of the treadmilling rate is compensated by growth of the total number of filaments, at conditions where either nucleator or CP concentrations are enhanced.

Conceptually, treadmilling describes the microscopic dynamics of an individual filament and may result in a force generation. On the other hand, turnover is more commonly described as an experimentally measurable property via FRAP that captures global remodeling of actin networks. The separate analyses of local filament treadmilling and global network turnover in this work help to better understand the relationship between these interrelated phenomena, shedding light on the overall organization of actin network self-assembly dynamics.

Two theories have been developed to describe how CP regulates remodeling of dendritic networks. Actin funneling hypothesis, proposed by [123] suggests that barbed end capping would enhance the cytosolic G-actin concentration, which, in turn, would lead to faster elongation of uncapped filaments. Detailed microscopic simulations have both supported and elaborated on this idea [60]. Other workers introduced another hypothesis, called "monomer gating", as a further elaboration of the actin funneling effect. This theory suggests that increased cytosolic G-actin concentration tends to promote Arp2/3 branching rather than elongation of free

barbed ends, hence, leading to more dendritic networks [35, 144]. Interestingly, our findings indicate that systems containing CPs having high dissociation rates follow the actin funneling hypothesis regardless of the Arp2/3 concentration. On the other hand, the "monomer gating" mechanism becomes more operative in our simulations when CP dissociation rates are slow enough, providing G-actin molecules more opportunities to engage in the nucleation reaction and thus promoting *de novo* filament assembly.

We investigated the effects of two types nucleators in this work: branching by Arp2/3 and linear nucleation by formin. Arp2/3 requires activation by WAVE or WASP families of proteins [9, 130], however, for the sake of simplicity, we ignored activation of Arp2/3 itself. Our conclusion of treadmilling inhibition at high Arp2/3 concentrations is partially based on the assumption that Arp2/3 complex blocks the depolymerization of mother filaments. Although this assumption is supported by the observation of strong binding affinity between Arp2/3 and actin filaments [130, 142], it has not been directly proven.

The turnover timescales observed in our simulations fall within the range measured for *in vitro* actin networks [15, 24], however, *in vivo* experiments reported much faster dynamics [37, 43, 145, 146]. It is presumed that the discrepancy between the *in vitro* and *in vivo* rates is due to the lack of profilin-actin in formin based networks [8, 140], and also lack of ADF/cofilin [15, 147] in many *in vitro* experiments (and our current simulations). Motor proteins, such as myosin II, can also affect the turnover dynamics [134], which should be explored in future work.

We also would like to point out that G-actin concentrations reported *in vivo*

can be up to 3 orders of magnitude higher than the typical critical G-actin concentration created by filament treadmilling *in vitro* (a detailed compilation of the experimentally measured actin concentrations in various cell types can be found in [148]). However, maintaining such high G-actin concentrations at a steady state would lead to extremely fast elongation rates that do not appear to be physiological reasonable. Consequently, it is believed that only a small fraction of overall cytosolic G-actin is activated *in vivo* at any instant [131, 149]. Including explicit modeling of G-actin activation, as more relevant experimental data become available, would present another interesting avenue for future research.

Chapter 4: The formation of cortex-like and ring-like actomyosin structures

This chapter is adapted from: Qin Ni, Kaustubh Wagh, Arpita Upadhyaya and Garegin A Papoian. "Filament treadmilling induces phase transition in actomyosin networks." In preparation. (2020)

Author contributions: Q.N. and G.A.P. performed the computer simulations (Section 4.2.1 to 4.2.3, part of Section 4.2.4, and Figure 4.1, 4.3, and 4.4). K.W. and A.P. performed the experiments (part of Section 4.2.4, and Figure 4.2). All authors wrote the manuscript.

4.1 Introduction

A shell-like cortex is ubiquitously found under the cell membrane of eukaryotic cells, which is primarily comprised of actin and myosin. It is characterized by a mesh geometry, playing an indispensable role in defining cellular shape and cell's mechanochemical responses [28, 42]. The actin filaments within the cortex are highly dynamic, undergoing rapid polymerization and depolymerization, subject to contractile forces from myosin motors [114, 150]. Polymerization is highly polarized: monomeric actin (G-actin) binds to the barbed ends of a filament and

polymeric actin (F-actin) dissociates from the pointed end in a process called treadmilling [3, 130]. As a consequence, the actin cortex is a dynamically polymorphic structure that is capable of rapidly remodeling in response to biochemical signals and physical stimuli [24, 151]. Improper assembly of the actin cortex hampers cellular functions [152, 153]. A similar structure can be found in immune cells, such as T cells, the latter reorganizing their actin network upon stimulation by an antigen-presenting cell into a quasi 2D actin ring that sequesters different signaling complexes in separate concentric domains [46, 73, 74, 154]. While the actin cortex and actin ring are indispensable for the normal functioning of all organisms, the fundamental physical mechanisms underlying the formation of these structures are still not well understood.

In remarkable contrast to the shell-like or ring-like networks ubiquitously seen in living cells, *in vitro* experiments primarily produce actomyosin networks comprised of clusters that originate from global geometric collapse due to myosin's contractile activity [20–22, 24, 25, 137]. We hypothesized that this apparent disparity between the prevailing actomyosin architectures formed in *in vitro versus* those *in vivo* may arise from the notable difference in the corresponding treadmilling rates: *in vitro* networks reconstituted from purified proteins exhibit treadmilling rates that are often much slower than those observed *in vivo*. Therefore, to probe this idea, one would like to systematically explore how the treadmilling rate affects the actomyosin network architecture. This is a difficult experimental task, requiring careful control of molecular machinery and actin polymerization kinetics. On the other hand, such limitations can be overcome by computer simulations, which provide a powerful way

to capture the complex chemistry and mechanics of the active cytoskeleton, bringing also significant mechanistic insights.

In order to find a minimal set of conditions that lead to the formation of rings and cortices, we used the MEDYAN (Mechanochemical Dynamics of Active Networks) simulation framework. MEDYAN couples sophisticated treatment of complex cytoskeletal reactions, polymer mechanics, and mechanochemical feedbacks to simulate complex actomyosin networks at experimentally meaningful length and time-scales at a single molecule resolution [20]. It's chemical engine models a large variety of cytoskeletal reactions, such as treadmilling, nucleation by formin, and non-muscle myosin II (NMII) binding and walking, via a stochastic reaction-diffusion scheme. The mechanical engine employs a coarse-grained representation of semi-flexible actin filaments as connected cylinders, treating filament bending and stretching deformations and steric interactions, as well as NMII and linker crosslinking potentials. MEDYAN also captures various mechanochemical feedbacks of actomyosin networks, for example, relying on the Brownian ratchet model [89]. Using MEDYAN simulations, we discovered that increasing the speed of filament treadmilling induces a phase transition from large clusters to actin rings and cortices. Furthermore, our corresponding quantitative measurements on live Jurkat T cells provide experimental support for the idea that the tug of war between filament treadmilling and myosin induced contraction determines whether a ring near the boundary will form, or, instead centripetally moving clusters will be more prevalent.

4.2 Results

4.2.1 Filament treadmilling generates disordered actin networks

We initialized *de novo* networks in MEDYAN with some seed filaments, 40 µM diffusing G-actin, and 100 nM filament nucleators. To reduce the computational cost, most of the simulations were carried out in a quasi-2D cylindrical geometry with a diameter similar to that human cells (3.8 to 10 µm in diameter and 200 nm in height). Filament treadmilling is a complex dynamic process consisting of polymerization and depolymerization at both ends, and thus, direct manipulation of the filament treadmilling rate (r_{TM}) is not physiologically reasonable. For simplicity, we tune the barbed end polymerization rate constant and pointed end depolymerization rate constants to mimic the effects of treadmilling promoters such as formin, profilin and cofilin [8, 15, 147], and measure the actual speed of treadmilling. We define r_{TM} as the average barbed end elongation rate, which is also equal to the shortening rate of the pointed end at steady state (see Supplementary Information, SI, for details).

We first modeled networks in the absence of NMIIs and linkers at different average treadmilling rates ($\langle r_{TM} \rangle$ = 0.57 s^{-1}, 1.41 s^{-1}, and 2.21 s^{-1}) and found that disordered actin networks were created at all treadmilling conditions tested. We quantified the spatiotemporal evolution of the network geometry by plotting the median of the radial filament density distribution, R_{median}, as a function of time. In NMII-free networks, we observed a relatively uniform filament density across

the network regardless of treadmilling rates (Fig. C.1d-f, and Fig. C.3). In this case, the network geometry is dominated by stochastic, non-preferential filament treadmilling. The boundary effect, based on the Brownian Ratchet model, also plays a role as the boundary repulsion force inhibits the barbed end polymerization such that filaments reaching the boundary rapidly depolymerize and eventually get destroyed. The loss of filaments through depolymerization is compensated by the nucleation of new filaments, resulting in dynamic but stable disordered structures.

4.2.2 Actin rings and cortices formation upon enhancing filament treadmilling rates

Next we initialized the same actin network as described above for 300 s and then added NMIIs to explore how they affects actin network geometry. We find that the addition of NMIIs and alpha-actinin into slow-treadmilling networks (r_{TM} = $0.56s^{-1}$) induces geometric collapse of filaments into actin clusters (Fig. 4.1b-iii). This geometric pattern is consistent with prior *in vitro* and *in silico* works on contractile actomyosin networks [21, 22, 24, 25], where contractility can be defined as a symmetry breaking event accompanied by a geometric collapse of the network. Although the size and location of actin clusters vary significantly between duplicated trajectories (Fig. C.1c), the decreasing R_{median} suggests that the overall collapse is centripetal (Fig. 4.1a-iii).

It is reasonable to assume that treadmilling and geometric collapse are two competing events since treadmilling tends to homogeneously distribute filaments in

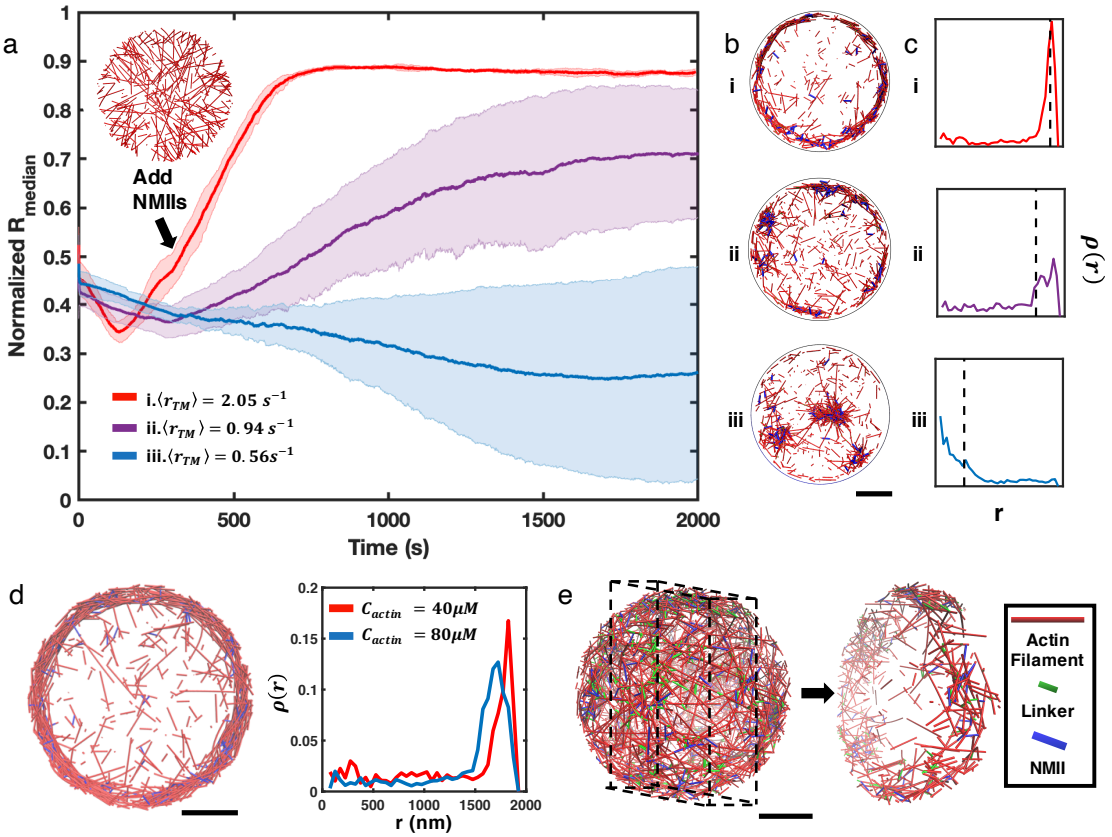

Figure 4.1: (a) Normalized median of filament radial density distribution (R_{median}) at different treadmilling speeds. The treadmilling rate ($\langle r_{TM} \rangle$) is defined as the average number of actin monomers added per filament per second at the barbed ends - equivalent to the rate of F-actin depletion from the pointed ends - after reaching the kinetic steady state (SI-2). 0.06 µM of NMII and 4 µM of alpha-actinin were added at 301 s. The inset figure is a snapshot at t = 300 s of networks with $\langle r_{TM} \rangle$ = 2.05s^{-1}. 5 runs per condition. The shaded color and error bars represents the standard deviation across trajectories. (b-c) The representative snapshots at each treadmilling condition (b) and their filament radial density distribution, $\rho(r)$ (c). Dash lines in (c) indicate the position of R_{median}. (d) The representative snapshot of ring-like networks with 80 μM actin (left), and $\rho(r)$ of actin rings with 40 μM actin and 80 μM actin. $\langle r_{TM} \rangle$ = 1.35 s^{-1}. (e) A snapshot of 3D cortex-like networks (left) and a slice showing the internal structure (right). (a,b,d,e) Actin filaments are red cylinders, NMIIs are blue cylinders and linkers are green cylinders in all snapshots. All scale bars are 1 µm.

the network, while NMII tends to trap filaments into clusters. We thus explored the changes in the actin network geometry by increasing the treadmilling rate while maintaining the presence of NMIIs as a constant variable. Although filament nucleation occurs stochastically throughout the entire network and there is no arbitrary filament tethering near the boundary, filaments steadily accumulate at the network edge after the addition of NMII to rapid-treadmilling networks (Fig. 4.1a-i). During this process, we observed that many filaments were deformed by NMII, gradually changing their orientation from perpendicular to the boundary to parallel (Video 5). After allowing the system to evolve for several hundred seconds, actin networks transform into ring-like structures (Fig. 4.1b-i).

The thickness of the actin ring is approximately a few hundred nanometers, and the thickness of actin ring increases as actin concentration increases (Fig. 4.1c). Most filaments in actin rings are oriented parallel to the boundary (Fig. C.5), and filaments or small actin clusters undergo an azimuthal flow at the boundary (Video 6). The same 2D ring-like patterns are observed on a much larger length scale (Fig. C.6), and hollow spherical cortex-like patterns emerge if we extend the model to three dimensions (Fig. 4.1d).

The formation of ring-like actin networks is strongly correlated with the treadmilling rate. By plotting the distribution of R_{median} at different $\langle r_{TM} \rangle$, we are able to define two geometric states. To form ring-like geometry, $\langle r_{TM} \rangle$ has to be above a certain threshold, which is between 0.65 and 0.94 s^{-1} in our simulations (Fig. 4.3a-b, and Fig. C.4a). In the ring state, R_{median} is higher and has less dispersion. Networks tend to geometrically collapse with $\langle r_{TM} \rangle$ below this threshold, with lower

R_{median} but higher dispersion. Networks with $\langle r_{TM} \rangle$ close to this threshold rate can sometimes form a mixture of clusters and rings (Fig. 4.1b-ii). We also notice that networks with higher treadmilling rate require shorter time to transform into ring-like structures after the addition of NMII.

Interestingly, this change of R_{median} from cluster state to ring state displays a sharp increase (Fig. 4.2b). We then examined the system energy as a function of $\langle r_{TM} \rangle$. While the chemical free energy reminds almost the same across different $\langle r_{TM} \rangle$ (Fig. C.7), the mechanical energy (U_{Mech}) of the system decreases as R_{median} increases (Fig. 4.2c-d). Moreover, this negative correlation is valid either within the same structural regimes (ring *vursus* cluster) or across different structural regimes, suggesting that the periphery is more energy favorable than the central region. The distributions of U_{Mech} also display a sharp decrease when $\langle r_{TM} \rangle$ reaches the transitional rate, where U_{Mech} of actin rings is 2-3 fold lower than that of clusters (Fig. 4.2, d). These sharp change in order parameter potentially suggests that the structural change between ring and cluster is a phase transition.

4.2.3 Disrupting treadmilling induces centripetal collapse of actin rings *in vivo* and *in silico*

In order to further understand how treadmilling regulates ring-like actin networks, we examined at F-actin in Jurkat T cells, which are known to form ring-like actomyosin structures that are highly similar to our simulations upon activation by stimulatory antibodies [46,73,74,154]. Direct controls of treadmilling rates in exper-

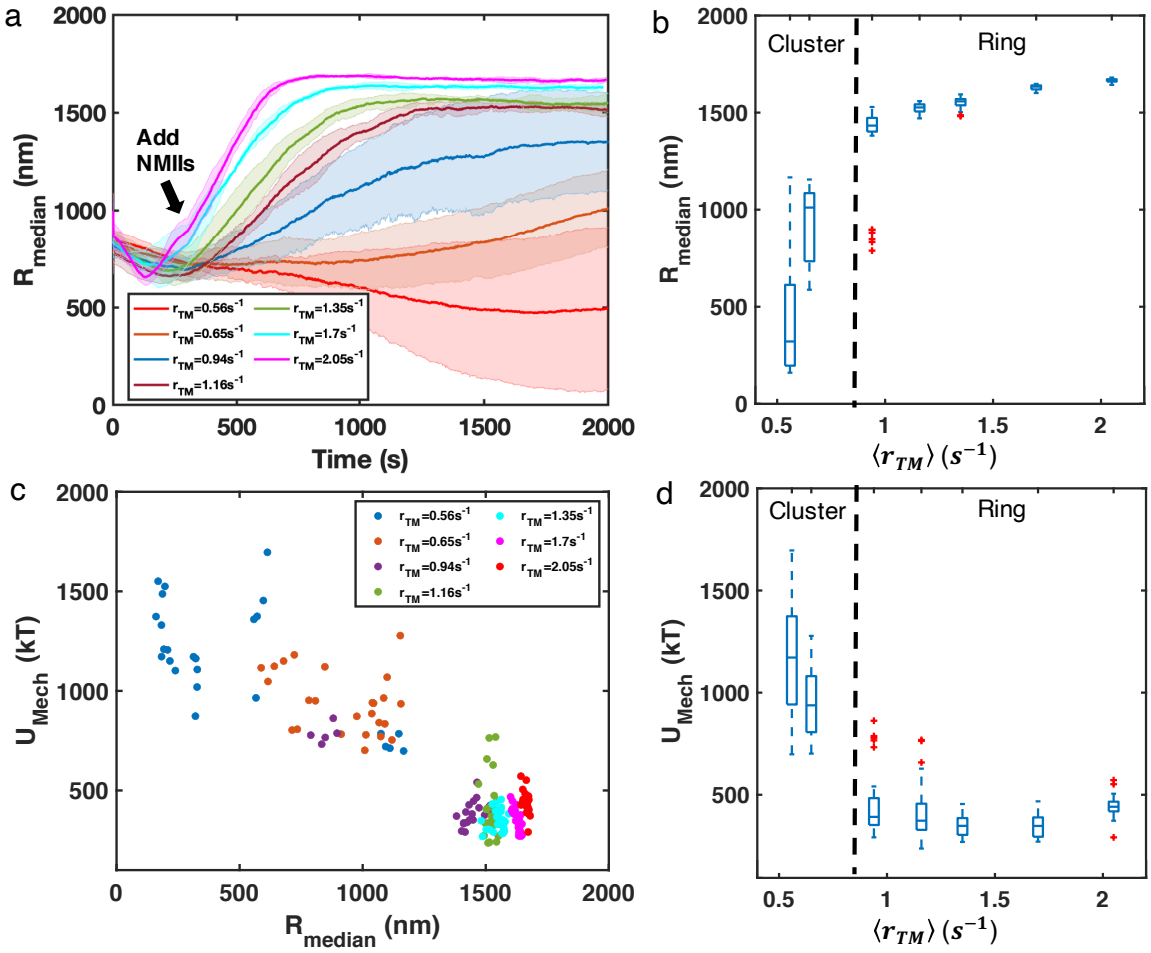

Figure 4.2: (a) Median of filament radial density distribution (R_{median}) at different treadmilling speeds ranges from 0.56 s^{-1} to 2.05 s^{-1}. The shaded color and error bars represents the standard deviation across trajectories. (b) The box plot of R_{median} of the last 500 seconds simulation at each treadmilling rate. (c) System mechanical energy (U_{Mech}) of the last 500 seconds simulation and their corresponding R_{median} at each treadmilling rate. U_{Mech} includes the bending energy of actin filaments and the stretching energy of filaments, motors, and linkers. (d) The box plot of U_{Mech} at each treadmilling rate. (b-d) Data are taken every 100 s during t=1500 - 2000s, 5 runs per condition. (b,d) The top and bottom edges of the box indicate the 25th and 75th percentiles, the central mark indicates the median, the dash line represents the extreme data points, and the "+" symbol represents the outliers.

iments is not feasible, hence we use Latrunculin A (LatA) as a reasonable substitute to illustrate the same general concepts. LatA is known as a toxin that decreases the polymerization rate and increases the depolymerization rate by sequestering G-actin and accelerating phosphate release from ADP-Pi-actin [1, 155, 156]. We used EGFP-f-tractin, an indirect reporter of F-actin to visualize the actin network as imaged under total internal reflection fluorescence microscopy (TIRF). In order to compare with simulations, we used the fluorescence intensity as a reporter of F-actin distribution and a normalized R_{median} to quantify the evolution of the network under LatA inhibition. With weak treadmilling inhibition (C_{LatA} =250 nM), the ring-like structure is preserved (Fig. 4.3b) as observed in comparison with the vehicle control (Fig. 4.3a). This shows that with a low inhibition of treadmilling, filament treadmilling still overweighs myosin driven contraction, dominating the network geometry. With high doses of LatA, R_{median} rapidly decreases, indicating a collapse of the network towards the geometric center of the cell (Fig. 4.3c-d). The rate of centripetal collapse of the actin network increases with increase in C_{LatA} (Fig. 4.3e-f). The dismantling of the actin ring is also accompanied by the formation of F-actin clusters or bundles (Fig. 4.3f-g).

To compare with *in vivo* experiments, we perturbed $\langle r_{TM} \rangle$ *in silico* to model the effect of LatA after ring-like networks are established. For simplicity, we reduced the polymerization rate constants and increased the depolymerization rate constants, and we discovered specific parameter ranges that closely follow the T cell experiments (see SI-5 for more details). We found that actin rings persist at weak treadmilling inhibition (Fig. 4.4b), while they collapse into clusters under

strong inhibition (Fig. 4.4c). Measurements of R_{median} and the rate of collapsing (Fig. 4.4d-e) at different inhibition conditions indicates the centripetal collapse of the ring network, as observed *in vivo* .

4.3 3. Discussion

Detailed mechanochemical modeling of filament treadmilling in MEDYAN shows a striking morphological transitions in actomyosin networks. We have found that two distinct types of dynamic patterns emerged under the interplay between treadmilling rates and NMII contractility in an initially disordered network: (1) actin clusters in slow-treadmilling networks and (2) actin rings (in 2D) or cortices (in 3D) in fast-treadmilling networks. Importantly, the formation of these structures are extremely robust as filament tethering to the boundary or preferential filament nucleation at the network periphery are not required.

Our energy analysis suggests that comparing to the cluster structure, the actin ring structure is an energy ground state. The addition of myosin motors and crosslinkers to an initially disordered actin network induces contractility, creating an energy trap that attracts actin filaments into clusters (Fig. 4.4g). Rapid filament treadmilling allows the system to overcome these contractility trap, where small clusters rapidly dissolve and exchange with their environment. In this case, the network tends to choose a structure that can reduce its energy. Since the energy is lower when networks are closed to the periphery (Fig. 4.2c), actin filaments eventually accumulate at the network periphery that forms actin rings or cortices

(Fig. 4.4f, higher). On the other hand, networks with slower filament treadmilling are trapped at the higher energy state. These systems are dominated by myosin-driven contractility, leading to a non-ergodic state with actin filaments centripetally collapse of the network (Fig. 4.4f, lower).

Although some earlier computational studies have emphasized how network morphology is regulated by treadmilling rate [23, 137], the active formation of cortical shell-like or ring-like networks has never been observed. In fact, these geometries have been widely found in other sub-cellular structures such as podosomes and actin/septin rings in dendritic spines. Unable to observe these general structures may due to lack of detailed chemical models of filament treadmilling and nucleation. In addition, we believe a non-periodic boundary condition is also required for actin cortex or ring formation. We observe similar phase-transition-like behavior by tuning filament treadmilling rates (Fig. 4.2b and d). Phase transition in many biomolecular systems is often driven by passive biomolecular interaction such as valency effect or binding affinity [157, 158], but in this work we suggest a phase transition can also be induced by non-equilibrium actomyosin dynamics.

In this work, we have shown that rapid treadmilling and the presence of myosin are sufficient to create ring-like or cortex-like actomyosin networks in a minimal system with confined boundary. However, it is reasonable to believe that filament tethering to the membrane and preferential nucleation at the boundary can assist the formation of ring and cortex. On the other hand, Arp2/3 as nucleators potentially play important roles in regulating the mechanical properties of actin rings or cortices. In spreading T cells, the outer region of actin ring is Arp2/3 enriched,

creating a dense dendritic network that can potentially exclude myosin, while the inner region has mostly formin-nucleated filaments. How different nucleator types affect actin architectures and ring/cortex formation should be explored in future work. Moreover, we added a constant concentration of alpha-actinin crosslinker in accompany with myosin in the simulation. The concentration of crosslinkers and crosslinker types can potentially affect the actin ring/cortex formation by affecting contractility: higher contractility should be unfavorable for actin ring/cortex formation. Studying the building blocks of these structures can allow us to probe possible ways to reverse defective organization of cortices, which can help devise novel therapeutic approaches to primary immunodeficiencies, autoimmune disorders, and cancer.

4.4 Methods

4.4.1 Simulation setup

In this work, we employed the open-access mechanochemical simulation tool of active matters (MEDYAN [20]) to investigate the spatialtemporal evolution of actin networks under different treadmilling and myosin motor conditions. We initialized *de novo* networks with 40 µM diffusing G-actin, 100 nM formin and 100 seed filaments based on their cytoplasmic concentrations measured *in vivo* [159]. The network is cylindrical with the effective height of 200 nm, and the effective radius of 1900 nm. The spherical network has a radius of 2000 nm. With such a high initial G-actin concentration, disordered networks are generated within a few seconds by filament

nucleation and elongation. Although treadmilling can be promoted by formin, which binds to the filament barbed end and facilitates filament elongation [8], in this work we use a uniform polymerization rate as an input in each condition. More model details can be found in Appendix C.1, and parameters for chemical reactions can be found on Table C.2.

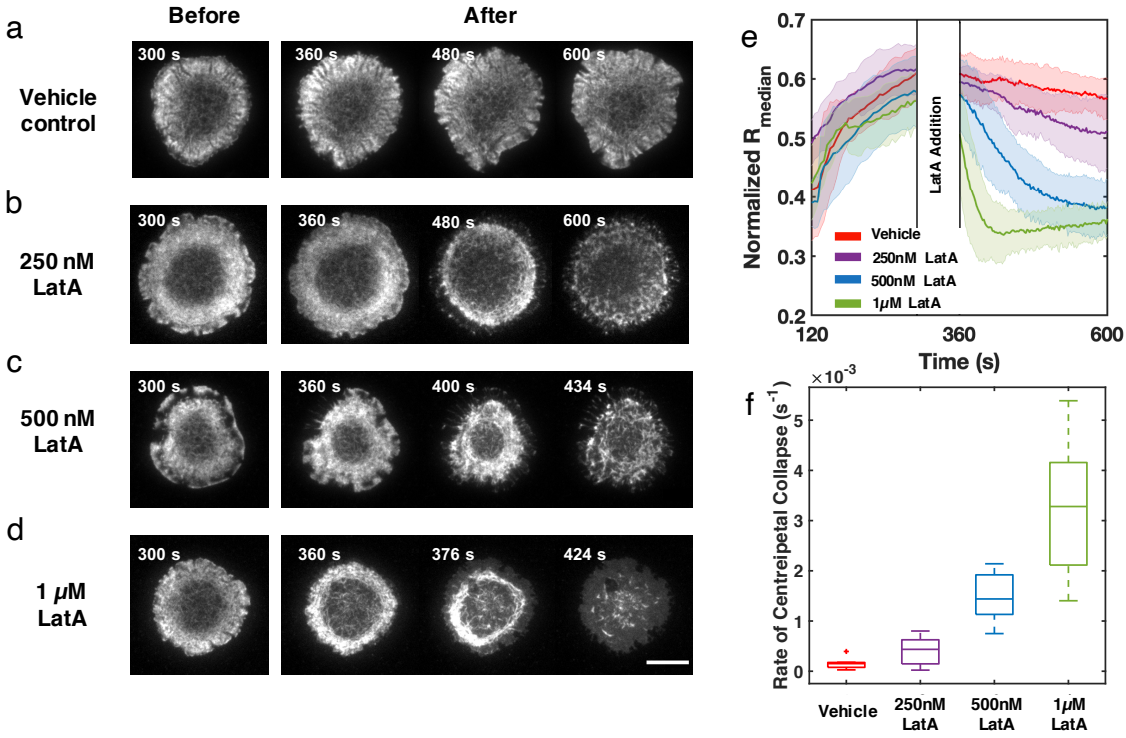

Figure 4.3: Timelapse montage of Jurkat T cells expressing Ftractin-EGFP spreading on anti-CD3 coated glass substrates. Addition of (a) vehicle (0.1% DMSO), (b) 250 nM LatA, (c) 500 nM LatA, or (d) 1µM LatA was done between 300 and 360 seconds after seeding the cells. The timelapse illustrates the centripetal collapse of the actin ring upon treatment with the actin inhibitor Latrunculin A. The timescales of this collapse depend on the concentration of LatA as can be seen from the timestamps on the images. Scale bar: 10 µm. (e) Quantification of the spatial organization of the actin network using the normalized median of filament radial density distribution. (f) Rate of centripetal collapse, measured as the slope of the normalized median distribution after inhibition. 7-11 cells per condition. The shaded color and error bars represents the standard deviation across trajectories.

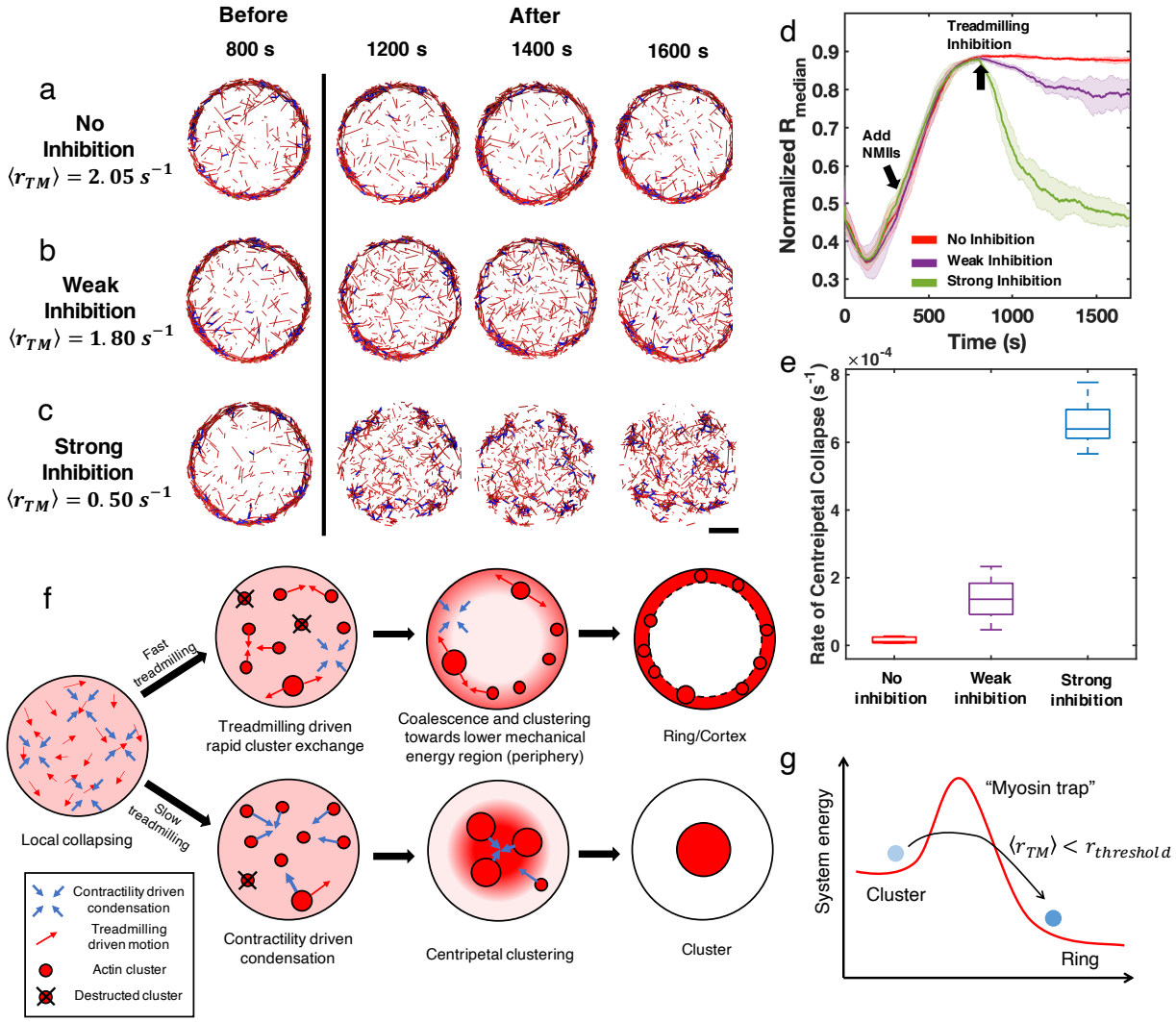

Figure 4.4: Timelapse montage of actin ring simulation with filament inhibition at 800s. The $\langle r_{TM} \rangle$ corresponding to no inhibition (a), weak inhibition (b), and strong inhibition (c) are $2.05S^{-1}$, $1.80S^{-1}$, and $0.50S^{-1}$ respectively. Before inhibition, all simulations have the same kinetic conditions (also shown as case i in Figure 4.1a). The treadmilling inhibition mimics the effect of LatA based on recent *in vitro* experiments [1]. See SI-5 for more details regarding treadmilling inhibition. The treadmilling rates after inhibition (averaged from 1500s to the end of simulations) are shown in the figure legend. Scale bar is 1 µm. (d)The median of radial filament density distribution at different treadmilling inhibition condition. (e) The centripetal collapse rate after inhibition. (d-e) The shaded color and error bars represents the standard deviation across trajectories, 5 runs per condition. (f) A sketch showing actin ring/cortex versus clusters formation. At low treadmilling rates, networks are dominated by myosin-driven contraction, leading to centripetal collapse into clusters (lower). Faster filament treadmilling allows networks to overcome the myosin trap, where filaments tend to move to periphery due to lower energy (upper). (g) A graphical description of system energy landscape with the myosin trap.

Chapter 5: Discussion and Outlook

In this thesis, we explore the self-organization dynamics underlying the assembly of three *in vivo* actin architectures: stress fibers, dendritic lamellipodia, as well as actin cortices and rings. We utilize the computer simulation platform MEDYAN to reconstitute actin networks with key cytoskeletal proteins. Collaborating with experimentalists and theorists, our work reveals how actin networks remodel themselves in response to mechanical and chemical stimuli from inside and outside the cell. Importantly, our studies provide biophysical insights for the formation of highly ordered actin scaffolds from initially disordered networks, which helps to understand how cells adjust their actin structures under different mechanochemical environments to fulfill their unique responsibilities in cell biomechanics and motility.

In the first project (Chapter 2), we show that bundle-like actin configuration can be induced by tensile external forces, and this work can be further extended to investigate the effect of different force types generated by *in vivo* environments. For example, cells in blood vessels are mechanically impacted by blood pressure, which generates periodic axial and circumferential wall stresses on entire cells [57]. Understanding how actin network response and transfer forces in this system can help to cure cardiovascular diseases [160, 161]. On the other hand, it is not known

how stress fibers develop graded polarity, an essential property for contractility generation. Intuitively, the periodic polarity pattern is a natural consequence of myosin driven polarity sorting [20, 162, 163], but we fail to observe the development of graded polarity in our simulation. It may require us to anchor both ends of the stress fiber and allow a longer time for the polarity sorting.

The system shown in Chapter 4 can be extended to investigate the non-equilibrium physical principles during actin self-organization by tracking free energy dissipation. Recently developed theories suggest that active matter systems, such as actomyosin networks, optimize the speed of free energy dissipation as they self-organize from disordered states to highly-ordered scaffolds [85, 164]. This theory has been supported by experimental work, which suggests that the entropy production rate of actomyosin networks *in vitro* is maximized at steady state [165], in striking contrast to the minimal entropy production principle of irreversible systems. Whether it is a universal rule in the active matter, and what regulates the free energy dissipation during self-organization are still elusive. Moreover, a series of works carried out by various groups have observed that actomyosin networks sometimes undergo large-scale, non-Gaussian release of free energy or actin displacement in cells [166–168] and in computer simulations [169, 170]. What leads to the non-Gaussian actin dynamics and how it contributes to actin remodeling are still unknown. The quasi-2D system presented in Chapter 4 is an excellent model to investigate this question, since we are able to tune actin network remodeling without altering the main force generators - myosin motors and crosslinkers. Recently, we found that actomyosin networks sometimes enter a highly unstable state that

is accompanied by the large-scale, non-Gaussian free energy dissipation for a long period. We hope to further explore how actomyosin networks enter and exit from this unstable state, and how it is related to actin organization and higher-order structure formation.

In this thesis, we connect the actin cytoskeleton system with soft condensed matter physics, which has many interesting scientific outlooks. The large scale condensation in actomyosin networks has been widely observed in reconstituted networks from purified proteins and simulations, including our findings in Chapter 2. Prior research has shown that the condensation of the far-from-equilibrium actomyosin networks can be tuned by varying contractility regulated proteins such as myosin motors and crosslinkers. In Chapters 3 and 4, we show that the speed of filament polymerization serves as the other key parameter that regulates this process by restoring the disorder of the network. It brings up the question of whether we can consider the contractility as the energetic driving force while the filament treadmilling as the entropic driving force for actin network organization. Solving this question may help us to find a universal principle underlying active matter dynamics.

Research discussed in this thesis also contributes several unique implementations, primarily experiment-related functions, to the MEDYAN platform. For example, we designed a system to mimic the atomic force microscope in the first project (Chapter 2), which allows us to apply external point forces during simulation. This system has recently been extended to model filament growth from focal adhesion. The three-step nucleation reactions proposed in the second project (Chap-

ter 3) is now a standard protocol for formin based filament nucleation in MEDYAN simulation. These new implementations have benefited many users in the MEDYAN community, including researchers from the University of Maryland, Georgia State University, Taxes A&M, University of Pennsylvania, Ohio State University, and Duke University. In the future, we would like to extend this setup to more systems, and explore other experiment related frameworks such as microrheology and traction force microscopy.

Appendix A: Supporting Information for Chapter 2

*This chapter is adapted from the published work: Xiaona Li [*], Qin Ni [*], Xiuxiu He, Jun Kong, Soon-Mi Lim, Garegin A Papoian, Jerome P Trzeciakowski, Andreea Trache, and Yi Jiang. "Tensile force-induced cytoskeletal remodeling: Mechanics before chemistry". **PLoS Computation Biology** 16(6): e1007693. (2020) [*]Co-first authors*

A.1 Experimental methods

A.1.1 Vascular smooth muscle cell cultures and transient transfections

VSMC were previously isolated from rat cremaster arterioles [171] and handled as previously described [57]. Briefly, cells were cultured in a smooth muscle cell culture media containing Dulbecco's Modified Eagle Medium (DMEM) supplemented with 10% fetal bovine serum (FBS), 10 mM HEPES (Sigma, St. Louis, MO), 2 mM L-glutamine, 1 mM sodium pyruvate, 100 U/ml penicillin, 100 μg/ml streptomycin and 0.25 μg/ml amphotericin B. Cells were trypsinized and transient transfections were performed according to manufacturer's protocol by using the Nucleofector ap-

paratus (Lonza, formerly Amaxa Biosystems, Gaithersburg, MD) with Nucleofector kit VPI-1004. Then, cells expressing mRFP1-actin-7 were plated on 60 mm MatTek glass bottom dishes (Ashland, MA, USA) in phenol-red free cell culture media, and incubated overnight in 5% CO2 at 37 ˚C. The plasmid mRFP1-Actin-7 was a gift from Michael Davidson (Florida State University, Tallahassee, FL). Unless otherwise specified, all reagents were purchased from Invitrogen (Carlsbad, CA, USA).

A.1.2 Vascular smooth muscle cell imaging

The integrated microscope system used for these studies was described in detail [126]. Briefly, the system was constructed using an inverted Olympus IX-81 microscope (Olympus Corp., NY). An atomic force microscope (XZ Hybrid Head, Bruker Instruments, Santa Barbara, CA) was set on top of the inverted microscope and a Yokogawa CSU 22 spinning-disk confocal attachment was added to the left imaging port of the microscope. This combination of techniques enabled mechanical stimulation of live cells and simultaneous visualization of molecular dynamic events at the subcellular level in real-time. A PLAN APO TIRF 60x oil 1.45 NA objective lens (Olympus Corp., NY) was used for imaging live cells expressing fluorescent protein constructs excited by a Stabilite 2018 RM laser (Spectra Physics/Newport, Mountain View, CA) using a dual 488/568 nm bandpass filter from Chroma Technology (Brattleboro, Vermont). Confocal images were acquired as 3D stacks of 20 planes at a 0.25 mum step size with an exposure time of 100 ms using a QuantEM 512SC camera (Roper Scientific Photometrics, Tuscon, Arizona). The fluorescence

imaging was controlled by Slidebook software (Intelligent Imaging Innovations, Denver, CO).

A.1.3 AFM mechanical stimulation of VSMCs

Tensile stress was applied to live VSMCs using an atomic force microscope probe with a 2 μm glass bead functionalized with fibronectin (Novascan Technologies, IA, USA) [57]. Formation of a functional linkage between the fibronectin on the AFM probe and cortical cytoskeleton via integrins enabled mechanical stimulation of the cell through the application of tensile forces. A mechanical stimulation experiment consists of four segments of force application. First, the probe is brought in contact with the cell for 20min to allow the formation of a functional adhesion through recruitment of integrins and focal adhesion proteins. During this time, the probe rest on the cell surface, and no tensile force is applied. The second step consists of the application of small tensile forces (i.e., mechanical stimulations of 0.2-0.4 nN) to further reinforce the adhesion by enhancing protein recruitment at the respective site. Then, the mechanical stimulation of the cell with low (0.5 nN) and high (1 nN) magnitude forces consisted of controlled upward movement of the cantilever in discrete steps at every 3–5 minute intervals. The same force regime mechanical stimulation was applied for 20–25 minutes each, while the actin cytoskeleton was imaged by spinning-disk confocal microscopy after each force application. The AFM data were acquired using NanoScope (8.15, Bruker) Software and were processed off-line in MATLAB (R2019b, Mathworks) and Excel (Microsoft).

A.1.4 Three-dimensional image analysis

For each raw three-dimensional (3D) image volume at a specific time point, imaging data in z-direction were interpolated by linear interpolation to generate a new sequence. Spatial sizes of a voxel in three dimensions were not all equal, i.e., $\Delta x = \Delta y = 0.178\mu m$, and $\Delta z = 0.25\mu m$. The resulting image sequences were imported to Imaris (v.9.3.0, Oxford Instruments, Inc.) for Automatic Tracing analysis. The coordinates of branch points from the tracing analysis was exported and saved. The 3D coordinates of all paired points that are 10 points apart along a given trace are used to compute the alignment index:

Alignment Index $=< cos\theta >=< \frac{\Delta z}{\sqrt{\Delta x^2+\Delta y^2+\Delta z^2}} >$, (1)

where Δx, Δy, Δz are differences of the paired points in x, y, and z direction, respectively. The resulting set of measurements along each trace were averaged as an estimate for the angle between each trace and the z-axis. As an aggregated measure for trace angles at each time point, angle measures from all traces at a given time point were further averaged.

A.2 Simulation parameters

Chemical Parameters		
Names	Reaction rates (unit of s^{-1})	References
Actin diffusion	80	[20]

α-actinin diffusion	8	[20]
Non-muscle myosin II (NMII) mini-filament diffusion	0.8	[20]
Actin polymerization at plus end	0.151	[4]
Actin polymerization at minus end	0.017	[4]
Actin depolymerization at plus end	1.4	[4]
Actin depolymerization at minus end	0.8	[4]
NMII head binding	0.2	[91]
NMII mini-filament unbinding under no external load	0.2	
α-actinin binding	0.009	[172]
α-actinin unbinding under no external load	0.3	[172]
Mechanical Parameters		
Length of cylindrical actin filament segment	108 nm	[173]
Actin filament bending energy	672.5 pN·nm	[173]
Actin filament stretching constant	100 pN/nm	[20]
Actin filament excluded volume repulsion constant	100000 pN/nm	[20]
NMII head stretching constant	2.5 pN/nm	[174]
α-actinin stretching constant	8 pN/nm	[175]
Boundary repulsion energy	41 pN·nm	[84]
Boundary repulsion screening length	2.7 nm	[84]
Mechanochemical Parameters		
Unbinding force of NMII head	12.6 pN	[176]

Stall force of NMII head	15 pN	[20]
Characteristic unbinding force of α-actinin	17.2 pN	[177]
Characteristic polymerization force of actin filaments	1.5 pN	[178]

Table A.1: Parameters for the simualtions

A.3 Supplementary figures

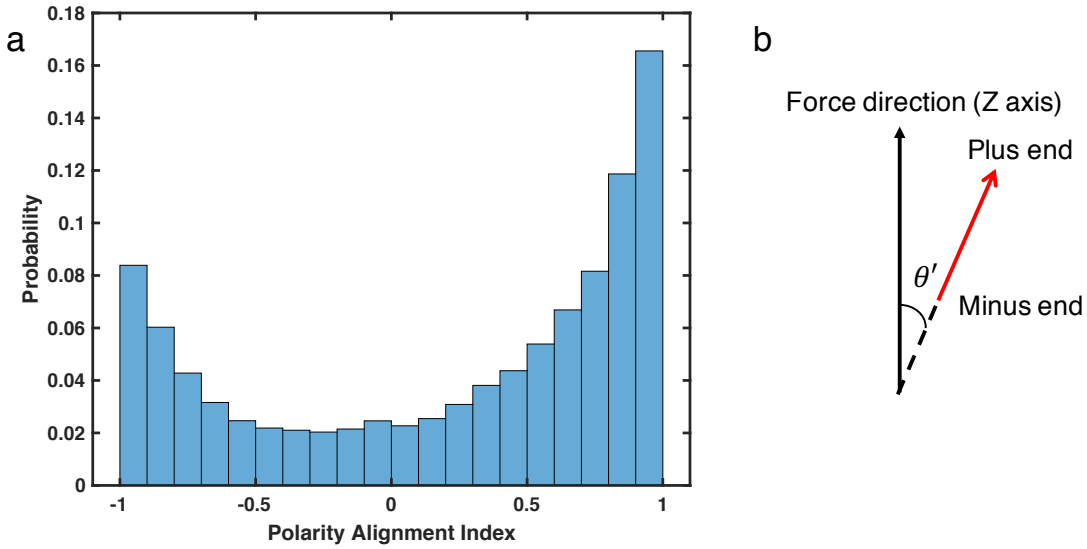

Figure A.1: (a) The probability distribution of filament polarity alignment index for bundle-like networks under pulling condition Case i. Data are taken from t = 751s - 900s out of 5 duplicated trajectories. (b) The polarity alignment index is defined as $\cos' \theta$, where $\prime\theta$ the angle between a filament vector and the force direction. The filament vector (red arrow) in this case, considers the polarity of plus end and minus end. (a-b) The distribution spreads across [-1,1], suggesting that the generated actin bundles have mixed polarity.

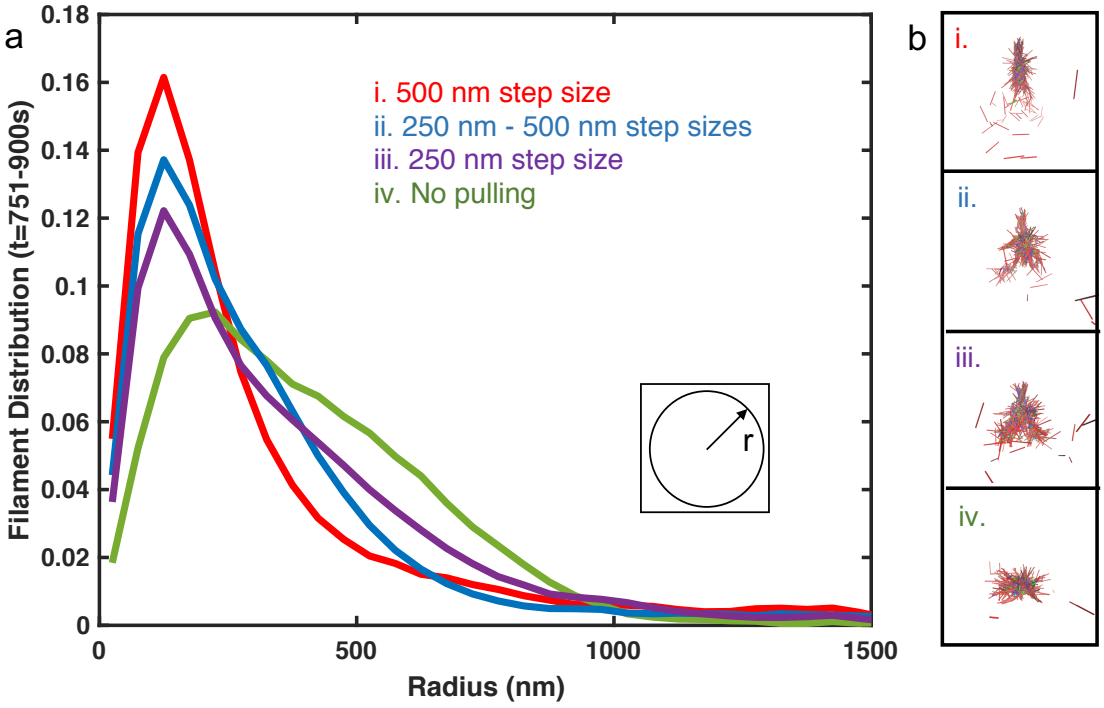

Figure A.2: (a) F-actin radial distribution after the last pulling event (t = 751 - 900s) under pulling condition Case i-iv. (b) Representative snapshots at t = 900s for each case.

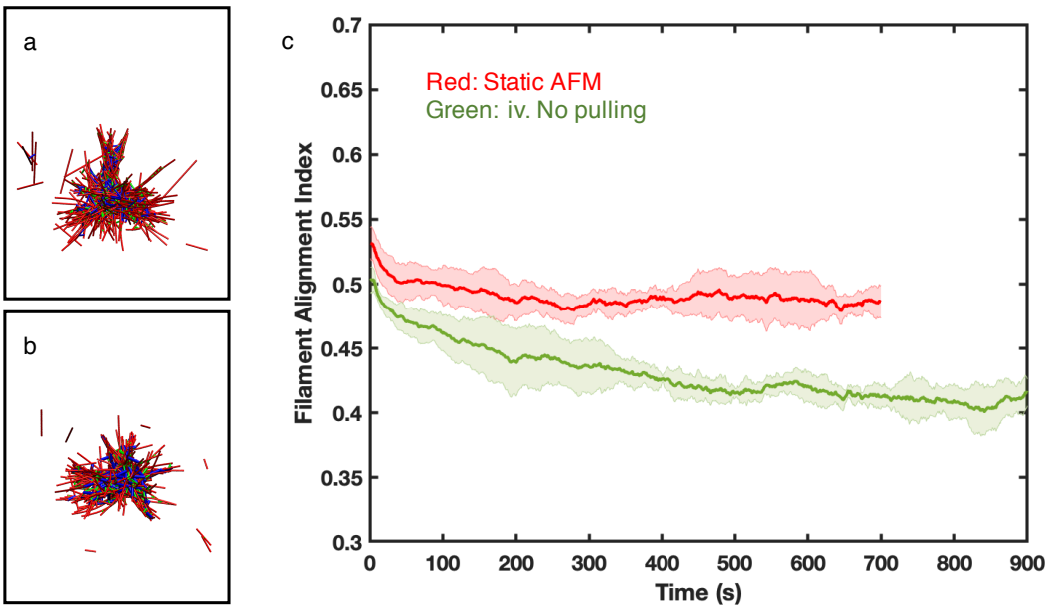

Figure A.3: (a) Representative snapshot of actin network with a static AFM probe at t = 700 s. The height of AFM probe is fixed at 1750 nm. (b) Representative snapshot of actin network with no pulling force (control case iv). (c) The alignment index for static AFM-probe (red) and no force condition (green). Error bars represent the standard deviation from the mean from 5 replicate simulations.

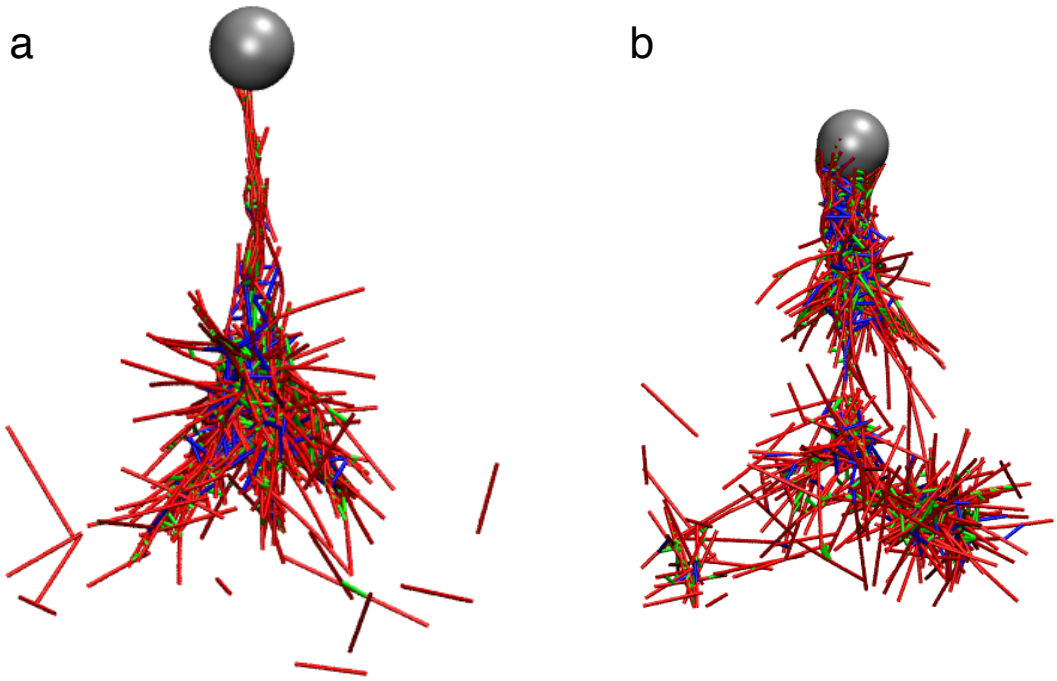

Figure A.4: (a) Representative snapshot of actin network with 5 filaments attached to the AFM probe, after the fifth pulling event (d = 500 nm). (b) Representative snapshot of actin network with 60 filaments attached to the AFM probe, after the fourth pulling event (d = 500 nm). Actin filaments, myosin motors, and crosslinkers are shown in red, blue, and green cylinders, respectively. The gray sphere represents the AFM probe.

Appendix B: Supporting Information for Chapter 3

*This chapter is adapted from the Supplementary Information of the published work: Qin Ni and Garegin A Papoian. "Turnover versus treadmilling in actin network assembly and remodeling". **Cytoskeleton**. ; 76: 562– 570. (2019)*

B.1 Model Details

B.1.1 Time integration method and general simulation protocol in MEDYAN

We carried out all simulations using a publicly available software and force field named MEDYAN (Mechanochemical Dynamics of Active Networks) [20]. MEDYAN has been designed for modeling reaction-diffusion processes, mechanical interactions, and mechanochemical dynamics of active matter networks including, in particular, cytoskeletal systems. It is available at http://www.medyan.org.

Unlike typical constant time-step Langevin based models, the time evolution in MEDYAN simulation is determined by solving the chemical Master Equation using Next Reaction Method (NRM) [86], which is a variation of the Gillespie algorithm [88]. This algorithm samples a stochastic trajectory corresponding to the given

the Master Equation. The sequence of realized chemical events during the time evolution in MEDYAN occurs at specific (yet stochastically chosen) absolute times, including such reactions as polymerization, branching, and nucleation. The time step for the next reaction to happen (τ) is given as,

$$\tau = \frac{1}{a} ln(\frac{1}{r}),$$

where r is a random number between 0 and 1. a, the propensity of a reaction step, is defined as

$$a = \sum_i a_i,$$

where a_i indicates the reaction propensity for the reaction with an index i. Please refer to the original MEDYAN paper [20] and other Gillespie algorithm references for further elaboration [86, 88]. Additional details of all chemical reactions used in this work are further introduced in Text S2.

After the system chemically evolves for some small number of steps, MEDYAN pauses the chemical reactions' engine, to follow by mechanical minimization of the total energy of the system. After the mechanical minimization, a number of reaction propensities may be updated if their kinetics depends on instantaneous mechanical stresses (this being an example of mechanochemical coupling in MEDYAN). This protocol is iterated until reaching the preset overall simulation timescale, which is 2000 seconds in the current work. The above-described pseudo-adiabatic dynamical *ansatz* for active polymer networks was elaborated in the original MEDYAN paper

[20], following earlier works by Hu and Papoian [60, 84, 143]. This approach is supported by recent works indicating that the time to relax local deformation of actin networks [90] is much shorter than the timescale for typical chemical events, such as motor stepping [91] or filament polymerization [4], to happen. Therefore, we take advantage of this significant timescale separation, assuming that the mechanical subsystem almost instantly equilibrates upon chemical perturbations. We favor this time evolution algorithm over the constant time-step Langevin algorithm, because the former significantly reduces the computational cost while maintaining sufficient accuracy.

Further details regarding mechanical models and mechanochemical dynamic rate models used in this work are shown in Text S3-S4.

B.1.2 Reactions and parameters

In MEDYAN, the simulation volume is divided into cubic compartments, in which the diffusing molecules are considered to be homogeneously dissolved. The dimension of the compartments may be chosen by relying on the Kuramoto length of the system [48, 60], with $500nm$ being a reasonable choice for actin-based cytoskeletal networks. We consider that molecular transport between compartments is based on passive diffusion. Actin filament segments can only chemically react with the diffusing molecules in the compartments where they are mutually colocalized. Diffusion is modeled as a hopping process between neighboring compartments,

$$DM_{i_0,j_0,k_0} \rightleftharpoons DM_{i_1,j_1,k_1}.$$

In this reaction, $_{i_0,j_0,k_0}$ annotate the original compartment of the diffusing molecule, while $_{i_1,j_1,k_1}$ annotate the neighboring compartment to where this molecule may be transferred to if this reaction is stochastically selected.

In addition to the diffusion, other chemical reactions considered in this work include: actin polymerization and depolymerization at barbed ends (BE) and pointed ends (PE), CP binding and unbinding from barbed end, nucleation based on Arp2/3 and formin, Arp2/3 dissociation from branchers, formin dissociation from barbed end and destruction of filaments. The polymerization and depolymerization reactions are written as

$$G - actin + BE/PE \longrightarrow F - actin + BE/PE,$$

$$F - actin + BE/PE \longrightarrow G - actin + BE/PE.$$

F-actin is a part of non-diffusive filaments, and BE/PE are also F-actin molecules. A polymerization reaction makes the original BE/PE become a F-actin molecule, where the incoming G-actin becomes the new BE/PE. In a depolymerization event, the original BE/PE becomes a G-actin molecule, and the F-actin next to it would be the new BE/PE.

CP binding and unbinding reactions are written in a similar manner as

$$CP + BE \longrightarrow CBE + F - actin,$$

$$F - actin + CBE \longrightarrow BE + CP.$$

The regular barbed end is replaced by the capped barbed end (CBE), where actin polymerization and depolymerization are terminated.

Names	Parameters	References
Diffusion	$D = 20\mu m^2/s$ $(80s^{-1})$	60
Actin	$k_{on}^{BE} = 11.6(\mu Ms)^{-1}$ $(0.154s^{-1})$	4
	$k_{on}^{PE} = 1.3(\mu Ms)^{-1}$ $(0.017s^{-1})$	
	$k_{off}^{BE} = 1.4s^{-1}$	
	$k_{off}^{BE} = 0.8s^{-1}$	
Arp2/3	$k_{on}^{Arp2/3} = 1 \times 10^{-4}s^{-1}$	This work
	$k_{off}^{Arp2/3} = 0.01s^{-1}$	
CP	$k_{on}^{CP} = 3.98(\mu Ms)^{-1}$ $(0.053s^{-1})$	60
	$k_{off}^{CP} = 0.04s^{-1}$	
Formin	$k_{on}^{formin} = 5 \times 10^{-3}s^{-1}$	This work
	$k_{off}^{formin} = 0.01s^{-1}$	150
Destruction	$k_{destruction} = 1.0s^{-1}$	This work

Table B.1: Parameters for diffusion and reactions.

The Arp2/3 based nucleation reaction depends on G-actin concentration, Arp2/3 concentration and the number of available Arp2/3 binding sites in preexisting filaments as

$$Arp2/3 + G-actin + FreeBindingSite \longrightarrow F-actin + BE + OccupiedBindingSite.$$

In this model, each cylinder have at most one binding site at the center, and each binding site can only bind to one daughter filament. The brancher is a special filaments without a pointed end. Pointed ends can be generated by Arp2/3 unbinding from the brancher and the mother filament:

$$OccupiedBindingSite \longrightarrow Arp2/3 + PE + FreeBindingSite.$$

The body of daughter filaments would remain intact during Arp2/3 dissociation. Both binding rate and unbinding rate constants are chosen arbitrarily to produce a reasonable number of branchers at steady state.

In MEDYAN, the formin nucleation is based on Ref. 135, which is written as a two-step reaction:

$$1. Formin + G - actin \longrightarrow intermediate,$$

$$2. G - actin + intermediate \longrightarrow FBE + F - actin + PE.$$

FBE represents the formin bound barbed end, which has the same polymerization and depolymerization as regular barbed ended (BE) for convenience. We assume step 1 is the rate limiting step and step 2 is a fast step, and rate constants are arbitrary chosen to produce a reasonable nucleation rate. The formin dissociation is similar to CP dissociation, which creates a diffusing formin molecule and a regular barbed end:

$$F - actin + FBE \longrightarrow BE + Formin.$$

In order to balance the filament nucleation, we write a special type of reactions called filament destruction:

$$BE + PE \longrightarrow 2G - actin.$$

The destruction reaction will occur only when a filament has two F-actin molecules,

namely the BE and the PE.

All reaction and diffusion parameters used in this work are summarized in Table B.1.

B.1.3 Mechanical models

A typical cytoskeletal system contains $10^5 \sim 10^9$ actin molecules, making it extremely slow to mechanically model actin filaments as collections of spherical beads. To improve computational efficiency, polymeric actin filaments are coarse grained as connected cylinders in MEDYAN [20]. Each cylinder represents 40 actin monomers, corresponding to $108nm$ in the linear dimension. The persistence length of F-actin filaments is three orders of magnitude larger than their diameter, thus, MEDYAN prohibits bending of above-mentioned elementary cylinder units, allowing only individual cylinders to be stretchable axially as harmonic springs. The stretching potential is given as

$$U_{filament}^{str} = \frac{1}{2} K_{str} (\delta l)^2,$$

where δl is the deviation from the equilibrium length at zero force. Bending of longer actin filaments is realized by the following bending potential between two connected cylinders as

$$U_{filament}^{bending} = K_{bending}(1 - cos(\theta)),$$

where θ is the angle between the two consecutive cylinders. To prevent cylinders from overlapping, the following volume exclusion potential was introduced in MEDYAN,

$$U^{Vol} = \iint_{l_i,l_j} \delta U \mid \vec{r}_i - \vec{r}_j \mid dl_i dl_j,$$

where $\delta U \mid \vec{r}_i - \vec{r}_j \mid = 1/ \mid \vec{r}_i - \vec{r}_j \mid^4$ is a repulsive pair potential between two points located on two interacting cylinders.

In dendritic networks, Arp2/3 branches daughter filament that attaches to the mother filaments at a 70° angle [9]. To mechanically model this specific structural element, MEDYAN employs a combination of stretching, and angular potentials. The corresponding stretching potential is based on the distance between the branching point of mother filaments (i) and the Arp2/3 bound minus end point on daughter (j) as

$$U_{str}^{branch} = \frac{1}{2} K_{str}^{branch} (d_{i,j} - d_0)^2,$$

where $d^{i,j}$ is the distance between the two points and $d_0^{i,j}$ is the equilibrium distance. The angular potential is written as

$$U_{ang}^{branch} = K_{ang}^{branch} (1 - cos(\theta_{i,j} - \theta_0)),$$

where θ is the angle between two cylinder vectors, and θ_0 is set as 70°.

To restrict all filaments inside the simulation domain, boundary boundary repulsion potential is used, as further elaborated in Text S4.

B.1.4 Dynamic rate models

To prevent filaments from growing out of boundary, a boundary repulsion potential is applied as

$$U^{boundary} = \epsilon_{boundary} e^{-d/\lambda},$$

where $\epsilon_{boundary} = 100pm \cdot nm$ is the repulsive force constant, d is the between boundary and filament element and $\lambda = 2.7nm$ is the screening length. The BE polymerization rate is dynamically changed by the boundary force if within 500nm cutoff, where the rate is based on Brownian Ratchet model [89],

$$k_{poly}^{BE} = k_0^{BE} \cdot e^{-F_{boundary}/F_0}.$$

where k_0^{BE} is the bare barbed end polymerization rate under zero external force, $F_{boundary}$ is the boundary force exerted on the actin filament, and $F_0 = 1.5pN$ is the characteristic force based on the thermal energy and the size of actin monomers. The exponential boundary force and the Brownian Ratchet model have minimal effect to filaments unless very close to the boundary, which preserves the accuracy of BE polymerization.

B.1.5 Measurement of turnover halftime, length and treadmilling

In this work, we monitored the actin dynamics of the whole system by recording the actin molecules association/dissociation at barbed ands and pointed ends of all filaments every 1 second. The turnover fraction between any two time frames

can be determined by tracking the actin dynamics (Fig. B.1). The turnover fraction is the ratio of new filamentous actin associated during a specific timescale to the number of F-actin molecules averaged over all snapshots, which is presented as

$$Turnover\ Fraction = \frac{N_{new\ F-actin,t}}{< N_{F-actin} >}.$$

Turnover halftime is the timescale when turnover fraction reaches 0.5. The determination of turnover halftime was similar to FRAP method [37, 43, 136], but our turnover halftime calculation is based on the turnover of the whole system. We make the actin signal intensity equal to 0 at the beginning of each measurement, which is considered as the "photobleaching". Each actin molecules associate to a filament during the measurement would increase the signal intensity by 1, and this filament can either be a preexisting filament or a *de novo* filament. If an actin molecule associates and then dissociates from a filament during the measurement, the signal intensity would be reduced by 1. Dissociation of any filamentous actin molecule that are presented before the measurement would not reduce the signal intensity. We only consider the turnover based on polymerization/depolymerization, and actin diffusion between compartments affects the reaction rate but not considered in turnover measurement. Fig. B.2 shows one measurement of simulated fluorescent recovery (turnover fraction), where we rescale the time such that t = 0 s at the beginning of the measurement.

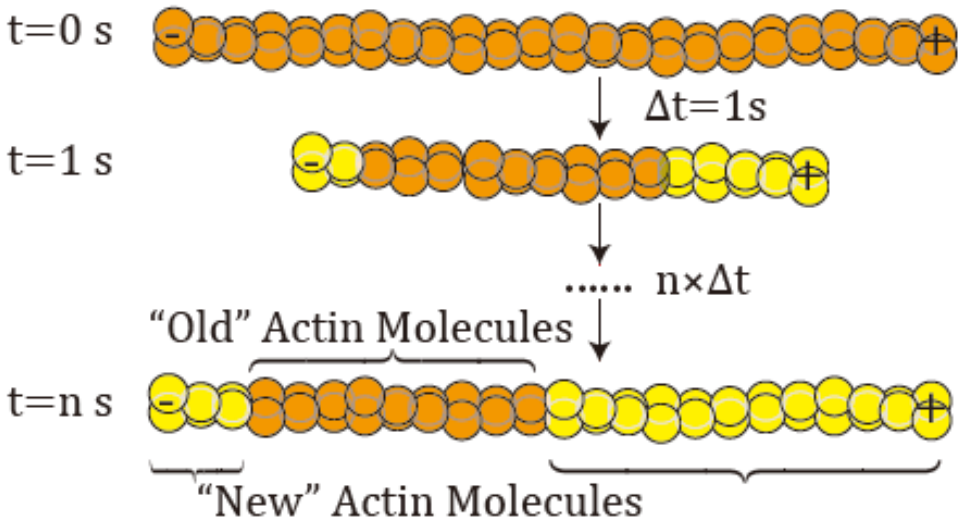

Figure B.1: A sketch showing how turnover fraction is calculated. Actin molecules are "photobleached" at $t = 0s$ (orange beads), and the addition of new actin molecules (yellow beads) are counted. The turnover fraction is calculated via dividing new actin molecules by the total number of actin.

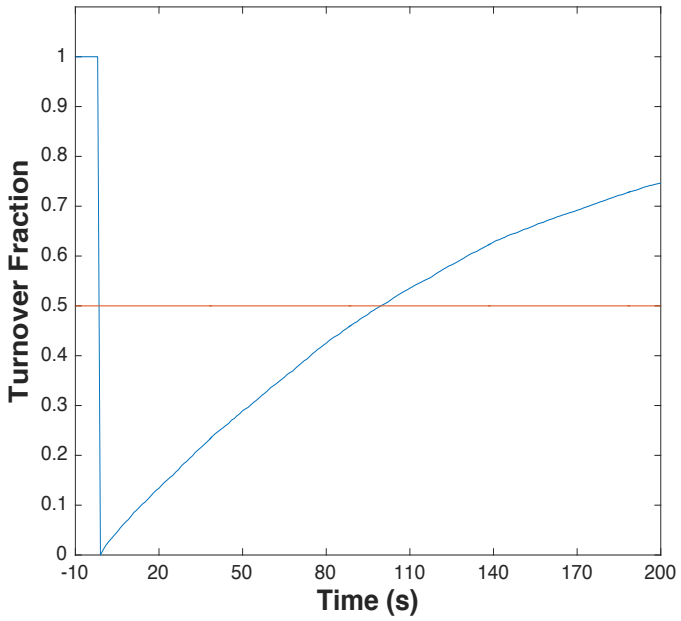

Figure B.2: One measurement of fluorescent recovery (turnover fraction) profile from MEDYAN simulation. Time axis in this plot has been rescaled, where $t = 0s$ is the time when the measurement started. The system contains 5 μM actin, 50 nM Arp2/3 complex and 50 nM CP.

Due to the reaction stochasticity and effects by CPs and Arp2/3 complex, we calculate the treadmilling as an average rate of the whole system by

$$r_{TM} = \frac{\sum N^{BE,i}_{actin,+} - N^{BE,i}_{actin,-}}{N_{filament}} = \frac{\sum N^{PE,i}_{actin,-} - N^{PE,i}_{actin,+}}{N_{filament}},$$

where $N^{BE,i}_{actin,+}$ and $N^{BE,i}_{actin,-}$ are the number of actin molecules associate(+) and dissociate(-) to the barbed end (BE) of filament i, and PE refers to the pointed end. At steady state, the average barbed end elongation rate equals to the average pointed end contraction rate, defined as the treadmilling rate of the network.

The filament length (Fig. B.3) is calculated based on the number of F-actin molecules, where we assume each molecules has a diameter of 2.7 nm due to the two-strand structure of actin filament. Therefore, the average filament length in each snapshot can be represented as

$$< Length >= \frac{\sum (N^{i}_{F-actin} \times 2.7nm)}{N_{filament}},$$

where $N^{i}_{F-actin}$ is the number of filamentous actin molecules in filament i, $N_{filament}$ is the total number of filament in the system.

B.2 Supplementary Figures

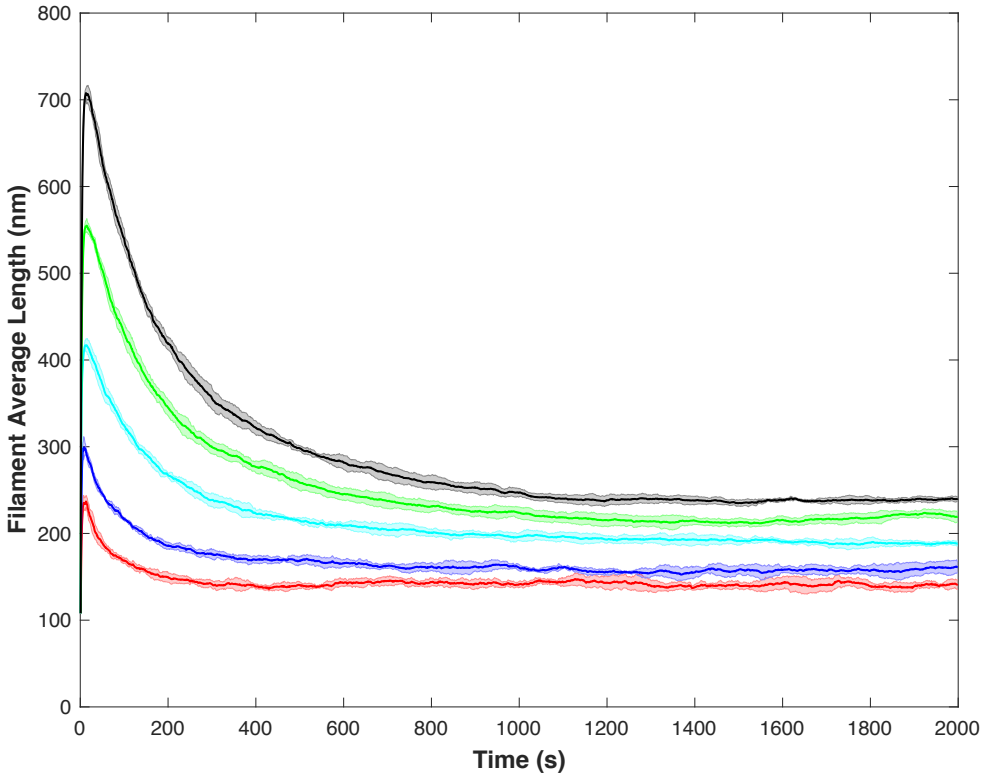

Figure B.3: Filament average length throughout the entire evolution. Total actin concentrations of 3 μM, 5 μM, 10 μM, 15 μM and 20 μM are marked as red, blue, cyan, green and black respectively. Arp2/3 and CP concentrations are fixed at 50nM. Shaded regions represent the standard deviation over trajectories.

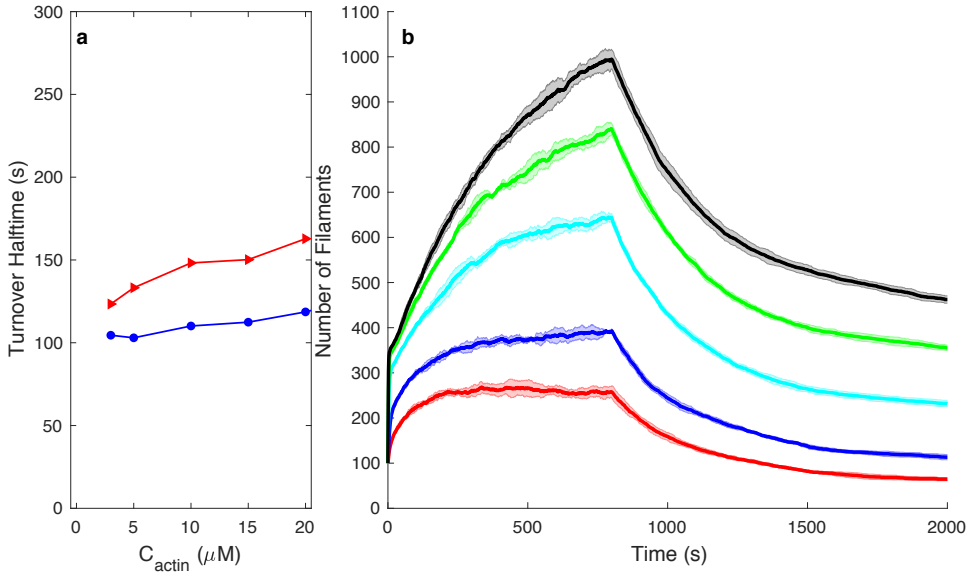

Figure B.4: (a)Turnover halftime of networks with steady state nucleation (blue circle) and without steady state nucleation (red triangle). The nucleator in these systems is Arp2/3, and the steady state nucleation is passivated by stopping Arp2/3 from binding to mother filaments at 800s. (b) The total numbers of filaments decrease after inhibition of nucleation at t = 800s. Total actin concentrations of 3 μM, 5 μM, 10 μM, 15 μM and 20 μM are marked as red, blue, cyan, green and black respectively. Arp2/3 and CP concentrations are fixed at 50nM. Shaded regions represent the standard deviation over trajectories.

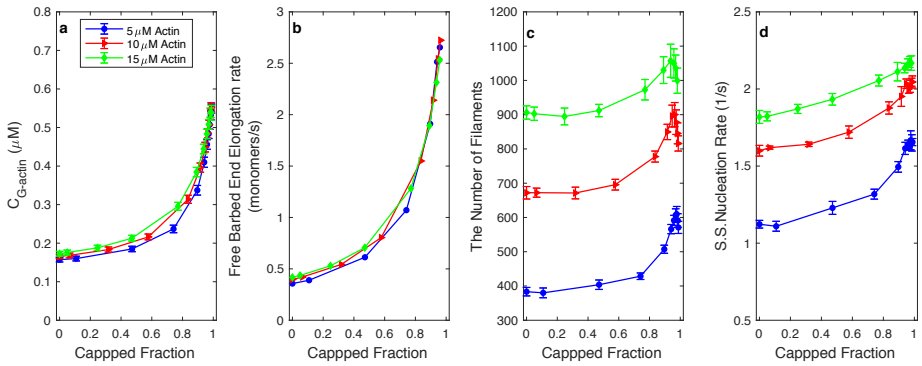

Figure B.5: Capping barbed end "funnels" the critical G-actin concentration (a) and promotes barbed end elongation (b), as proposed by the funneling effect hypothesis. The increases in the total number of filaments (c) and steady state nucleation rate (d) as a function of capped fraction also suggest that CP promotes filament nucleation.

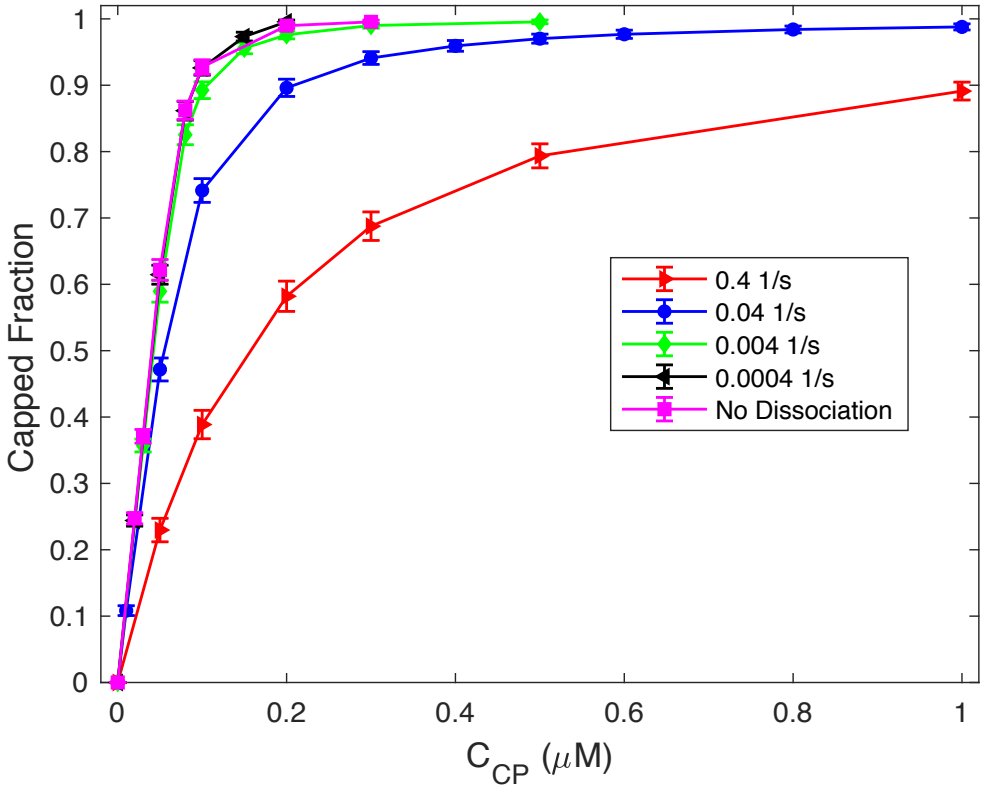

Figure B.6: Capped fraction as a function of CP concentration. The correlation is significant affected by CP dissociation rate. Actin concentration is $5\mu M$ and Arp2/3 concentration is 50 nM.

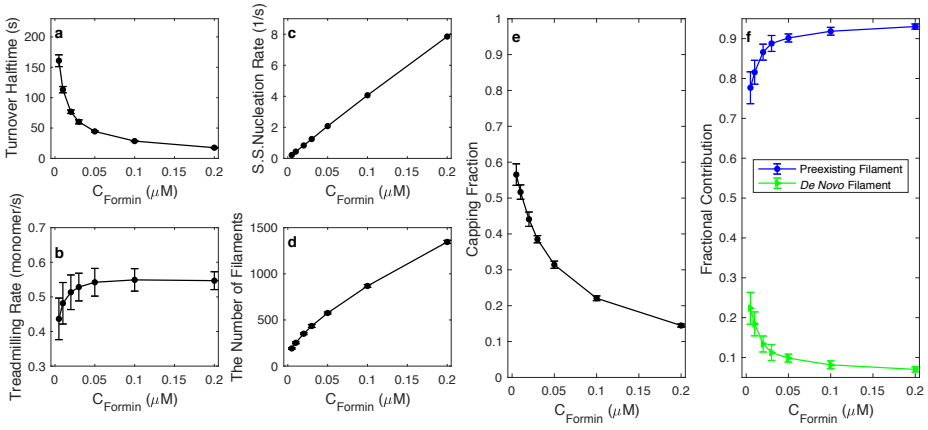

Figure B.7: The turnover halftime (a), treadmilling rate (b), steady state nucleation rate (c), the total number of filaments at steady state (d), capped fraction (e) and the fractional contribution to turnover (f) as a function of formin concentration. Actin concentration is $5\mu M$ and CP concentration is 50nM.

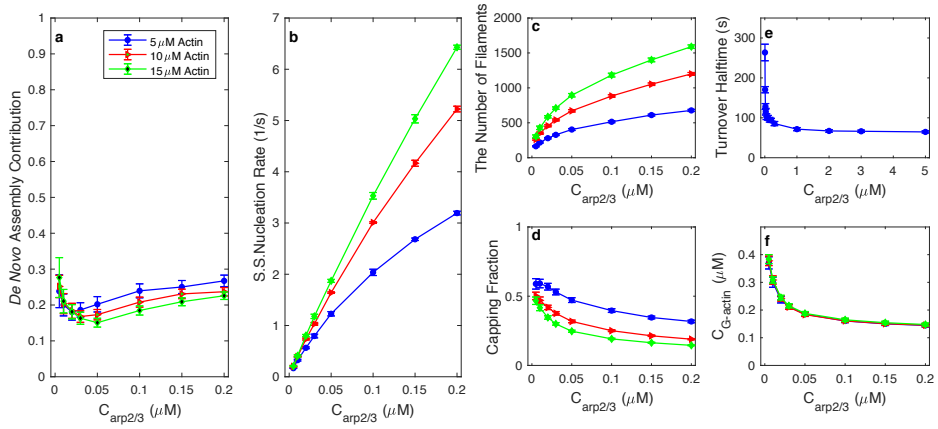

Figure B.8: (a) The *de novo* filaments have insignificant contribution to turnover, and the contribution is insensitive to Arp2/3 concentration. Steady state nucleation rate (b) and the number of filament (c) grow with Arp2/3 concentration. (d) Barbed end capped fraction reduces as increasing Arp2/3 concentration due to the growth of total number of filament. (e) Although Arp2/3 facilitate turnover, the halftime cannot reach lower than ~ $60s$. (f) Free G-actin monomer concentration (critical actin concentration) decrease as $C_{Arp2/3}$ increases. Capping protein concentration is 50nM in all conditions.

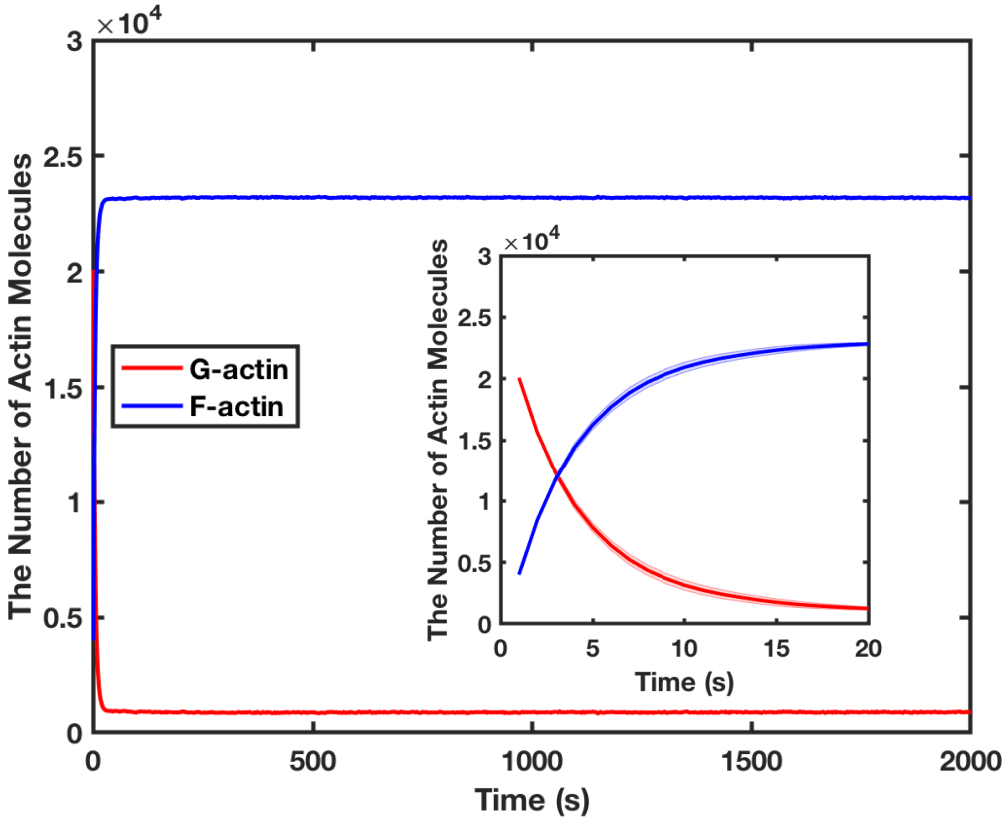

Figure B.9: An example illustrating how G-actin and F-actin concentrations change as a function of time, where the data for the first 20 seconds are additionally shown in the inset. Note that the total concentration of actin is conserved throughout the simulation (5 μM or 24080 molecules in this plot). Shaded regions represent the standard deviation over 5 trajectories.

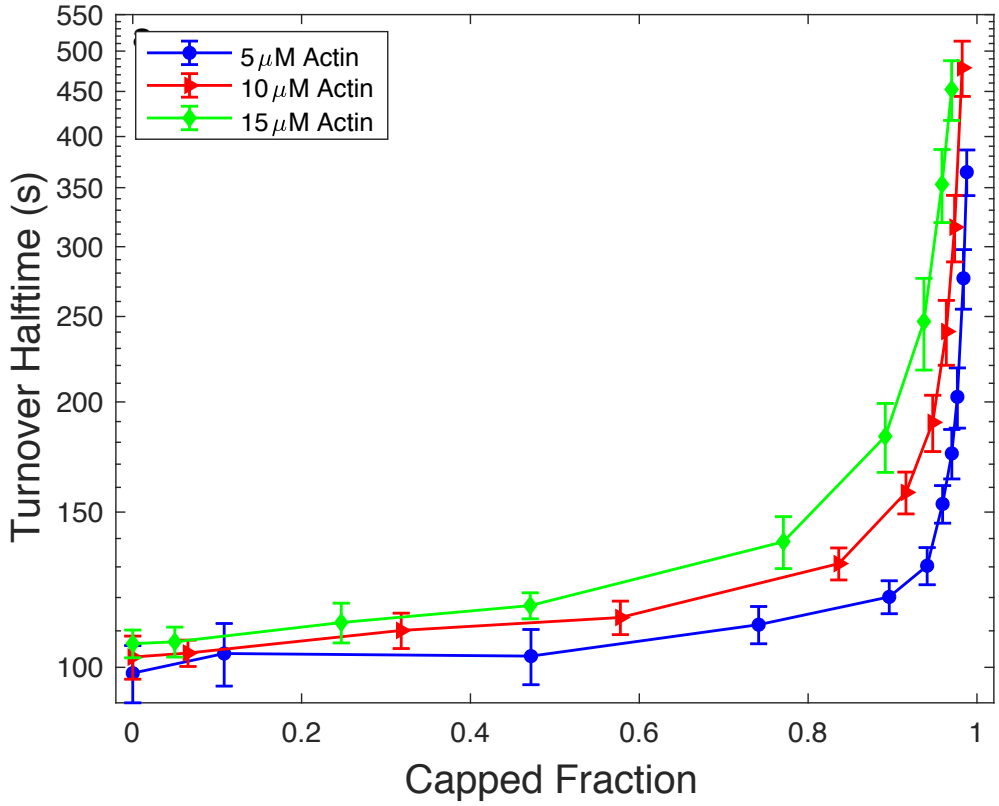

Figure B.10: The semi-log plot of turnover halftime as a function of capped fraction at different actin concentrations $(5 - 15\mu M)$. The nonlogarithmic plot is shown in Fig. 3.3a. Arp2/3 concentration is fixed at $50nM$.

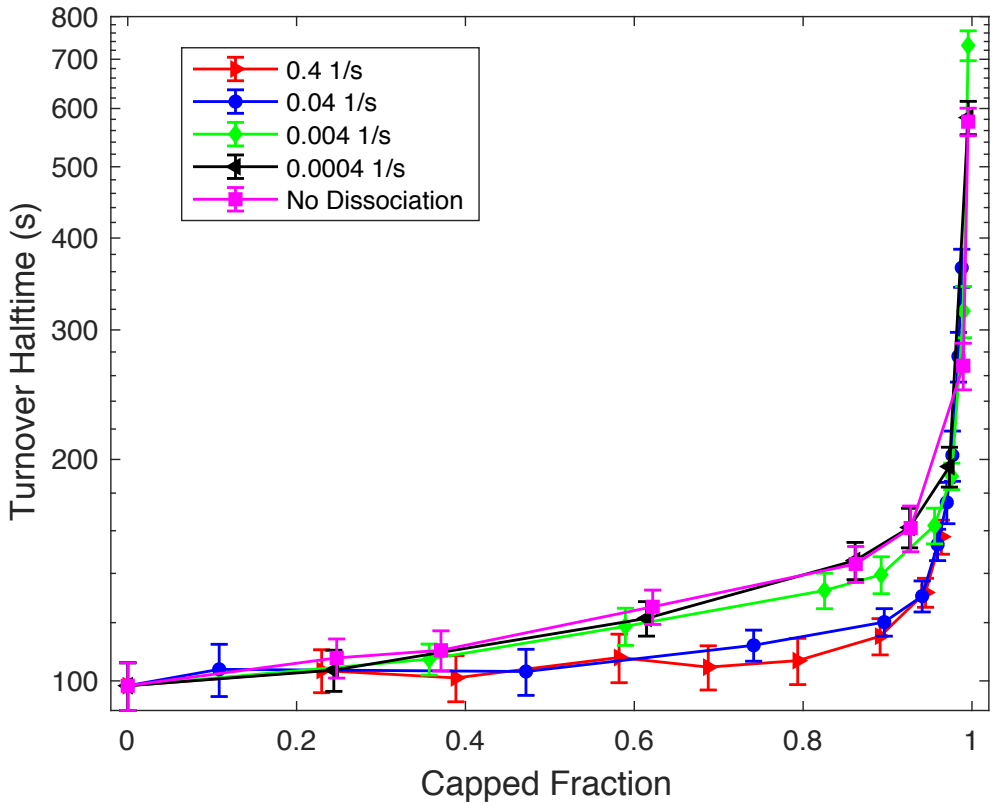

Figure B.11: The semi-log plot of turnover halftime as a function of capped fraction at different CP dissociation rates. The nonlogarithmic plot is shown in Fig. 3.4a. Arp2/3 concentration is fixed at $50nM$.

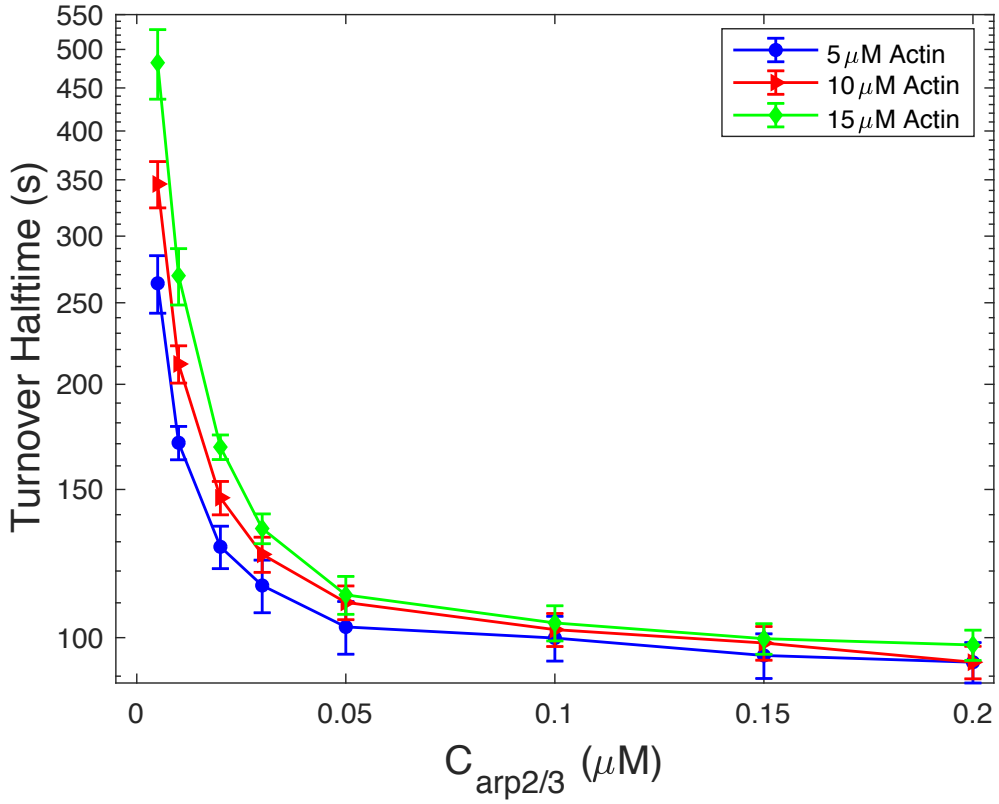

Figure B.12: The semi-log plot of turnover halftime as a function of Arp2/3 concentration at different actin concentration $(5 - 15\mu M)$. The nonlogarithmic plot is shown in Fig. 3.5d. CP concentration is fixed at $50nM$.

Appendix C: Supporting Information for Chapter 4

This chapter is adapted from the Supplementary Information of the published work: Qin Ni, Kaustubh Wagh, Arpita Upadhyaya and Garegin A Papoian. "Filament treadmilling induces phase transition in actomyosin networks." In preparation. (2020)

C.1 Computational Model Details

The simulations presented in this work were carried out via MEDYAN (Mechanochemical Dynamics of Active Networks). MEDYAN is an open-source mechanochemical simulation tool and force field (available at www.medyan.org) of active matters developed by the Papoian Lab at University of Maryland, College Park [20]. We employed MEDYAN to model complex stochastic reaction-diffusion, mechanical interaction, and mechanochemical dynamics of active cytoskeletal networks.

In MEDYAN, the simulation space is divided into a solution phase and a polymer phase. All diffusing molecules (DM) are dissolved in the solution phase, including G-actin, and unbound formin, non-muscle myosin II (NMII), and crosslinker molecules. To reduce the computational cost without losing too much spatial information, the solution phase is discretized into many linear compartments. The dimension of the compartment is carefully chosen based on the Kuramoto length

of actin, which is the mean-free path that molecules are expected to diffuse before undergoing their next reaction [60]. In the 3D spherical network, compartments are 500 nm × 500 nm × 500 nm cubes. In quasi 2D cylindrical networks, the compartment dimension in the Z-axis is reduced to $400nm$ (the mechanical boundary is $200nm$ as restricted by boundary repulsion potential, see Section 1.2 for details). Diffusing molecules are assumed to be well-mixed within each compartment without specific locations, and the transport of molecules between compartments is modeled as a diffusion reaction within the solution phase.

On the other hand, polymeric filaments and bound formin, NMIIs and crosslinkers are dissolved in the polymer phase that lays over the solution phase. This phase accounts for the mechanical modeling of boundary repulsion, steric interactions, bending and stretching of filaments, as well as the stretching of linkers and motors. When polymerization, nucleation, NMII or crosslinker binding reactions happen, diffusing molecules will be transfered from the solution phase into the polymer phase. The depolymerization, filament destruction, NMII or crosslinker unbinding reactions will release molecules from the polymer phase to solution phase.

In the following sections, we will further discuss details of our chemical models (including diffusion), mechanical models, mechanochemical coupling, and the simulation protocol.

C.1.1 Mechanical models

Unlike the traditional bead-spring model, the semi-flexible filaments are represented as connected cylinders. The equilibrium length (under zero force) of each cylinder elements varies from 2.7nm (1 actin monomer) to a maximum of 108nm (40 actin monomers). Addition (depletion) of each actin monomer would increase(decrease) the length of the first or last cylinders by 2.7nm. If a cylinder has reached the maximum allowed length, a new cylinder will be created upon a polymerization event.This coarse-graining method significantly reduces the number of mechanical elements in the system, while still maintaining sufficient accuracy. Filaments have a very large aspect ratio, i.e., the persistence length of a filament ($\sim 20\mu m$) is much larger than its diameter ($\sim 10nm$). Thus, it is reasonable to only allow axial deformation of a cylinder (stretching). The stretching potential is represented as

$$U^{str}_{filament} = \frac{1}{2} K^{str}_{filament} (l_f - l_{f,0})^2,$$

where l_f is the actual length of cylinder under force, and $l_{f,0}$ is the equilibrium length based on the number of actin monomers on this cylinder (each monomer is 2.7nm). Filament bending is realized by bending between two connected cylinders:

$$U^{bending}_{filament} = K^{bending}_{filament} (1 - cos(\theta - \theta_0)),$$

where θ is the angle between the two consecutive cylinders under force, while θ_0 is the equilibrium angle that is set to be 0. A novel volume exclusion exclusion

potential is also implemented to prevent cylinders overlapping, which is written as

$$U^{Vol} = \iint_{l_i,l_j} \delta U \mid \vec{r}_i - \vec{r}_j \mid dl_i dl_j,$$

where $\delta U \mid \vec{r}_i - \vec{r}_j \mid = 1/ \mid \vec{r}_i - \vec{r}_j \mid^4$ is the pair potential between two points located on the two interacting cylinders. $\vec{r}_i$ amd $\vec{r}_j$ are the distance between any two points along the cylinder i and j. This potential can provide a steep enough volume exclusion effect while remain analytically solvable.

Names	Parameters	References
Cylinder stretching	$K^{str}_{filament} = 100pN/nm$	20
Cylinder bending	$K^{bending}_{filament} = 672pN \cdot nm$	173
Filament volume exclusion	$K_{vol} = 10^5 pN/nm^4$	20
Linker stretching	$K^{str}_{linker} = 8pN/nm$	175
NMII stretching	$K^{str}_{NMII} = 2.5pN/nm$ per head	174
Boundary repulsion	$\epsilon_{boundary} = 100pN \cdot nm$	This work

Table C.1: Mechanical parameters.

Bound NMIIs and linkers are modeled as harmonic springs as

$$U^{str}_{NMII/linker} = \frac{1}{2} K^{str}_{NMII/linker} (l_{NMII/linker} - l_{NMII/linker,0})^2.$$

$l_{linker,0}$ is the equilibrium length of a linker, which is set as the distance between the binding sites when a linker binding reaction happens. $l_{NMII,0}$ is also initialized when a motor binding reaction occurs, however, it is reset every time a motor walking reaction occurs.

In order to confine all the filaments within the simulation boundary, a boundary repulsion potential is implemented. In the quasi-2D system, the actual height of the network is set to be 400 nm, and the diameter is 4000 nm. However, filaments would occasionally move out of the mechanical boundary due to rapid treadmilling, leading to simulation failures. To prevent this, we shift the boundary barrier slightly inside the network by a_0, and the exponential boundary repulsion is written as

$$U^{boundary} = \epsilon_{boundary} e^{-(d-a_0)/\lambda},$$

where $\epsilon_{boundary} = 100pm \cdot nm$ is the repulsive energy constant, d is the distance between boundary and filament element, and $\lambda = 2.7nm$ is the screening length. The boundary shifting factor a_0 is chosen to be 100 nm based on experience. The existence of a_0 restricts the effective network boundary to be height = 200 nm and diameter = 1900 nm.

The mechanical model parameters can be found in Table C.1.

C.1.2 Chemical models

The chemical engine of MEDYAN is powered by an efficient stochastic Next Reaction Method (NRM) [86], which is based on the Gillespie algorithm [88] but is more computationally efficient. Overall, the NRM stochastically solves the chemical Master Equation that generates a trajectory of chemical events. In this work, we consider the following chemical reactions: diffusion, filament polymerization, filament depolymerization, nucleation based on formin, destruction of filaments, binding of

myosin motor and linker, and motor walking reaction.

The diffusion of molecules between compartments is modeled as a simple transport process as

$$DM_{i_0,j_0,k_0} \rightleftharpoons DM_{i_1,j_1,k_1},$$

where the diffusing molecules are originally located in compartment $_{i_0,j_0,k_0}$, and is transfered to compartment $_{i_1,j_1,k_1}$.

Filament (F-actin) polymerization and depolymerization can occur at both barbed end (BE) and pointed end (PE) of a filament. These reactions are written as

$$G-actin + BE/PE \longrightarrow F-actin + BE/PE,$$

$$F-actin + BE/PE \longrightarrow G-actin + BE/PE.$$

It should be noted that BE and PE are F-actin molecules at two end points of a filament.

The nucleation reaction is presented as a two-step reaction based on the mechanism of formin nucleation [36, 135]:

$$1. Formin + G-actin \longrightarrow intermediate,$$

$$2. G-actin + intermediate \longrightarrow FBE + F-actin + PE.$$

The intermediate is an arbitrary molecule that consists of a formin and a G-actin molecule. We assume step 1 is the rate-limiting step and step 2 is a fast step,

Names	Parameters	References
Diffusion	$D_{actin,arp2/3,CP} = 20\mu M^2/s$	60
Actin	$k_{on}^{BE} = 11.6 - 34.8(\mu M \cdot s)^{-1}$	4 and this work
	$k_{on}^{PE} = 1.3(\mu M \cdot s)^{-1}$	
	$k_{off}^{BE} = 1.4s^{-1}$	
	$k_{off}^{PE} = 0.8 - 2.4s^{-1}$	
Destruction	$k_{destruction} = 1.0 - 1.9s^{-1}$	This work
Nucleation	$k_{nu} = 0.005s^{-1}$	36
Formin dissociation	$k_{off}^{formin} = 0.01s^{-1}$	150
Alpha-actinin	$k_{on}^{\alpha} = 0.7(\mu M \cdot s)^{-1}$	172
	$k_{on}^{\alpha} = 0.3s^{-1}$	
NMII head binding	$k_{on}^{M} = 0.2s^{-1}$	91
	$k_{on}^{M} = 1.7s^{-1}$	20

Table C.2: Parameters for diffusion and reactions.

thus this intermediate would rapidly react with a G-actin and become a filament with a pointed end, a regular F-actin, and a formin bound barbed end (FBE). For simplicity, polymerization and depolymerization at FBE are the same as regular barbed end reactions. The formin can dissociate from a filament that releases a formin and creates a regular F-actin barbed end on that filament:

$$F - actin + FBE \longrightarrow BE + Formin.$$

Since nucleation keeps creating new filaments, the filament destruction process is required to establish a steady state that keeps the total number of filaments constant. The destruction reaction occurs exclusively when a filament has only two

F-actin molecules (a BE and a PE), which destroy this filament and release two diffusing G-actin molecules as

$$BE + PE \longrightarrow 2G - actin.$$

The binding reactions of myosin motors and linkers are carried out in a slightly different protocol. Before a binding reaction is to happen, a pair of binding sites at neighboring filaments would be stochastically chosen. The distance between the two binding sites ranges from 175 to 225 nm [16] for NMII, and 30-40 nm for alpha-actinin [118] . After the binding site pair is determined, the binding reaction would convert a diffusing motor or linker to a bound motor or linker with two ends attaching to the two binding sites, creating a mechanical linkage. This linkage vanishes when an unbinding reaction occurs, releasing the motor or linker to the diffusing pool. It should be noted that Non-muscle Myosin II mini-filaments (NMII) used in this work consists of 15-30 myosin heads [179]. To mimic this property, the reaction rate for each NMII binding event is scaled by the number of myosin heads that are randomly chosen within this specific range.

In an active cytoskeleton, myosin motors consume energy from ATP hydrolysis and actively walk along filaments, which is one of the most important sources for force generation. In MEDYAN, a motor stepping reaction is implemented to mimic this effect. For a bound NMII, the stepping reaction is written as

$$NMII_i \longrightarrow NMII_{i+1},$$

where i and $i+1$ are the NMII locations on the filament before and after walking. NMII is a barbed end walking motor, thus $i+1$ represents the next binding site towards the barbed end.

Parameters for diffusion and chemical reactions can be found in Table C.2.

C.1.3 Mechanochemical models

Many cytoskeletal reactions, including actin polymerization, myosin motor binding and stepping, and linker binding, have been shown to be mechanical sensitive. To capture this feature, MEDYAN implements mechanochemical models that explicitly allow force-dependent chemical reaction rates.

Names	Parameters	References
Characteristic polymerization force	$F_{poly,0} = 1.5pN$	178
Characteristic linker unbinding force	$F_{linker,unbind} = 17.2pN$	177
NMII duty ratio	$\rho = 0.1$	91
NMII stall force	$F_{stall} = 12.62pN$ per head	176
Tunable parameters	$\beta = 0.2$	20
	$\gamma = 0.05pN^{-1}$	
	$\xi = 0.1$	

Table C.3: Mechanochemical dynamic rate parameters.

The effect of boundary force on filament polymerization is described by the Brownian Ratchet model [89], which models the force sensitive polymerization rate constant k_{poly} as:

$$k_{poly} = k^0_{poly} \cdot \exp(-F_{ext}/F_{poly,0}),$$

where k^0_{poly} is the bare polymerization rate under zero external force, F_{ext} is the boundary repulsive force exerted on the filament ends, and $F_{poly,0}$ is the characteristic polymerization force based on the thermal energy and the size of actin monomers.

We used a simple exponential equation to model the slip bond property of alpha-actinin crosslinker:

$$k_{linker,unbind} = k^0_{linker,unbind} \cdot \exp(F_{linker,stretching}/F_{linker,unbind}),$$

where $k^0_{linker,unbind}$ is the unbinding rate constant under zero external force, and $F_{linker,unbind}$ is the characteristic unbinding force of alpha-actinin. $F_{linker,stretching}$ is the stretching force on the linker, while the compressing force on linker does not trigger the slip bond model.

In this work, we model NMII binding as a catch bond, as adapted from the Parallel Cluster Model [176], such that the force loaded on NMII can reduce its unbinding rate constant:

$$k_{NMII,unbind} = \frac{\beta \cdot k^0_{NMII,unbind}}{N_{bound}} \cdot (\frac{-F_{ext}}{N_{bound} \cdot F_{NMII,unbind}}),$$

where β is a tunable parameter, $k^0_{NMII,unbind}$ is the unbinding rate constant under zero force, and F_{ext} is the total stretching force applied on the NMII. The number of heads bound to the filament, N_{bound}, increases linearly as the force:

$$N_{bound} = \rho \cdot N_{total} + \gamma \cdot F_{ext},$$

where ρ is the duty ratio, andγ is another tunable parameter. N_{total} is the total number of NMII heads that can bind to filament, which is randomly chosen during each motor binding reaction.

The NMII walking rate is also mechanochemically sensitive and can be modeled as in a Hill type force-velocity relation:

$$k_{walk} = k^0_{walk} \cdot \frac{F_{stall} - F_{ext}/N_{total}}{F_{stall} + F_{NMII,pulling}/(N_{total} \cdot \xi)},$$

where F_{stall} is the stall force of single NMII head, $F_{NMII,pulling}$ is the pulling force on NMII in the opposite direction of walking movement, and ξ is a tunable parameter.

The mechanochemical model parameters can be found in Table C.3.

C.1.4 Simulation protocol

The relaxation time for local deformations of actin networks [90] is much shorter than the timescale of typical chemical events such as motor stepping [91] or filament polymerization [4], thereby creating a significant separation of timescales. Hence, the mechanical equilibrium process can be viewed as a pseudo-adiabatic process that can be separated from chemical reactions. Based on this hypothesis, the simulation can be carried out as the following:

1. Chemical reactions occur that evolve the time of the system stochastically.

2. Pausing chemical reactions when the time step reaches a preset time value. The system mechanically minimizes the total energy.

3. Reaction rates are updated based on the mechanical conditions after mini-

mization.

4. Going back to step 1 based on the updated reaction rates.

This protocol is iterated until reaching 2000 s of simulation, or until reaching the 2-week wall time on the Deepthought2 High-Performance Computing cluster at University of Maryland, College Park.

All the networks are initialized with 100 seed filaments, each 1 cylinder long (108nm). Filament polymerization, depolymerization, nucleation, and destruction start immediately. We allow these networks to evolve for 300s before adding myosin motors and linkers. For each condition, we run 5 duplicated trajectories. The R_{median} (median of filament radial distribution) of each duplicated trajectory at different conditions are plotted in Fig. C.1.

C.2 Defining treadmilling rate and treadmilling inhibition simulation setups

Although the treadmilling in cells is a complex system that involves hundreds of reactions [3, 138], it is simplified to four reactions in this work by considering polymerization and depolymerization at both barbed ends and pointed ends. When a steady state is established, the net barbed end growth rate will equal to the net pointed ends reduction rate (averaged over the system), maintaining a constant average filament length. Therefore, we can define a kinetic steady state for treadmilling by monitoring the average filament length of the network as shown in Fig. C.2. We found that a kinetic steady state could be established after 1000s in all conditions,

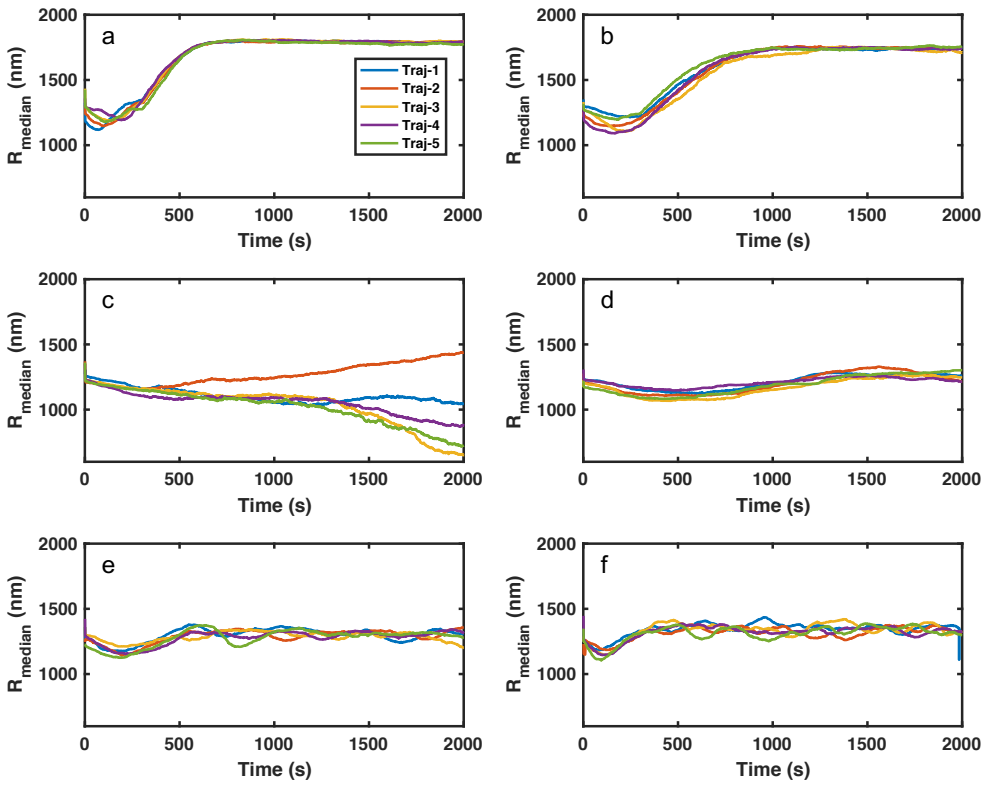

Figure C.1: (a-b)5 R_{median} trajectories of ring-like actomyosin networks at $\langle r_{TM} \rangle$ = $2.05s^{-1}$ (standard deviation SD = $0.07s^{-1}$) and $\langle r_{TM} \rangle$ = $1.25s^{-1}$ (SD = $0.05s^{-1}$). The mean R_{median} trajectory is shown in Fig. 1a-i. (c) 5 trajectories of geometrically collapsed networks at $r\langle r_{TM} \rangle$ = $0.56s^{-1}$ (SD = $0.05s^{-1}$). The mean R_{median} trajectory as shown in Fig. 1a-iii. (d-f) 5 trajectories of networks with no NMII and alpha-actinin at $\langle r_{TM} \rangle$ = $0.57s^{-1}$ (SD = $0.04s^{-1}$), $\langle r_{TM} \rangle$ = $1.41s^{-1}$ (SD = $0.06s^{-1}$), and $\langle r_{TM} \rangle$ = $2.21s^{-1}$ (SD = $0.09s^{-1}$) respectively.

and we have examined that at this steady state the average barbed end elongation rate is almost the same as the average pointed end shrinkage rate. Hence, we quantify the average treadmilling rate $\langle r_{TM} \rangle$ as the average barbed end elongation rate after 1000s. It should be noted that the steady state does not exist in any individual filaments due to the stochastic reaction-diffusion scheme of MEDYAN.

While the treadmilling rate is an elegant and robust way of quantifying the speed of actin network assembly, it is extremely hard to measure *in vivo*. An alternative way to quantify the speed of actin network remodeling is to measure the turnover timescale, which has been widely studied via an experimental technique called Fluorescent Recovery After Photobleaching (FRAP) [36]. To compare with experiments, we use a process similar to FRAP to calculate the turnover halftime ($t_{1/2}$, the time required for a network to reach 50% turnover) in our simulation, and we obtain $t_{1/2} \sim 168s$ for the slowest treadmilling condition, and $t_{1/2} \sim 48s$ for the most rapid treadmilling case. It should be noted that our longest $t_{1/2}$ is similar to the turnover timescale of some reconstitute networks [15], and our shortest $t_{1/2}$ is comparable to that of *in vivo* actin cortices [42]. The details of turnover halftime measurement in MEDYAN and how it is related to treadmilling has been discussed in depth in a prior computational study [36].

We utilized kinetic parameters measured *in vitro* [4] as the baseline to assemble the slow treadmilling networks as shown Fig. 1a-b, iii. To explore suitable parameters for rapidly treadmilling networks, we looked into the effects of formin and ADF/cofilin. An earlier work [8] has shown that the presence of formin can promote the polymerization rate at the barbed end to nearly 4 times the baseline.

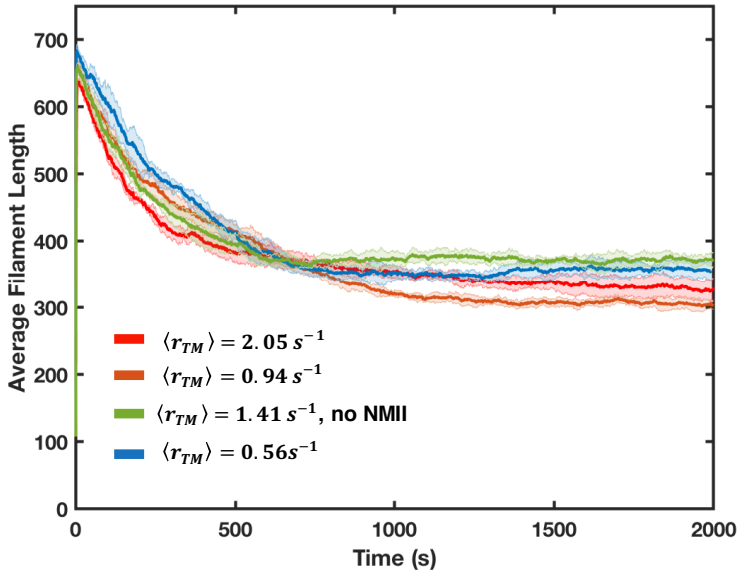

Figure C.2: Average filament length as a function of time. Shaded color represents the standard deviation of mean (5 run per condition).

For simplicity, we imitated this effect by increasing the barbed end polymerization rate constant (k_{on}^{BE}) of all filaments. ADF/cofilin can also promote treadmilling by severing filaments. Importantly, the fragment that contains the pre-existing pointed end is very unstable and would undergo rapidly disassembly [15]. This observation allows us to mimic the effect of ADF/cofilin by simply increasing the depolymerization at the pointed end (k_{off}^{PE}). For example, we increase the k_{on}^{BE} and k_{off}^{PE} to three-fold in the actin ring network as shown in Fig. 1a-b, i.

It is difficult to tune the polymerization and depolymerization rate constants at both end *in vivo*. We indirectly perturb filament assembly and disassembly in T cells by treating them with Latrunculin A (LatA). Earlier works have shown that LatA affects the filament treadmilling in two ways: it sequesters G-actin while also accelerating the phosphate release from ADP-Pi-actin thereby reducing filament polymerization while increasing depolymerization at both ends [1, 155, 156]. We

disrupted r_{TM} by reducing k_{on}^{BE}, and increasing both k_{off}^{BE} (barbed end depolymerization rate constant) and k_{off}^{PE}.Since the pointed end polymerization rate constant is much smaller than the other three parameters [4], for simplicity, we keep it constant during these perturbation simulations.

We ran the simulations with different rate constants until we found a parameter space that mimicked the effect of LatA treatment. In the weak inhibition case, we decreased k_{on}^{BE} to $11.6(\mu M \cdot s)^{-1}$, increased k_{off}^{BE} to $2.1s^{-1}$, and maintained k_{off}^{PE} at $2.4s^{-1}$. In the strong inhibition case, k_{on}^{BE} is decreased to $3.48(\mu M \cdot s)^{-1}$, k_{off}^{BE} is increased to $11.2s^{-1}$, and k_{off}^{PE} is increased to $4.8s^{-1}$. In all simulations, pointed end polymerization rate constant is maintained at $1.3(\mu M \cdot s)^{-1}$.

C.3 Experimental methods

C.3.1 Cell culture and transfection

E6.1 Jurkat T cells were grown in RPMI medium supplemented with 10% Fetal Bovine Serum (FBS) and 1% penicillin-streptomycin at 37°C in a CO_2 incubator. Transfections were performed with 2×10^5 cells using $1\mu g$ of plasmid by electroporation using a Neon electroporation kit (Thermo Fisher Scientific). Prior to imaging, 1mL of cells were centrifuged at 2×10^5 for 5 minutes. The supernatant was aspirated and the cells were resuspended in CO_2 independent L-15 medium (Fisher Scientific).

C.3.2 Plasmids and reagents

pEGFP-C1 F-tractin-EGFP was a gift from Dyche Mullins (Addgene plasmid # 58473; http://n2t.net/addgene:58473 ; RRID:Addgene_58473) [180]. Latrunculin A was purchased from Sigma Aldrich and its vehicle, dimethyl sulfoxide (DMSO) was purchased from Thermo Fisher Scientific.

C.3.3 Preparation of glass coverslips

Sterile 8-well chambers (Cellvis) were incubated with 0.01% poly-L-lysine solution in distilled water for 10 minutes and then dried at 37°C for 1 hour. Poly-L-lysine coated chambers were then incubated with anti-human CD3 antibody (HIT3a clone, Thermo Fisher Scientific) in PBS at a concentration of $1\mu g/mL$ for 2 hours at 37°C or overnight at 4°C. Following incubation, the chambers were washed 5 times with L-15 and warmed prior to imaging.

C.3.4 Microscopy

Transfected T cells were seeded on anti-CD3 coated glass coverslips and allowed to activate for 5 minutes. Chambers were maintained at 37°C using a stage-top incubator (Okolab). Latrunculin A or vehicle (DMSO) were added at specified concentrations 5 minutes after seeding the cells. Fluorescence and interference reflection microscopy images were acquired using an inverted microscope (Ti-E, Nikon, Melville, NY) with a scientific CMOS camera (Prime BSI, Photometrics, Tucson, AZ) with a frame interval of 2 seconds. EGFP-FTractin was imaged using total in-

ternal reflection fluorescence (TIRF), using a 60X, 1.49 NA oil immersion objective; EGFP was imaged using a 488 nm laser for excitation. One background image was captured during every session in order to perform background subtraction.

C.3.5 Image analysis

Initial preprocessing of images was done using FIJI. A custom MATLAB script was written to perform background subtraction. The IRM images were used to find the outline and centroid of the cells. 50 uniformly spaced lines were drawn from the centroid and these 50 line profiles were pooled together to generate a histogram of intensities as a function of a normalized distance to the centroid. The median of the distribution of intensities (and hence F-actin) were estimated for each time point.

C.4 Supplementary Figures

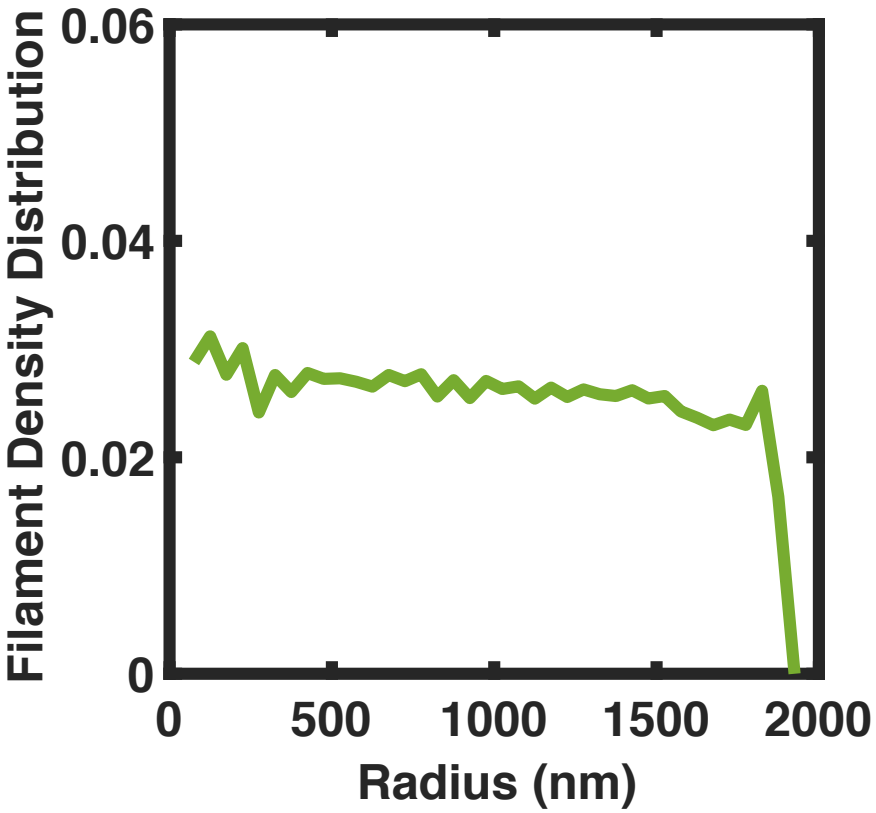

Figure C.3: Filament radial density of disordered networks with $\langle r_{TM} \rangle$ = $1.41s^{-1}$. Data are taken at last 500s. 5 runs per condition

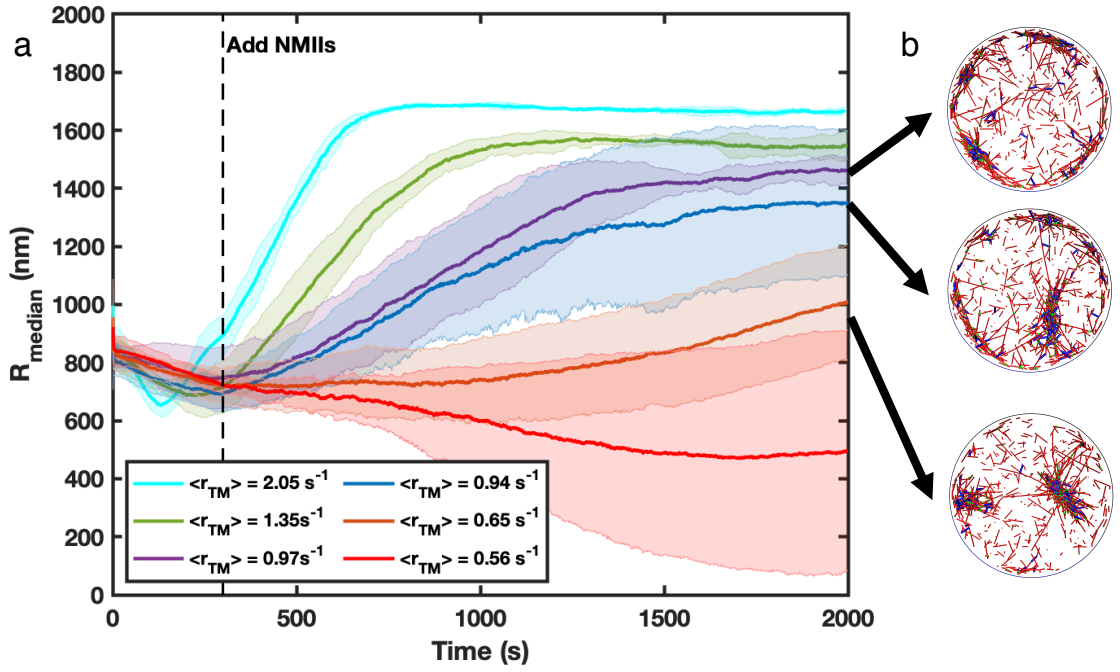

Figure C.4: (a) Median of filament radial density distribution of actomyosin networks at different treadmilling rates as a function of time. Actin ring emerges when $\langle r_{TM} \rangle = 0.97 - 2.05 s^{-1}$, and $\langle r_{TM} \rangle = 0.56 - 0.94 s^{-1}$ induces cluster formation. At $\langle r_{TM} \rangle = 0.94 s^{-1}$, networks are ring-like with significant local clustering. (b) The most representative snapshots of the network with $\langle r_{TM} \rangle = 0.94 s^{-1}$ (upper), $0.97 s^{-1}$ (middle), and $0.65 s^{-1}$ (lower).

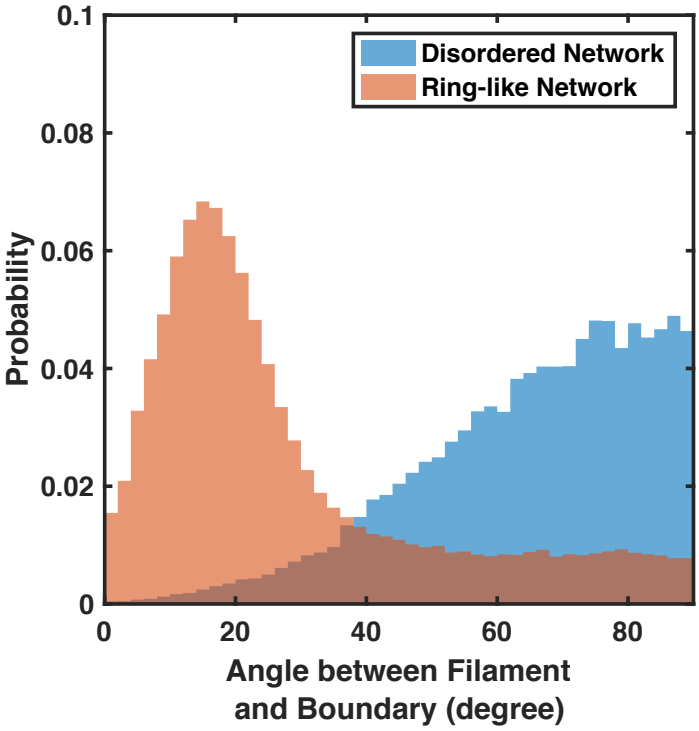

Figure C.5: The distribution of filament orientations for disordered networks and ring-like networks (Fig. 1a-i) near the network periphery ($r > 1600nm$). More filaments are oriented perpendicularly to the boundary in disordered networks. Polymerization at the barbed end is inhibited due to stronger ratcheting, leading to fewer filaments surviving at long timescales in myosin-free networks. The filament orientation is represented by the angle between the treadmilling direction (the non-bendable barbed end cylinder) and the tangent vector to the boundary. Only filaments longer than 200nm are counted. The angle ranges from 0° to 90°, with 0° indicating treadmilling parallel to the boundary and 90° indicating treadmilling perpendicular to the boundary. 5 runs per condition.

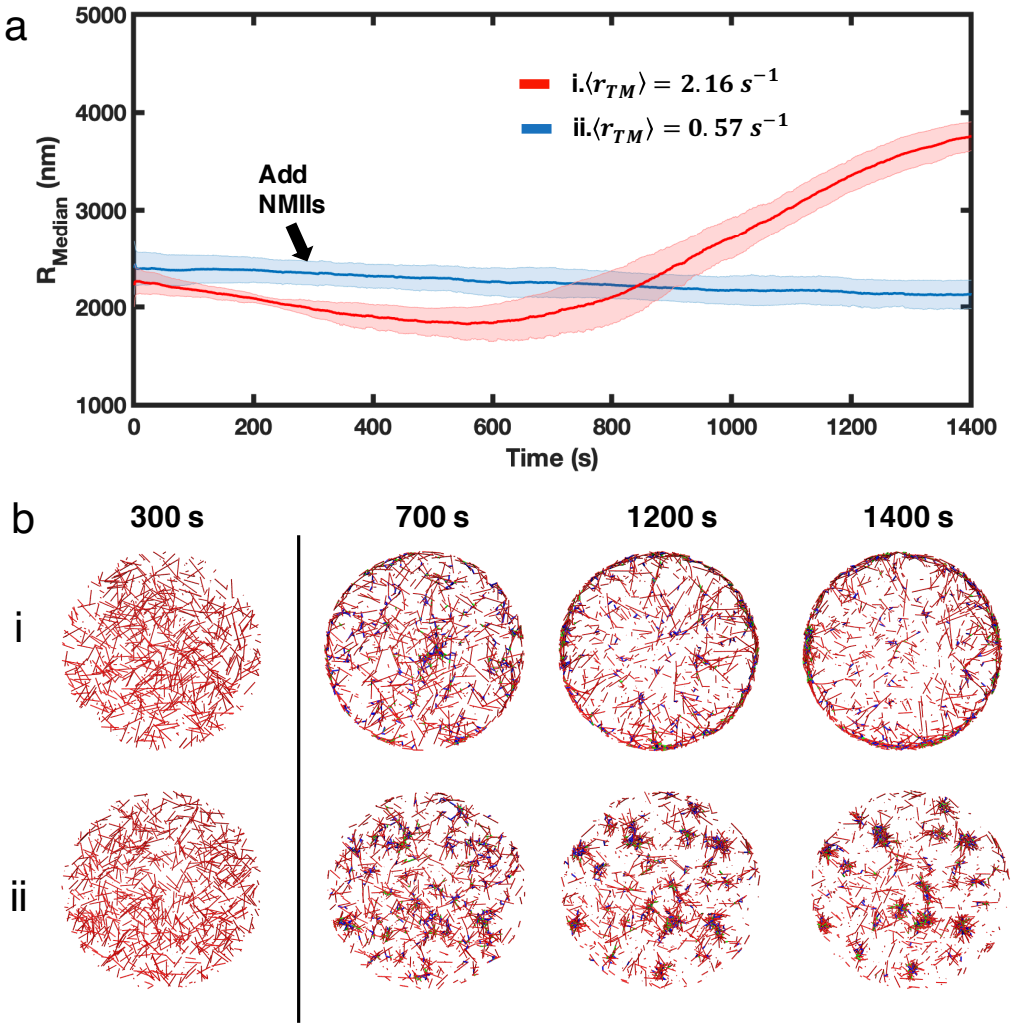

Figure C.6: (a) Median of filament radial density distribution (R_{median}) at different treadmilling speeds. Networks are quasi-2D disk with 10 µm in diameter and 200 nm in height. The network contains 20 µM and 100 nm filament nucleator. 0.03 µM of NMII and 2 µM alpha-actinin are added at t = 300 s.

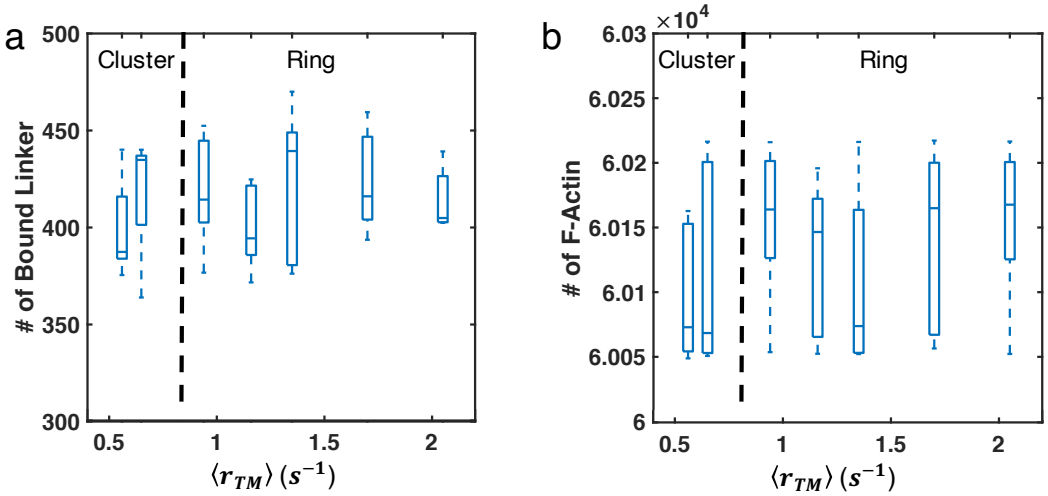

Figure C.7: (a-b) Box plots of the number of bound linker (a) and F-actin (b) in the system. Almost all motors are bound upon addition, thus we do not provide a plot for the number of bound motor.

Bibliography

[1] Ikuko Fujiwara, Mark E. Zweifel, Naomi Courtemanche, and Thomas D. Pollard. Latrunculin A accelerates actin filament depolymerization in addition to sequestering actin monomers. *Current Biology*, 28(19):3183–3192.e2, 2018.

[2] F Gittes, B Mickey, J Nettleton, and J Howard. Flexural rigidity of microtubules and actin filaments measured from thermal fluctuations in shape. *The Journal of Cell Biology*, 120(4):923–34, 1993.

[3] Thomas D Pollard. Regulation of actin filament assembly by Arp2/3 complex and formins. *Annual Review of Biophysics and Biomolecular Structure*, 36(February):451–77, 2007.

[4] I Fujiwara, D Vavylonis, and T D Pollard. Polymerization kinetics of ADP- and ADP-Pi-actin determined by fluorescence microscopy. *Proceedings of the National Academy of Sciences of the United States of America*, 104(21):8827–8832, may 2007.

[5] Julie A. Theriot. The polymerization motor. *Traffic*, 1(1):19–28, 2000.

[6] Thomas Pollard, William Earnshaw, Jennifer Lippincott-Schwartz, and Graham Johnson. *Cell Biology*. 3rd edition, 2016.

[7] Sally H. Zigmond. Formin-induced nucleation of actin filaments. *Current Opinion in Cell Biology*, 16(1):99–105, jan 2004.

[8] David R. Kovar, Elizabeth S. Harris, Rachel Mahaffy, Henry N. Higgs, and Thomas D. Pollard. Control of the assembly of ATP- and ADP-actin by formins and profilin. *Cell*, 124(2):423–435, 2006.

[9] R. D. Mullins, J. A. Heuser, and T. D. Pollard. The interaction of Arp2/3 complex with actin: Nucleation, high affinity pointed end capping, and formation of branching networks of filaments. *Proceedings of the National Academy of Sciences of the United States of America*, 95(11):6181–6186, 1998.

[10] Tatyana M. Svitkina and Gary G. Borisy. Arp2/3 complex and actin depolymerizing factor/cofilin in dendritic organization and treadmilling of actin filament array in lamellipodia. *The Journal of Cell Biology*, 145(5):1009–26, may 1999.

[11] Marc Edwards, Adam Zwolak, Dorothy A. Schafer, David Sept, Roberto Dominguez, and John A. Cooper. Capping protein regulators fine-tune actin assembly dynamics. *Nature Reviews Molecular Cell Biology*, 15(10):677–689, 2014.

[12] Dennis Breitsprecher, Antje K. Kiesewetter, Joern Linkner, Marlene Vinzenz, Theresia E.B. Stradal, John Victor Small, Ute Curth, Richard B. Dickinson, and Jan Faix. Molecular mechanism of Ena/VASP-mediated actin-filament elongation. *EMBO Journal*, 30(3):456–467, 2011.

[13] Melanie Barzik, Tatyana I. Kotova, Henry N. Higgs, Larnele Hazelwood, Dorit Hanein, Frank B. Gertler, and Dorothy A. Schafer. Ena/VASP proteins enhance actin polymerization in the presence of barbed end capping proteins. *Journal of Biological Chemistry*, 280(31):28653–28662, 2005.

[14] W. Brieher. Mechanisms of actin disassembly. *Molecular Biology of the Cell*, 24(15):2299–2302, 2013.

[15] Patrick M. McCall, Frederick C. MacKintosh, David R. Kovar, and Margaret L. Gardel. Cofilin drives rapid turnover and fluidization of entangled F-actin. *Proceedings of the National Academy of Sciences of the United States of America*, 116(26):12629–12637, 2019.

[16] Thomas D. Pollard. Structure and polymerization of acanthamoeba myosin-ii filaments. *Journal of Cell Biology*, 95(3):816–825, 1982.

[17] Todd Thoresen, Martin Lenz, and Margaret L. Gardel. Thick filament length and isoform composition determine self-organized contractile units in actomyosin bundles. *Biophysical Journal*, 104(3):655–665, 2013.

[18] Nilushi L. Dasanayake, Paul J. Michalski, and Anders E. Carlsson. General Mechanism of Actomyosin Contractility. *Physical Review Letters*, 107(11):118101, sep 2011.

[19] José Alvarado, Michael Sheinman, Abhinav Sharma, Fred C. Mackintosh, and Gijsje H. Koenderink. Molecular motors robustly drive active gels to a critically connected state. *Nature Physics*, 9(9):591–597, 2013.

[20] Konstantin Popov, James Komianos, and Garegin A. Papoian. MEDYAN: Mechanochemical Simulations of Contraction and Polarity Alignment in Actomyosin Networks. *PLOS Computational Biology*, 12(4):1–35, 2016.

[21] Ian Linsmeier, Shiladitya Banerjee, Patrick W. Oakes, Wonyeong Jung, Taeyoon Kim, and Michael P. Murrell. Disordered actomyosin networks are sufficient to produce cooperative and telescopic contractility. *Nature Communications*, 7:12615, 2016.

[22] Michael P Murrell and Margaret L Gardel. F-actin buckling coordinates contractility and severing in a biomimetic actomyosin cortex. *Proceedings of the National Academy of Sciences of the United States of America*, 109(51):20820–20825, 2012.

[23] Taeyoon Kim, Margaret L. Gardel, and E. D. Munro. Determinants of fluidlike behavior and effective viscosity in cross-linked actin networks. *Biophysical Journal*, 106(3):526–534, 2014.

[24] Tzer Han Tan, Maya Malik-Garbi, Enas Abu-Shah, Junang Li, Abhinav Sharma, Fred C. MacKintosh, Kinneret Keren, Christoph F. Schmidt, and Nikta Fakhri. Self-organized stress patterns drive state transitions in actin cortices. *Science Advances*, 4(6):eaar2847, jun 2018.

[25] Jing Li, Thomas Biel, Pranith Lomada, Qilin Yu, and Taeyoon Kim. Buckling-induced F-actin fragmentation modulates the contraction of active cytoskeletal networks. *Soft Matter*, 13(17):3213–3220, 2017.

[26] Sean X. Sun, Sam Walcott, and Charles W. Wolgemuth. Cytoskeletal cross-linking and bundling in motor-independent contraction. *Current Biology*, 20(15):R649–R654, aug 2010.

[27] James E. Komianos and Garegin A. Papoian. Stochastic ratcheting on a funneled energy landscape is necessary for highly efficient contractility of actomyosin force dipoles. *Physical Review X*, 8(2):21006, may 2018.

[28] Laurent Blanchoin, Rajaa Boujemaa-Paterski, Cécile Sykes, and Julie Plastino. Actin dynamics, architecture, and mechanics in cell motility. *Physiological Reviews*, 94(1):235–263, 2014.

[29] Aron B. Jaffe and Alan Hall. Rho GTPases: Biochemistry and biology. *Annual Review of Cell and Developmental Biology*, 21:247–269, 2005.

[30] Christopher C. Beltzner and Thomas D. Pollard. Pathway of actin filament branch formation by Arp2/3 complex. *Journal of Biological Chemistry*, 283(11):7135–7144, 2008.

[31] Kirsi Riento and Anne J Ridley. Rocks: multifunctional kinases in cell behaviour. *Nature reviews Molecular cell biology*, 4(6):446–56, jun 2003.

[32] M. L. Gardel, J H Shin, F C MacKintosh, L Mahadevan, P Matsudaira, and D A Weitz. Elastic behavior of cross-linked and bundled actin networks. *Science*, 304(5675):1301–5, may 2004.

[33] M L Gardel, F Nakamura, J H Hartwig, J C Crocker, T P Stossel, and D A Weitz. Prestressed F-actin networks cross-linked by hinged filamins replicate mechanical properties of cells. *Proceedings of the National Academy of Sciences of the United States of America*, 103(6):1762–7, feb 2006.

[34] T. Pujol, O. du Roure, M. Fermigier, and J. Heuvingh. Impact of branching on the elasticity of actin networks. *Proceedings of the National Academy of Sciences of the United States of America*, 109(26):10364–10369, 2012.

[35] Orkun Akin and R. Dyche Mullins. Capping Protein Increases the Rate of Actin-Based Motility by Promoting Filament Nucleation by the Arp2/3 Complex. *Cell*, 133(5):841–851, 2008.

[36] Qin Ni and Garegin A. Papoian. Turnover versus treadmilling in actin network assembly and remodeling. *Cytoskeleton*, 76(11-12):562–570, 2019.

[37] Marco Fritzsche, Alexandre Lewalle, Tom Duke, Karsten Kruse, and Guillaume Charras. Analysis of turnover dynamics of the submembranous actin cortex. *Molecular Biology of the Cell*, 24(6):757–67, 2013.

[38] Tasnuva Sarowar and Andreas M. Grabrucker. Actin-dependent alterations of dendritic spine morphology in shankopathies. *Neural Plasticity*, 2016:8051861, 2016.

[39] Minakshi Guha, Mian Zhou, and Yu Li Wang. Cortical actin turnover during cytokinesis requires myosin II. *Current Biology*, 15(8):732–736, 2005.

[40] Kimberly M. Stroka, Hongyuan Jiang, Shih Hsun Chen, Ziqiu Tong, Denis Wirtz, Sean X. Sun, and Konstantinos Konstantopoulos. Water permeation drives tumor cell migration in confined microenvironments. *Cell*, 157(3):611–623, 2014.

[41] Michael Murrell, Patrick W Oakes, Martin Lenz, and Margaret L Gardel. Forcing cells into shape: the mechanics of actomyosin contractility. *Nature Reviews Molecular Cell Biology*, 16(8):486–498, aug 2015.

[42] Guillaume Salbreux, Guillaume Charras, and Ewa Paluch. Actin cortex mechanics and cellular morphogenesis. *Trends in Cell Biology*, 22(10):536–545, 2012.

[43] Frank PL Lai, Malgorzata Szczodrak, Jennifer Block, Jan Faix, Dennis Breitsprecher, Hans G Mannherz, Theresia EB Stradal, Graham A Dunn, J Victor Small, and Klemens Rottner. Arp2/3 complex interactions and actin network turnover in lamellipodia. *The EMBO Journal*, 27(7):982–992, 2008.

[44] Stéphanie Pellegrin and Harry Mellor. Actin stress fibers. *Journal of Cell Science*, 120(20):3491–3499, 2007.

[45] Douglas N Robinson, Guy Cavet, Hans M Warrick, and James A Spudich. Quantitation of the distribution and flux of myosin-II during cytokinesis. *BMC Cell Biology*, 3:4, 2002.

[46] Jason Yi, Xufeng S. Wu, Travis Crites, and John A. Hammer. Actin retrograde flow and actomyosin II arc contraction drive receptor cluster dynamics at the immunological synapse in Jurkat T cells. *Molecular Biology of the Cell*, 23(5):834–852, 2012.

[47] King Lam Hui, Lakshmi Balagopalan, Lawrence E Samelson, and Arpita Upadhyaya. Cytoskeletal forces during signaling activation in Jurkat T-cells. *Molecular Biology of the Cell*, 26(4):685–95, 2015.

[48] Yueheng Lan and Garegin A Papoian. The stochastic dynamics of filopodial growth. *Biophysical journal*, 94(10):3839–52, 2008.

[49] Pavel I. Zhuravlev and Garegin A. Papoian. Molecular noise of capping protein binding induces macroscopic instability in filopodial dynamics. *Proceedings of the National Academy of Sciences of the United States of America*, 106(28):11570–11575, 2009.

[50] Erdinç Atilgan, Denis Wirtz, and Sean X. Sun. Mechanics and dynamics of actin-driven thin membrane protrusions. *Biophysical Journal*, 90(1):65–76, 2006.

[51] S. Tojkander, G. Gateva, and P. Lappalainen. Actin stress fibers - assembly, dynamics and biological roles. *Journal of Cell Science*, 125(8):1855–1864, apr 2012.

[52] Kyle Kurpinski, Julia Chu, Craig Hashi, and Song Li. Anisotropic mechanosensing by mesenchymal stem cells. *Proceedings of the National Academy of Sciences of the United States of America*, 103(44):16095–16100, oct 2006.

[53] Margaret L Gardel, Ian C Schneider, Yvonne Aratyn-Schaus, and Clare M Waterman. Mechanical integration of actin and adhesion dynamics in cell migration. *Annual Review of Cell and Developmental Biology*, 26(4):315–33, apr 2010.

[54] Dong Hwee Kim and Denis Wirtz. Predicting how cells spread and migrate: Focal adhesion size does matter. *Cell Adhesion and Migration*, 7(3):293–296, 2013.

[55] Pirta Hotulainen and Pekka Lappalainen. Stress fibers are generated by two distinct actin assembly mechanisms in motile cells. *Journal of Cell Biology*, 173(3):383–394, 2006.

[56] Sari Tojkander, Gergana Gateva, Galina Schevzov, Pirta Hotulainen, Perttu Naumanen, Claire Martin, Peter W. Gunning, and Pekka Lappalainen. A molecular pathway for myosin II recruitment to stress fibers. *Current Biology*, 21(7):539–550, 2011.

[57] Soon Mi Lim, Jerome P Trzeciakowski, Harini Sreenivasappa, Lawrence J Dangott, and Andreea Trache. RhoA-induced cytoskeletal tension controls adaptive cellular remodeling to mechanical signaling. *Integrative Biology (United Kingdom)*, 4(6):615–627, jun 2012.

[58] Theresia E.B. Stradal, Klemens Rottner, Andrea Disanza, Stefano Confalonieri, Metello Innocenti, and Giorgio Scita. Regulation of actin dynamics by WASP and WAVE family proteins. *Trends in Cell Biology*, 14(6):303–311, jun 2004.

[59] Alexander Leithner, Alexander Eichner, Jan Müller, Anne Reversat, Markus Brown, Jan Schwarz, Jack Merrin, David J. J. de Gorter, Florian Schur, Jonathan Bayerl, Ingrid de Vries, Stefan Wieser, Robert Hauschild, Frank P. L. Lai, Markus Moser, Dontscho Kerjaschki, Klemens Rottner, J. Victor Small, Theresia E. B. Stradal, and Michael Sixt. Diversified actin protrusions promote environmental exploration but are dispensable for locomotion of leukocytes. *Nature Cell Biology*, 18(11):1253–1259, 2016.

[60] Longhua Hu and Garegin A Papoian. Mechano-chemical feedbacks regulate actin mesh growth in lamellipodial protrusions. *Biophysical Journal*, 98(8):1375–84, apr 2010.

[61] Marcus Prass, Ken Jacobson, Alex Mogilner, and Manfred Radmacher. Direct measurement of the lamellipodial protrusive force in a migrating cell. *Journal of Cell Biology*, 174(6):767–772, sep 2006.

[62] Y. Marcy, J. Prost, M.-F. Carlier, and C. Sykes. Forces generated during actin-based propulsion: A direct measurement by micromanipulation. *Proceedings of the National Academy of Sciences of the United States of America*, 101(16):5992–5997, apr 2004.

[63] Fabian Heinemann, Holger Doschke, and Manfred Radmacher. Keratocyte lamellipodial protrusion is characterized by a concave force-velocity relation. *Biophysical Journal*, 100(6):1420–7, mar 2011.

[64] Sapun H. Parekh, Ovijit Chaudhuri, Julie A. Theriot, and Daniel A. Fletcher. Loading history determines the velocity of actin-network growth. *Nature Cell Biology*, 7(12):1119–1123, 2005.

[65] Thomas D. Pollard and Gary G. Borisy. Cellular motility driven by assembly and disassembly of actin filaments. *Cell*, 112(4):453–465, 2003.

[66] Ikuko Fujiwara, Kirsten Remmert, Grzegorz Piszczek, and John A. Hammer. Capping protein regulatory cycle driven by CARMIL and V-1 may promote actin network assembly at protruding edges. *Proceedings of the National Academy of Sciences of the United States of America*, 111(19), 2014.

[67] Janet H. Iwasa and R. Dyche Mullins. Spatial and Temporal Relationships between Actin-Filament Nucleation, Capping, and Disassembly. *Current Biology*, 17(5):395–406, 2007.

[68] Jiaxiang Tao, Yizeng Li, Dhruv K. Vig, and Sean X. Sun. Cell mechanics: A dialogue. *Reports on Progress in Physics*, 80(3), 2017.

[69] Dimitrios Vavylonis, Jian-Qiu Wu, Steven Hao, Ben O'Shaughnessy, and Thomas D. Pollard. Assembly mechanism of the contractile ring for cytokinesis by fission yeast. *Science*, 319(5859):97–100, jan 2008.

[70] Tim Steinbacher and Klaus Ebnet. The regulation of junctional actin dynamics by cell adhesion receptors. *Histochemistry and Cell Biology*, 150(4):341–350, 2018.

[71] Ke Xu, Guisheng Zhong, and Xiaowei Zhuang. Actin, spectrin, and associated proteins form a periodic cytoskeletal structure in axons. *Science*, 339(6118):452–6, jan 2013.

[72] Guisheng Zhong, Jiang He, Ruobo Zhou, Damaris Lorenzo, Hazen P. Babcock, Vann Bennett, and Xiaowei Zhuang. Developmental mechanism of the periodic membrane skeleton in axons. *eLife*, 3:1–21, 2014.

[73] Alexander Babich, Shuixing Li, Roddy S. O'Connor, Michael C. Milone, Bruce D. Freedman, and Janis K. Burkhardt. F-actin polymerization and retrograde flow drive sustained PLCγ1 signaling during T cell activation. *Journal of Cell Biology*, 197(6):775–787, 2012.

[74] King Lam Hui and Arpita Upadhyaya. Dynamic microtubules regulate cellular contractility during T-cell activation. *Proceedings of the National Academy of Sciences of the United States of America*, 114(21):E4175–E4183, may 2017.

[75] Rodrigo Cáceres, Majdouline Abou-Ghali, and Julie Plastino. Reconstituting the actin cytoskeleton at or near surfaces in vitro. *Biochimica et Biophysica Acta - Molecular Cell Research*, 1853(11):3006–3014, 2015.

[76] F. J. Nédélec, T Surrey, A. C. Maggs, and S Leibler. Self-organization of microtubules and motors. *Nature*, 389(6648):305–308, 1997.

[77] Julio M Belmonte, Maria Leptin, and François Nédélec. A theory that predicts behaviors of disordered cytoskeletal networks. *Molecular Systems Biology*, 13(9):941, sep 2017.

[78] T. Kim, W. Hwang, and R. D. Kamm. Computational analysis of a cross-linked actin-like network. *Experimental Mechanics*, 49(1):91–104, 2009.

[79] Simon L. Freedman, Shiladitya Banerjee, Glen M. Hocky, and Aaron R. Dinner. A versatile framework for simulating the dynamic mechanical structure of cytoskeletal networks. *Biophysical Journal*, 113(2):448–460, jul 2017.

[80] Tamara Carla Bidone, Wonyeong Jung, Daniel Maruri, Carlos Borau, Roger D. Kamm, and Taeyoon Kim. Morphological transformation and force generation of active cytoskeletal networks. *PLOS Computational Biology*, 13(1):e1005277, jan 2017.

[81] Samantha Stam, Simon L. Freedman, Shiladitya Banerjee, Kimberly L. Weirich, Aaron R. Dinner, and Margaret L. Gardel. Filament rigidity and connectivity tune the deformation modes of active biopolymer networks. *Proceedings of the National Academy of Sciences of the United States of America*, page 201708625, 2017.

[82] Alex Mogilner and Angelika Manhart. Intracellular fluid mechanics: coupling cytoplasmic flow with active cytoskeletal gel. *Annual Review of Fluid Mechanics*, 50:347–370, 2018.

[83] Pavel I Zhuravlev, Yueheng Lan, Maria S Minakova, and Garegin A Papoian. Theory of active transport in filopodia and stereocilia. *Proceedings of the National Academy of Sciences of the United States of America*, 109(27):10849–10854, jul 2012.

[84] Longhua Hu and Garegin A. Papoian. Molecular transport modulates the adaptive response of branched actin networks to an external force. *The Journal of Physical Chemistry B*, 117(42):13388–13396, oct 2013.

[85] Carlos Floyd, Garegin A. Papoian, and Christopher Jarzynski. Quantifying dissipation in actomyosin networks. *Interface Focus*, 9(3), 2019.

[86] Michael A. Gibson and Jehoshua Bruck. Efficient exact stochastic simulation of chemical systems with many species and many channels. *The Journal of Physical Chemistry A*, 104(9):1876–1889, 2000.

[87] Daniel T. Gillespie. A general method for numerically simulating the stochastic time evolution of coupled chemical reactions. *Journal of Computational Physics*, 22(4):403–434, 1976.

[88] Daniel T. Gillespie. Exact stochastic simulation of coupled chemical reactions. *Journal of Physical Chemistry*, 81(25):2340–2361, 1977.

[89] C. S. Peskin, G. M. Odell, and G. F. Oster. Cellular motions and thermal fluctuations: the Brownian ratchet. *Biophysical Journal*, 65(1):316–324, 1993.

[90] Tobias T. Falzone, Savanna Blair, and Rae M. Robertson-Anderson. Entangled F-actin displays a unique crossover to microscale nonlinearity dominated by entanglement segment dynamics. *Soft Matter*, 11(22):4418–4423, 2015.

[91] Mihály Kovács, Fei Wang, Aihua Hu, Yue Zhang, and James R. Sellers. Functional divergence of human cytoplasmic myosin II. *Journal of Biological Chemistry*, 278(40):38132–38140, oct 2003.

[92] Xiaona Li, Qin Ni, Xiuxiu He, Jun Kong, Soon-Mi Lim, Garegin A. Papoian, Jerome P. Trzeciakowski, Andreea Trache, and Yi Jiang. Tensile force-induced cytoskeletal remodeling: mechanics before chemistry. *PLOS Computational Biology*, 16(6):e1007693, 2020.

[93] Adam J Engler, Shamik Sen, H Lee Sweeney, and Dennis E Discher. Matrix elasticity directs stem cell lineage specification. *Cell*, 126(4):677–89, aug 2006.

[94] Viola Vogel and Michael P Sheetz. Cell fate regulation by coupling mechanical cycles to biochemical signaling pathways. *Current Opinion in Cell Biology*, 21(1):38–46, feb 2009.

[95] V M Weaver, O W Petersen, F Wang, C A Larabell, P Briand, C Damsky, and M J Bissell. Reversion of the malignant phenotype of human breast cells in three-dimensional culture and in vivo by integrin blocking antibodies. *The Journal of Cell Biology*, 137(1):231–45, apr 1997.

[96] Donald E Ingber. Mechanical signaling and the cellular response to extracellular matrix in angiogenesis and cardiovascular physiology. *Circulation Research*, 91(10):877–87, nov 2002.

[97] H D Intengan and E L Schiffrin. Structure and mechanical properties of resistance arteries in hypertension: role of adhesion molecules and extracellular matrix determinants. *Hypertension (Dallas, Tex. : 1979)*, 36(3):312–8, sep 2000.

[98] Chaohong Li and Qingbo Xu. Mechanical stress-initiated signal transduction in vascular smooth muscle cells in vitro and in vivo. *Cellular Signalling*, 19(5):881–91, may 2007.

[99] Deshun Lu and Ghassan S Kassab. Role of shear stress and stretch in vascular mechanobiology. *Journal of the Royal Society, Interface*, 8(63):1379–85, oct 2011.

[100] Amanda R Lawrence and Keith J Gooch. Transmural pressure and axial loading interactively regulate arterial remodeling ex vivo. *American Journal of Physiology. Heart and Circulatory Physiology*, 297(1):H475–84, jul 2009.

[101] D J Patel and D L Fry. Longitudinal tethering of arteries in dogs. *Circulation Research*, 19(6):1011–21, dec 1966.

[102] P Van Loon. Length-force and volume-pressure relationships of arteries. *Biorheology*, 14(4):181–201, 1977.

[103] René F M van Oers, Elisabeth G Rens, Danielle J LaValley, Cynthia A Reinhart-King, and Roeland M H Merks. Mechanical cell-matrix feedback explains pairwise and collective endothelial cell behavior in vitro. *PLOS Computational Biology*, 10(8):e1003774, aug 2014.

[104] Donald E Ingber. Cellular mechanotransduction: putting all the pieces together again. *The FASEB Journal*, 20(7):811–27, may 2006.

[105] N Wang, K Naruse, D Stamenović, J J Fredberg, S M Mijailovich, I M Tolić-Nørrelykke, T Polte, R Mannix, and D E Ingber. Mechanical behavior in living cells consistent with the tensegrity model. *Proceedings of the National Academy of Sciences of the United States of America*, 98(14):7765–70, jul 2001.

[106] Hiroaki Hirata, Hitoshi Tatsumi, and Masahiro Sokabe. Mechanical forces facilitate actin polymerization at focal adhesions in a zyxin-dependent manner. *Journal of Cell Science*, 121(Pt 17):2795–804, sep 2008.

[107] Andreea Trache and Soon-Mi Lim. Live cell response to mechanical stimulation studied by integrated optical and atomic force microscopy. *Journal of Visualized Experiments*, (44), oct 2010.

[108] Deok-Ho Kim, Karam Han, Kshitiz Gupta, Keon W Kwon, Kahp-Yang Suh, and Andre Levchenko. Mechanosensitivity of fibroblast cell shape and movement to anisotropic substratum topography gradients. *Biomaterials*, 30(29):5433–44, oct 2009.

[109] Jan Mueller, Gregory Szep, Maria Nemethova, Ingrid de Vries, Arnon D. Lieber, Christoph Winkler, Karsten Kruse, J. Victor Small, Christian Schmeiser, Kinneret Keren, Robert Hauschild, and Michael Sixt. Load adaptation of lamellipodial actin networks. *Cell*, 171(1):188–200.e16, 2017.

[110] K. E. Kasza, C. P. Broedersz, G. H. Koenderink, Y. C. Lin, W. Messner, E. A. Millman, F. Nakamura, T. P. Stossel, F. C. MacKintosh, and D. A. Weitz. Actin filament length tunes elasticity of flexibly cross-linked actin networks. *Biophysical Journal*, 99(4):1091–1100, 2010.

[111] Daisuke Mizuno, Catherine Tardin, C. F. Schmidt, and F. C. MacKintosh. Nonequilibrium mechanics of active cytoskeletal networks. *Science*, 315(5810):370–373, 2007.

[112] K M Schmoller, P Fernández, R C Arevalo, D L Blair, and A R Bausch. Cyclic hardening in bundled actin networks. *Nature Communications*, 1:134, 2010.

[113] Achim Besser and Ulrich S. Schwarz. Coupling biochemistry and mechanics in cell adhesion: A model for inhomogeneous stress fiber contraction. *New Journal of Physics*, 9, 2007.

[114] Romain Levayer and Thomas Lecuit. Biomechanical regulation of contractility: Spatial control and dynamics. *Trends in Cell Biology*, 22(2):61–81, 2012.

[115] Achim Besser, Julien Colombelli, Ernst H K Stelzer, and Ulrich S. Schwarz. Viscoelastic response of contractile filament bundles. *Physical Review E - Statistical, Nonlinear, and Soft Matter Physics*, 83(5):1–12, 2011.

[116] Aravind Chandrasekaran, Arpita Upadhyaya, and Garegin A. Papoian. Remarkable structural transformations of actin bundles are driven by their initial polarity, motor activity, crosslinking, and filament treadmilling. *PLOS Computational Biology*, 15(7):e1007156, 2019.

[117] Stefan Münster, Louise M Jawerth, Beverly A Leslie, Jeffrey I Weitz, Ben Fabry, and David A Weitz. Strain history dependence of the nonlinear stress response of fibrin and collagen networks. *Proceedings of the National Academy of Sciences of the United States of America*, 110(30):12197–202, jul 2013.

[118] R. K. Meyer and U. Aebi. Bundling of actin filaments by α-actinin depends on its molecular length. *Journal of Cell Biology*, 110(6):2013–2024, 1990.

[119] T T Egelhoff, R J Lee, and J A Spudich. Dictyostelium myosin heavy chain phosphorylation sites regulate myosin filament assembly and localization in vivo. *Cell*, 75(2):363–71, oct 1993.

[120] T D Pollard, L Blanchoin, and R D Mullins. Molecular mechanisms controlling actin filament dynamics in nonmuscle cells. *Annual Review of Biophysics and Biomolecular Structure*, 29:545–76, 2000.

[121] J Xu, Y Tseng, and D Wirtz. Strain hardening of actin filament networks. Regulation by the dynamic cross-linking protein alpha-actinin. *The Journal of Biological Chemistry*, 275(46):35886–92, nov 2000.

[122] Y Tseng and D Wirtz. Mechanics and multiple-particle tracking microheterogeneity of alpha-actinin-cross-linked actin filament networks. *Biophysical journal*, 81(3):1643–56, sep 2001.

[123] Marie-France Carlier and Dominique Pantaloni. Control of actin dynamics in cell motility. *Journal of Molecular Biology*, 269(4):459–467, jun 1997.

[124] Akira Katsumi, Tomoki Naoe, Tadashi Matsushita, Kozo Kaibuchi, and Martin Alexander Schwartz. Integrin activation and matrix binding mediate cellular responses to mechanical stretch. *Journal of Biological Chemistry*, 280(17):16546–16549, 2005.

[125] Francis J Alenghat and Donald E Ingber. Mechanotransduction: all signals Point to cytoskeleton, matrix, and integrins. *Science Signaling*, 2002(119):pe6–pe6, feb 2002.

[126] B Geiger and A Bershadsky. Assembly and mechanosensory function of focal contacts. *Current Opinion in Cell Biology*, 13(5):584–92, oct 2001.

[127] Yun Chen, Ana M Pasapera, Alan P Koretsky, and Clare M Waterman. Orientation-specific responses to sustained uniaxial stretching in focal adhesion growth and turnover. *Proceedings of the National Academy of Sciences of the United States of America*, 110(26):E2352–61, jun 2013.

[128] Wenwu Zhang and Susan J Gunst. Dynamic association between alpha-actinin and beta-integrin regulates contraction of canine tracheal smooth muscle. *The Journal of Physiology*, 572(Pt 3):659–76, may 2006.

[129] Démosthène Mitrossilis, Jonathan Fouchard, Axel Guiroy, Nicolas Desprat, Nicolas Rodriguez, Ben Fabry, and Atef Asnacios. Single-cell response to stiffness exhibits muscle-like behavior. *Proceedings of the National Academy of Sciences of the United States of America*, 106(43):18243–8, oct 2009.

[130] Thomas D. Pollard. Regulation of actin filament assembly by Arp2/3 complex and formins. *Annu Rev Biophys Biomol Struct*, 36:451–477, 2007.

[131] Marie France Carlier and Shashank Shekhar. Global treadmilling coordinates actin turnover and controls the size of actin networks. *Nature Reviews Molecular Cell Biology*, 18(6):389–401, 2017.

[132] Priyamvada Chugh, Andrew G. Clark, Matthew B. Smith, Davide A.D. D. Cassani, Kai Dierkes, Anan Ragab, Philippe P. Roux, Guillaume Charras, Guillaume Salbreux, and Ewa K. Paluch. Actin cortex architecture regulates cell surface tension. *Nature Cell Biology*, 19(6):689–697, 2017.

[133] Alexander Mogilner and George Oster. Cell Motility Driven by Actin Polymerization. *Biophysical Journal*, 71(6):3030–3045, 1996.

[134] Kausalya Murthy and Patricia Wadsworth. Myosin-II-dependent localization and dynamics of F-actin during cytokinesis. *Current Biology*, 15(8):724–731, 2005.

[135] Martin Pring, Marie Evangelista, Charles Boone, Changsong Yang, and Sally H. Zigmond. Mechanism of formin-induced nucleation of actin filaments. *Biochemistry*, 42(2):486–496, jan 2003.

[136] Aliaksandr A. Halavatyi, Petr V. Nazarov, Ziad Al Tanoury, Vladimir V. Apanasovich, Mikalai Yatskou, and Evelyne Friederich. A mathematical model of actin filament turnover for fitting FRAP data. *European Biophysics Journal*, 39(4):669–677, 2010.

[137] Michael Mak, Muhammad H. Zaman, Roger D. Kamm, and Taeyoon Kim. Interplay of active processes modulates tension and drives phase transition in self-renewing, motor-driven cytoskeletal networks. *Nature Communications*, 7(May 2015):10323, jan 2016.

[138] Carlos S Floyd, Christopher Jarzynski, and Garegin A Papoian. Low-dimensional manifold of actin polymerization dynamics. *New Journal of Physics*, aug 2017.

[139] Shashank Shekhar and Marie-France Carlier. Enhanced depolymerization of actin filaments by ADF/cofilin and monomer funneling by capping protein cooperate to accelerate barbed-end growth. *Current Biology*, 27(13):1990–1998.e5, jul 2017.

[140] Takushi Miyoshi, Takahiro Tsuji, Chiharu Higashida, Maud Hertzog, Akiko Fujita, Shuh Narumiya, Giorgio Scita, and Naoki Watanabe. Actin turnover-dependent fast dissociation of capping protein in the dendritic nucleation actin network: Evidence of frequent filament severing. *Journal of Cell Biology*, 175(6):947–955, 2006.

[141] D A Schafer, P B Jennings, and J A Cooper. Dynamics of capping protein and actin assembly in vitro: uncapping barbed ends by polyphosphoinositides. *The Journal of Cell Biology*, 135(1), 1996.

[142] Laurent Blanchoin, Kurt J. Amann, Henry Higgs, Jean-Baptiste Marchand, Donald A. Kaiser, and Thomas D. Pollard. Direct observation of dendritic actin filament networks nucleated by Arp2/3 complex and WASP/Scar proteins. *Nature*, 404(1994):1007–1011, 2000.

[143] Fabian Heinemann, Holger Doschke, and Manfred Radmacher. Keratocyte lamellipodial protrusion is characterized by a concave force-velocity relation. *Biophysical Journal*, 100(6):1420–7, mar 2011.

[144] Ruizhe Wang and Anders E Carlsson. How capping protein enhances actin filament growth and nucleation on biomimetic beads. *Physical Biology*, 12(6):066008, nov 2015.

[145] Naoki Watanabe and Timothy J Mitchison. Single-molecule speckle analysis of actin filament turnover in lamellipodia. *Science*, 295(5557):1083–6, 2002.

[146] Matthew B. Smith, Erdem Karatekin, Andrea Gohlke, Hiroaki Mizuno, Naoki Watanabe, and Dimitrios Vavylonis. Interactive, computer-assisted tracking of speckle trajectories in fluorescence microscopy: Application to actin polymerization and membrane fusion. *Biophysical Journal*, 101(7):1794–1804, 2011.

[147] Anne-Cécile Reymann, Cristian Suarez, Christophe Guérin, Jean-Louis Martiel, Christopher J Staiger, Laurent Blanchoin, and Rajaa Boujemaa-Paterski. Turnover of branched actin filament networks by stochastic fragmentation with ADF/cofilin. *Molecular Biology of the Cell*, 22(14):2541–2550, 2011.

[148] Pavel I. Zhuravlev, Bryan S. Der, and Garegin A. Papoian. Design of active transport must be highly intricate: a possible role of myosin and Ena/VASP for G-actin transport in filopodia. *Biophysical Journal*, 98(8):1439–1448, apr 2010.

[149] Laurent Blanchoin and Thomas D. Pollard. Hydrolysis of ATP by polymerized actin depends on the bound divalent cation but not profilin. *Biochemistry*, 41(2):597–602, 2002.

[150] Marco Fritzsche, C. Erlenka mper, Emad Moeendarbary, G. Charras, and Karsten Kruse. Actin kinetics shapes cortical network structure and mechanics. *Science Advances*, 2(4):e1501337–e1501337, apr 2016.

[151] Martin Bergert, Stanley D Chandradoss, Ravi a Desai, and Ewa Paluch. Cell mechanics control rapid transitions between blebs and lamellipodia during migration. *Proceedings of the National Academy of Sciences of the United States of America*, 109(36):14434–9, 2012.

[152] Martin P Stewart, Jonne Helenius, Yusuke Toyoda, Subramanian P Ramanathan, Daniel J Muller, and Anthony A Hyman. Hydrostatic pressure and the actomyosin cortex drive mitotic cell rounding. *Nature*, 469(7329):226–230, 2011.

[153] Miia Bovellan, Yves Romeo, Maté Biro, Annett Boden, Priyamvada Chugh, Amina Yonis, Malti Vaghela, Marco Fritzsche, Dale Moulding, Richard Thorogate, Antoine Jégou, Adrian J. Thrasher, Guillaume Romet-Lemonne, Philippe P. Roux, Ewa K. Paluch, and Guillaume Charras. Cellular control of cortical actin nucleation. *Current Biology*, 24(14):1628–1635, 2014.

[154] John A. Hammer, Jia Wang, Mezida Saeed, and Antonio Pedrosa. Origin, organization, dynamics, and function of actin and actomyosin networks at the T cell immunological synapse. *Annual Review of Immunology*, 37(1):201–224, 2018.

[155] Harvey F. Lodish. *Molecular cell biology*. W.H. Freeman, 2000.

[156] Elena G. Yarmola. Actin-Latrunculin A structure and function:differential modulation of actin-binding protein function by latrunculin A. *Journal of Biological Chemistry*, 275(36):28120–28127, jun 2000.

[157] Pilong Li, Sudeep Banjade, Hui Chun Cheng, Soyeon Kim, Baoyu Chen, Liang Guo, Marc Llaguno, Javoris V. Hollingsworth, David S. King, Salman F. Banani, Paul S. Russo, Qiu Xing Jiang, B. Tracy Nixon, and Michael K. Rosen. Phase transitions in the assembly of multivalent signalling proteins. *Nature*, 483(7389):336–340, 2012.

[158] C. P. Brangwynne, C. R. Eckmann, D. S. Courson, A. Rybarska, Carsten Hoege, Jöbin Gharakhani, F. Julicher, and Anthony A Hyman. Germline P granules are liquid droplets that localize by controlled dissolution/condensation. *Science*, 324(5935):1729–1732, jun 2009.

[159] J.-Q. Jian-Qiu Wu and Thomas D Pollard. Counting Cytokinesis Proteins Globally and Locally in Fission Yeast. *Science*, 310(5746):310–314, oct 2005.

[160] Susan J Gunst and Wenwu Zhang. Actin cytoskeletal dynamics in smooth muscle: a new paradigm for the regulation of smooth muscle contraction. *American journal of physiology. Cell physiology*, 295(3):C576–87, sep 2008.

[161] Luis A. Martinez-Lemus, Michael A. Hill, and Gerald A. Meininger. The plastic nature of the vascular wall: a continuum of remodeling events contributing to control of arteriolar diameter and structure. *Physiology*, 24(1):45–57, 2009.

[162] A B Verkhovsky, T M Svitkina, and G G Borisy. Polarity sorting of actin filaments in cytochalasin-treated fibroblasts. *Journal of Cell Science*, 110(11):1693–704, 1997.

[163] E. M. Craig, S. Dey, and A. Mogilner. The emergence of sarcomeric, graded-polarity and spindle-like patterns in bundles of short cytoskeletal polymers and two opposite molecular motors. *Journal of Physics Condensed Matter*, 23(37), 2011.

[164] Jeremy L. England. Dissipative adaptation in driven self-assembly. *Nature Nanotechnology*, 10(11):919–923, 2015.

[165] Daniel S. Seara, Vikrant Yadav, Ian Linsmeier, A. Pasha Tabatabai, Patrick W. Oakes, S. M.Ali Tabei, Shiladitya Banerjee, and Michael P. Murrell. Entropy production rate is maximized in non-contractile actomyosin. *Nature Communications*, 9(1):1–10, 2018.

[166] Toshihiro Toyota, David A. Head, Christoph F. Schmidt, and Daisuke Mizuno. Non-Gaussian athermal fluctuations in active gels. *Soft Matter*, 7(7):3234–3239, 2011.

[167] Yu Shi, Christopher L. Porter, John C. Crocker, and Daniel H. Reich. Dissecting fat-tailed fluctuations in the cytoskeleton with active micropost arrays. *Proceedings of the National Academy of Sciences of the United States of America*, 116(28):13839–13846, 2019.

[168] Adriano Mesquita Alencar, Mariana Sacrini Ayres Ferraz, Chan Young Park, Emil Millet, Xavier Trepat, Jeffrey J Fredberg, and James P Butler. Non-equilibrium cytoquake dynamics in cytoskeletal remodeling and stabilization. *Soft matter*, 12(41):8506–8511, 2016.

[169] James Liman, Carlos Bueno, Yossi Eliaz, Nicholas P. Schafer, M. Neal Waxham, Peter G. Wolynes, Herbert Levine, and Margaret S. Cheung. The role of the Arp2/3 complex in shaping the dynamics and structures of branched actomyosin networks. *Proceedings of the National Academy of Sciences of the United States of America*, 117(20):10825–10831, 2020.

[170] Carlos Floyd, Herbert Levine, Christopher Jarzynski, and Garegin A Papoian. Driven-dissipative dynamics of active cytoskeletal networks underlie near-critical energy fluctuations. *arXiv preprint arXiv:2006.01884*, 2020.

[171] X Wu, G E Davis, G A Meininger, E Wilson, and M J Davis. Regulation of the L-type calcium channel by alpha 5beta 1 integrin requires signaling between focal adhesion proteins. *The Journal of Biological Chemistry*, 276(32):30285–92, aug 2001.

[172] D.H. Wachsstock, W.H. Schwartz, and T.D. Pollard. Affinity of alpha-actinin for actin determines the structure and mechanical properties of actin filament gels. *Biophysical Journal*, 65(1):205–214, 1993.

[173] A. Ott, M. Magnasco, A. Simon, and A. Libchaber. Measurement of the persistence length of polymerized actin using fluorescence microscopy. *Physical Review E*, 48(3), 1993.

[174] Andrej Vilfan and Thomas Duke. Instabilities in the transient response of muscle. *Biophysical Journal*, 85(2):818–827, 2003.

[175] B. A. Didonna and Alex J. Levine. Unfolding cross-linkers as rheology regulators in F-actin networks. *Physical Review E - Statistical, Nonlinear, and Soft Matter Physics*, 75(4):1–10, 2007.

[176] Thorsten Erdmann, Philipp J. Albert, and Ulrich S. Schwarz. Stochastic dynamics of small ensembles of non-processive molecular motors: The parallel cluster model. *Journal of Chemical Physics*, 139(17), 2013.

[177] Jorge M. Ferrer, Hyungsuk Lee, Jiong Chen, Benjamin Pelz, Fumihiko Nakamura, Roger D. Kamm, and Matthew J. Lang. Measuring molecular rupture forces between single actin filaments and actin-binding proteins. *Proceedings of the National Academy of Sciences of the United States of America*, 105(27):9221–6, 2008.

[178] Matthew J. Footer, Jacob W.J. Kerssemakers, Julie A. Theriot, and Marileen Dogterom. Direct measurement of force generation by actin filament polymerization using an optical trap. *Proceedings of the National Academy of Sciences of the United States of America*, 104(7):2181–2186, 2007.

[179] Alexander B Verkhovsky, T M Svitkina, and G G Borisy. Myosin II filament assemblies in the active lamella of fibroblasts: their morphogenesis and role in the formation of actin filament bundles. *The Journal of Cell Biology*, 131(4):989–1002, nov 1995.

[180] Brittany J. Belin, Lauren M. Goins, and R. Dyche Mullins. Comparative analysis of tools for live cell imaging of actin network architecture. *BioArchitecture*, 4(6):189–202, 2014.